HIGH TEMPERATURE HALL EFFECT MEASUREMENT SYSTEM DESIGN, MEASUREMENT AND ANALYSIS

By

Isil Berkun

A DISSERTATION

Submitted to
Michigan State University
in partial fulfillment of the requirements
for the degree of

Electrical Engineering – Doctor of Philosophy

2015

ABSTRACT

HIGH TEMPERATURE HALL EFFECT MEASUREMENT SYSTEM DESIGN, MEASUREMENT AND ANALYSIS

By

Isil Berkun

A reliable knowledge of the transport properties of semiconductor materials is essential for the development and understanding of a number of electronic devices. In this thesis, the work on developing a Hall Effect measurement system with software based data acquisition and control for a temperature range of 300K-700K will be described. A system was developed for high temperature measurements of materials including single crystal diamond, poly-crystalline diamond, and thermoelectric compounds. An added capability for monitoring the current versus voltage behavior of the contacts was used for studying the influence of ohmic and non-ohmic contacts on Hall Effect measurements. The system has been primarily used for testing the transport properties of boron-doped single crystal diamond (SCD) deposited in a microwave plasma-assisted chemical vapor deposition (MPCVD) reactor [1]. Diamond has several outstanding properties that are of high interest for its development as an electronic material. These include a relatively wide band gap of 5.5 (eV), high thermal conductivity, high mobility, high saturation velocity, and a high breakdown voltage. For a temperature range of 300K-700K, IV curves, Hall mobilities and carrier concentrations are shown. Temperature dependent Hall effect measurements have shown carrier concentrations from below $10^{17}cm^{-3}$ to approximately $10^{21}cm^{-3}$ with mobilities ranging from $763(cm^2/Vs)$ to $0.15(cm^2/Vs)$ respectively. Simulation results have shown the effects of single and mixed carrier models, activation energies, effective mass and doping concentrations. These studies have been helpful in the development of single crystal diamond for diode applications.

Reference materials of Ge and GaAs were used to test the Hall Effect system. The system was also used to characterize polycrystalline diamond deposited on glass for electrochemical applications, and $Mg_2(Si, Sn)$ compounds which are promising candidates of low-cost, light weight and non-toxic thermoelectric materials made from abundant elements and are suited for power generation application in the intermediate temperature range of (600 K - 800 K). In this work the thermoelectric materials were synthesized by a solid-state reaction using a molten-salt sealing method. The ingots produced were then powder processed, followed by pulsed electric sintering (PECS) densification. A set of $Mg_{2.08}Si_{0.4-x}Sn_{0.6}Sb_x$ $(0 \leq x \leq 0.072)$ compounds were investigated and a peak ZT of 1.50 was obtained at 716 K in $Mg_{2.08}Si_{0.364}Sn_{0.6}Sb_{0.036}$ [2]. The high ZT value is related to a high electrical conductivity in these samples, which are possibly caused by a magnesium deficiency in the final product. Analysis of the measured results using LabVIEW and MATLAB developed programs showed good agreement with expected results and gave insight on mixed carrier dopant concentrations.

TABLE OF CONTENTS

LIST OF TABLES

LIST OF FIGURES

ACKNOWLEDGMENTS

I would like to express my deepest gratitude to my advisor, Prof. Timothy Hogan, who leads by example, for his outstanding guidance, consistent encouragement and being my role model both professionally and personally. Special thanks go to Prof. Timothy Grotjohn, Prof. Donnie Reinhard, Prof. Jes Asmussen and Prof. Greg Swain for being my committee members and their excellent support and guidance throughout my PhD studies. Also, I would like to thank my colleagues in the Electronic Materials and Pulsed Laser Deposition and Diamond Electronics Labs.

My gratitude extends to my parents, Hayriye and Ismail Berkun, for their support and encouragement. Also I would like to thank to my best friend and grandma Ayhan Berkun, my family members Funda Berkun and Alparslan Berkun. Their prayers for me during the course of this study have brought many blessings into my life. Special gratitude and appreciation goes to my yoga family in East Lansing. Their friendship and community have provided me support and encouragement. Last but not least, I would like to extend my sincere gratitude to my friends Will Cicola, Karyn Coward, Kazuko Fuchi, Sedat Gur, Letizia Tozzini, Ami Blue, Kitty Cox, Cagri Ozcaglar, Kathleen Donahue and many others.

Chapter 1

Introduction

1.1 Why Diamond?

Diamond has a broad range of applications incuding but not limited to power electronics, micro - electromechanical systems (MEMS), biomedical sensors, optics, thermal management, electrochemical electrodes and lasers. A few examples for diamond's common application areas are as follows:

Diamond is a versatile material. It is commonly used in improving the mechanical performance of industrial parts, processed by different methods including physical vapor deposition (PVD). Due to the extraordinary electrochemical properties of diamond including relatively low background current which results to improved signal-to-backround (SBR) and signal-to-noise (SNR) ratios, diamond has a high application potential in both aqueous and non-aqueous media and holds microstructural and morphological stability at relatively high temperatures (e.g. $180°C$) [15]. Diamond has a high thermal conductivity (approximately four times higher than copper), thus diamond is a practical material for thermal applications. The chemical and biological inertness of diamond allows for its use in severe chemical and radioactive environments that destroys other materials and helps it find practical applications in biosensor area [16]. Diamond has a highly symmetrical lattice as well as very strong bonding, thus, diamonds cubic symmetry minimizes the impact of multiple crystalline orientations in the film on performance which makes it a useful material for optics as seen

	Si	GaAs	4H-SiC	6H-SiC	GaN	Diamond
Bandgap (eV)	1.12	1.424	3.26	3.03	3.295	5.47
Maximum Electric Field (MV/cm)	0.41	0.48	2.4	2.4	5	20
Electron Mobility (cm^2/Vs)	1450	8600	900	400	2000	4500
Hole Mobility (cm^2/Vs)	480	130	120	100	200	3800
Thermal Conductivity (W/mK)	1.5	0.46	4.9	4.9	1.3	20
Relative Dielectric Constant	11.7	12.9	10	9.7	5.35	5.7

Table 1.1 Electrical properties of common wide bandgap semiconductors compared to silicon [3]

in Fig. 1.1. Diamond is transparent at a wide range of wavelengths from the mid-ultraviolet through the microwave portion of the spectrum and beyond [7].

Figure 1.1 Mounted optical grade polycrystalline diamond window, ready for use in high power CO_2 laser optics [7]

Due to the properties of diamond which are described above it is a high interest material for various applications. Diamond is compared with other common semiconductors in Table. 1.1. This work mainly focuses on applications of diamond in electronic devices, taking advantage of it's higher power, higher operating voltages and higher operational temperatures due to wide band gap.

Commonly used growth techniques for making synthetic diamond include the high pressure high temperature technique (HPHT) [17], hot filament chemical vapor deposition (HFCVD),

and microwave plasma chemical vapor deposition (MPCVD) [18]. The HPHT method provides growth of bulk crystals which are used to grow thin single crystal films on the top surface in this work, while the CVD-method is used for homoepitaxial growth of single crystal films on single crystal substrates. Thus, the crystal quality of films highly depends on the quality of substrate. Characterization of MPCVD grown p (mainly boron doped) or n type (mainly phosphorus doped) single crystal diamond films (SCD) on top of HPHT substrates for power electronic applications will be the main focus of this thesis. An essential need in the study of boron or phosphorus doped diamond semiconductors is the reliable and accurate determination of the critical electronic transport properties, such as the temperature dependent conductivity, carrier concentration, and carrier mobility of the deposited film. A detailed description on the measurement of these critical properties for a temperature range of 300K - 700K are provided in the following sections of this thesis.

1.2 Electrical Transport Characterization

1.2.0.1 Hall Effect Systems

In order to accurately characterize the electrical transport properties of semiconductors, temperature dependent Hall effect systems have been built by several research groups and reported in the literature, such as systems for thermoelectrics materials where the Van der Pauw method is used with pressure contacts [19], systems for refractory materials having high charge carrier concentrations; generally with low mobilities [20], some systems include a circuit which combines the best features of both ac and dc apparatus where errors due to thermal emf's and the Ettingshausen effect are eliminated [21], measurement systems for ferromagnetic semiconductors [22], systems for low-mobility samples at high temperatures

[23], systems that are capable of measuring eight samples simultaneously [24], systems for low electron mobility materials such as copper [25]. A temperature dependent Hall Effect measurement system with software based data acquisition and control was built and tested as a part of this PhD work [1].This system alters from the previously reported systems by adding several control components including a software based PID temperature controller, temperature dependent I-V measurements for monitoring the annealing effects on contact resistances under vacuum environment, and the capability to accommodate samples for both van der Pauw and inline geometrical configurations. Electronic transport measurements are shown for boron-doped single crystal diamond (SCD) films deposited in a microwave plasma-assisted chemical vapor deposition (MPCVD) reactor. The influence of ohmic contacts and PID temperature control accuracy and stability are studied. For a temperature range of 300K - 700K IV curves, Hall mobilities and carrier concentrations are presented as shown in the following sections in more detail.

1.2.0.2 Hall Effect Measurements on Diamond

Electrical transport studies for diamond in literature consists of several types of diamond samples including HPHT grown bulk single crystal diamond and MPCVD grown diamond thin films. Temperature dependent Hall effect measurements have been reported by several groups. These studies report three types of conduction mechanisms along with three activation energies.

$$\sigma = \sigma_1 * exp(-E_{a1}/kT) + \sigma_2 * exp(-E_{a2}/kT) + \sigma_3 * exp(-E_{a3}/kT) \tag{1.1}$$

In Eq. 1.1, E_{a1} is the activation energy for valance band conduction due to acceptor

ionization, E_{a2} is an activation energy for impurity band conduction due to the motion of carriers over neutral acceptors and E_{a3} is an activation energy for hopping conduction due to the transition of holes from occupied to unoccupied acceptor sites.

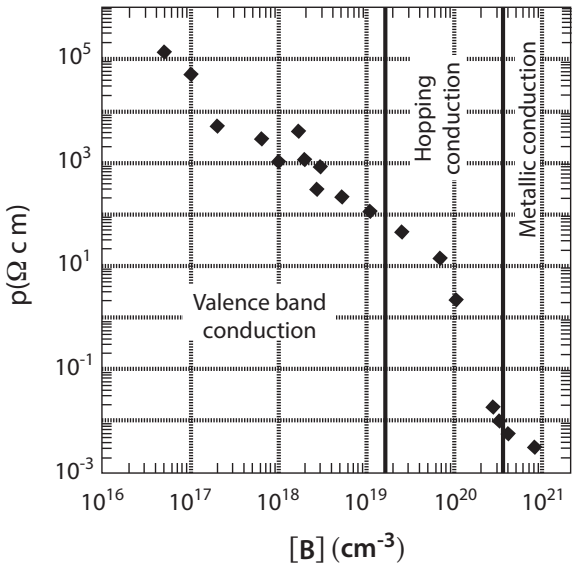

Figure 1.2 Room temperature resistivity as a function of doping concentration. [8]

The resistivities of the diamond films vs. the boron doping are plotted in Fig. 1.2 by Lagrange et al.[8]. According to the report, the resistivity of an undoped film was around $10^{13}\Omega cm$. Considering the results derived from the $I(T)$ curves, depending on the doping, three conduction mechanisms are observed at room temperature. For [B]$< 10^{19}cm^3$, the conduction is mainly dominated by the free holes within the valence band. As the resistivity decreases linearly with [B], the decrease in mobility is relatively low in this region. Between 10^{19} and $3{*}10^{20}cm^3$, the hopping conduction dominates, and the resistivity decreases strongly with [B]. Above $3 * 10^{20}cm^3$, progression of resistivity is not as strong due to the metallic behaviour of the conduction.

Borst et al. fabricated and characterized boron doped homoepitaxial diamond films using

Sample #	Concentration (cm^{-3})	Activation energy (eV)	$\mu \sim T_L^x$ - T_H^y	μ_{min} - μ_{max} (cm^2/Vs)
# 1	$7 - 15x10^{17}$	0.34	$T_L^{0.8}$ - $T_H^{-2.4}$	$5x10^{-6}$ - 250
# 2	–	0.33	$T_L^{1.1}$ - $T_H^{-2.3}$	$3.7x10^{-4}$ - 170
# 3	$1.2x10^{19}$	0.27	$T_L^{1.6}$ - $T_H^{-1.8}$	0.11 - 55
# 4	$4 - 5x10^{19}$	0.16	$T_L^{1.3}$ - $T_H^{-1.5}$	0.55 - 16
# 5	$1.2x10^{20}$	0	$T^{2.8}$	0 - 4
# 6	$3x10^{20}$	0	*Almost linear*	3.5 - 4.5
# 7	$3 - 9x10^{18}$	0.30	$T_H^{1.3}$ - $T_H^{2.2}$	$2.2x10^{-2}$ - 100

Table 1.2 Concentration, activation energy an Hall mobility of seven boron doped homoepitaxial diamond, Borst et al. [4]

microwave plasma chemical vapor deposition (MPCVD). Substrate types were type IIa for samples #1 and #7 and type Ib for all the other samples. Concentration and mobility data are summarized in Table. 1.2 for the temperature range of 100 to 1300K [4].

They have reported 3 main conduction mechanisms taking place: 1. Valance band conduction. 2. Impurity band conduction (sample #5) and 3. Hopping conduction (samples #2, #5 and #7). Sample # 6 is degenerated and showed metallic conduction.

In all other samples, valance band conduction was observed above 300K. Above 773K, the resistance of the type Ib sample becomes comparable and even lower than the resistance of the Hall bars which results as a misguiding raise of the conductivity. As a consequence, it has been reported that only samples # 1 and #7 were reliable in the high temperature range and showed the predicted transition from the exponential increase of the freezeout region to the exhaustion or saturation region.

Hopping conduction can also be present at room temperature in boron doped diamond due to the wide bandgap of diamond and large ionization energy of boron. In this case, nitrogen impurities and other unidentified defects contributed as donors with concentration n_D and gave their electron to the boron acceptors of concentration. Tunneling may occur in the form of nearest neighbor hopping or variable range hopping by thermal activation.

Another parameter which influences diamond electronic device performances is the elec-

tron and hole mobility. The empirical model used to fit the experimental Hall effect measurements reported in literature has been implemented into Silvaco finite element based software via a built-in C language interpreter, in order to take into account the doping concentration and temperature dependence of the mobility [26]. An empirical mobility model they developed shows good agreement with the experiments over a wide range of doping concentration, from $N_A = 10^{14} cm^3$, where the mobility is equal to $2016 cm^2/Vs$, to $N_A = 10^{21} cm^3$ where the mobility falls down to unity. For the phosphorus donor, the mobility is maximum $\mu_{max} = 1030 cm^2/Vs$,for $N_d = 10^{14} cm^{-3}$, and close to unity when $N_d = 10^{20} cm^{-3}$.

During the determination of the electrical transport properties of the materials, defects and the shape of the sample have a critical effect. Electrical properties in the temperature range of $180 - 800K$ with the influence of defects and geometry for high quality bulk single crystal IIb-type diamonds grown by the HPHT method are extensively studied by Bormashov et al. by measuring the defect free region from the actual sample [27]. They did not observe a significant change in resistivity, however observed a significant difference in the Hall effect data. The non-rectangular shaped sample showed a lower carrier mobility due to the inhomogenous acceptor and donor concentrations.

Borsmashov et al. determined the actual concentration of acceptors (N_A, boron) and compensating donors (N_D, nitrogen) by the regression analysis of the temperature dependencies of Hall effect data using the least squares method. They varied both concentration values of the theoretical model of conductivity where Fermi distribution of electrons and holes and the neutrality equation is used, until minumum deviation from the experimental data was achieved. Tau-approximation fit for collusion integral has been used and four scattering mechanisms of carriers were taken into account: by ionized and neutral impurities, and optical and acoustic phonons. At low boron conditions, acceptor concentration decreases

and compensation ratio increases (for mixtures containing less than 0.001% boron).

The maximum mobility achieved was in the range of $2000 - 2200 cm^2/Vs$ at $T = 300K$ and more than $7000 cm^2/Vs$ at $T = 180K$ was found from the mixture which contained 0.0005 to 0.002% boron. As a result of low impurity concentration and low compensation ratio, carrier scattering is not as strong on ionized and non-ionized impurities. Thus, the dominating mechanism is the phonon (lattice) scattering of holes where scattering by neutral and ionized impurity atoms is minimal. In this particular case, the mobility of holes does not depend on the impurity concentration.

For the heavily doped sample, Hall carrier mobility was shown to be very low in the whole temperature range. In addition to the deviation from the valance band conductivity to hopping conduction, defects play a significant role in the electrical transport properties of samples.

Pernot et al. combined theoretical and experimental studies for Hall hole mobility of homoepitaxial boron-doped diamonds in the temperature range of 100K to 900K where the maximum hole mobility was reported to be around $2000 cm^2/Vs$ [28]. Four hole scattering mechanisms have been considered: ionized impurity scattering, neutral impurity scattering, acoustic phonon scattering, and nonpolar optical phonon scattering. Scattering mechanisms and their anisotropy as well as the anisotropy of the valance band energy surface are the three main factors that contribute to the combine Hall scattering factor, r_H which is used to compare the theoretical to experimental data.

(i)In order to study the temperature dependency of the mobility in low boron doped diamond, they looked at four samples with fixed acceptor concentration $N_A = 10^{16} cm^{-3}$ and donor concentrations ranging from $N_D = 0$ to 10^{14}, 10^{15}, $5x10^{15} cm^{-3}$. They have observed the temperature dependence of the four samples are very similar in the low temperature

range (150-300K) with a joint effect of ionized impurity scattering and acoustic phonon scattering (below 200K). However, the high temperature range (larger than 300K) is dominated by phonon acoustical and optical phonons. The acoustical phonon scattering limited the mobility between 200K and 300K.

For the sample with $N_A = 10^{16} cm^{-3}$ and $N_D = 10^{15} cm^{-3}$, the neutral impurity contribution is considerably small in the whole temperature range. This negligible contribution was due to the low density of neutral boron atoms. Between 100K and 200K, ionized impurity scattering dominates due to the ionized compensated centers. Between 200K and 400K, acoustic phonnon scattering dominates which results in a temperature dependency of mobility as $T^{-3/2}$. For the high temperature range, optical phonon scattering dominates. Mobility reported at 700K is $100 cm^2/Vs$ [28]. Effective mass of light holes is low, as a result, they exhibit the highest mobility of the three bands. Effective mass of the spin-orbit holes is in between the light and heavy holes, thus, they have a mobility close but reasonably higher than the total mobility. Most influencing holes are the the heavy holes due to the high density of holes in this band.

(ii)In order to study the temperature dependency of the mobility in highly boron doped diamond, they have investigated several different samples. The moderately doped sample with $N_A = 2.5x10^{17} cm^{-3}$ and $N_D = 10^{15} cm^{-3}$, low temperature mobility is controlled mainly by acoustic scattering, the impurity and neutral impurity scattering mechanisms does not have a significant effect. For the sample with $N_A = 2x10^{18} cm^{-3}$ and $N_D = 3x10^{15} cm^{-3}$, the most important scattering mechanism between 200 and 400K is the neutral impurity scattering, which gives a mobility of $1000 cm^2/Vs$ at room temperature with an activation energy of $0.37eV$ for boron. This corresponds to an ionization ratio of p/N_A lower than a few % up to 400K indicating that a large majority of the boron acceptors are neutral.

For the most highly doped sample with $N_A = 1.7x10^{19}cm^{-3}$ and $N_D = 5x10^{15}cm^{-3}$, the low temperature mobility is completely controlled by neutral impurity mode up to 600K which corresponds to a mobility value of $200cm^2/Vs$. For all the three highly boron doped samples described above, the low temperature mobility decreases due to hopping. From valance band conduction to hopping conduction transition temperature is 150K, 200K and 223K respectively (from low to high doped sample).

Pernot et al. summarized the mobility vs temperature relationship as follows: at 300K, lattice scattering (acoustic and optical) at low doped materials up to $10^{17}cm^{-3}$. When acceptor concentration N_A is larger than $10^{17}cm^{-3}$ neutral impurity scattering is important, when N_A is larger than $3x10^{18}cm^{-3}$, neutral impurity scattering is dominating. Ionized impurity scattering is reported to be not as important in the whole temperature range due to the neglection of the compensation and the high ionization energy of boron compared to the ratio of the ionized boron. At 500K, lattice scattering is reported to be important up to $N_A = 10^{18}cm^{-3}$. In the case of highly doped diamond such as acceptor concentrations higher than $10^{18}cm^{-3}$, neutral impurity mode becomes important and for acceptor concentrations higher than $2x10^{19}cm^{-3}$, neutral impurity mode dominates and ionized impurities are not important [28].

Volpe et al. studied the mobility for low boron doped samples where the acceptor density of the samples has been estimated by capacitance voltage, C(V), measurements around $10^{16}cm^3$ with a maximum mobility value of $1870cm^2/Vs$ at 292 K. Table 1.3 summarizes the mobility and activation energy values for room temperature [5].

Sample #1 was measured to have a mobility significantly higher than the other samples. This is unexpected since the total dopant concentration is comparable to that of sample #2. The activation energy for sample #1, however, is significantly lower than for samples #2

Sample #	N_A (cm^{-3})	N_D (cm^{-3})	E_a (eV)	μ at 292K (cm^2/Vs)
# 1	$1.5x10^{16}$	$4.7x10^{15}$	0.295	1870
# 2	$1.7x10^{16}$	$1.5x10^{15}$	0.380	850
# 3	$2.2x10^{16}$	$2.5x10^{14}$	0.380	870

Table 1.3 The mobility and activation energy values for room temperature on low boron doped samples [5].

and #3. An underestimation of the ionization energy would result in an overestimation of the donor density since the two parameters are strongly correlated. Essentially, the ionized impurity scattering should not be the dominant scattering mechanism for donor densities lower than $5x10^{15}cm^3$, and the limitation of the mobility at room temperature suggested to be due to the crystalline quality of the layer, mostly related to the growth conditions [5].

It is common that more than one scattering mechanism is present in diamond. Time of flight (TOF) measurements are one of the few methods to identify the scattering mechanisms involved. CVD diamond samples are compared with data obtained on commercial samples, literature and theoretical data for IIa diamond in order to report dominant scattering mechacnisms for different temperature regimes by Nesladek et al. [29]. TOF tecnique was also used by Isberg et al. in order to determine the low-field drift mobility values on thick diamond plates for p-i junction diode studies [30]. The boron concentration of their sample was reported to be $1x10^{20}cm^{-3}$.

Deposition conditions have a tremendous effect on surface morphology and electrical properties of boron-doped diamond films synthesized by MPCVD. Effects of trimethylboron on diamond (100) to electronic transport properties of the substrate are presented by Tsubota et al. [31]. They also reported the effects of hydrogen plasma treatment to the surface smoothness and elecrical properties of the boron-doped diamond films. Barjon et al. optimized the growth conditions for MPCVD grown boron doped diamond samples with boron

concentrations ranging from $1x10^{18}cm^{-3}$ to $3x10^{19}cm^{-3}$ and reported the reduction of compensation effects [32]. The effect of substrate temperature between $850-950°C$ and growth rate on the doping efficiency of single crystal boron doped diamond was recently reported by Demlow et al. where heavily boron doped samples with a substrate temperature of $950°C$ showed fewer defects and higher doping efficiency than the samples grown at $850°C$ for boron concentrations ranging from $8.9x10^{18}cm^{-3}$ to $5.8x10^{19}cm^{-3}$ [14].

1.2.1 Ohmic Contacts

Ohmic contacts are essential for accurate Hall effect measurements. The use of silver paste as a contact to diamond yields a high contact resistance.

Das et al. reviewed the processing of metal contacts such as Al or Au on CVD films which showed highly resistive ohmic or nominally asymmetric behavior, where these contacts can be used for forming rectifying contacts on synthetic and natural semiconducting diamond crystals, and also this work pointed out the ohmic contact formation by using metals such as Ti, Ta and Mo with a layer of Au on top, followed by annealing [33].

Transition-metal/Au bilayer metallization have been studied by several groups. Moazed et al. used transition metals including Ti, Ta, Mo and Ni with a thickness of $100-150\mathring{A}$ and a $1500\mathring{A}$ layer of Au on top, followed by annealling at $885C°$ for 8-16min in an H_2 ambient to form ohmic contacts [34]. Volpe et al. used Ti/Pt/Au pads for low boron doped samples followed by annealing at $750C°$ during 30 min to obtain reliable ohmic contacts [5]. Ohmic contacts made out of Ti/Al/Au were deposited by PVD followed by annealing in argon at $600°C$ for the boron doped side of the p-i diode as reported by Isberg et al. [30].

Experimental contact studies have been reported from the same group by using Ti/Au contacts on diamond by B ion implantation where contact resistance was on the order of

10^{-6} $\Omega.cm^2$ [35]. They also fabricated similar contacts on polycrystalline films as well as a natural IIb crystal [36] and reported the electrical characterization of the diamond films including Hall effect measurements and other characterization techniques such as secondary ion mass spectroscopy (SIMS) [37].

Thin films of Mo, Mo/Au and Mo/Ni/Au were also used as contact metals on diamond by a thermally activated solid state reaction process which produced adherent ohmic contacts after annealing at $950°C$ by Moazed et al. [34].

Barjon et al. reported the resistivity of MPCVD grown boron doped diamond samples where Ti/Au contacts were fabricated followed by annealing at $450C°$ for 30 min under Ar in order to obtain an ohmic contact [32].

Using a similar approach, Hewett et al. tested the contacts including Ti, Mo, Al, Ni, Au, Pt and Pd and reported contact resistance as low as $2x10^{-5}\Omega cm^2$ on single crystalline films with boron concentrations of the order of $10^{20}cm^{-3}$. They have studied a transmission line model (TLM) for their contact resistance measurements as well as surface roughness measurements to verify the formation of a carbide for Ta/Au, Ti/Au and Mo/Au contacts[38].

On heavily doped diamond samples with a concentration value of $10^{19}cm^{-3}$, Geis observed that ohmic contacts can be obtained with most evaporated metals without any additional processing with contact resistance of $10^{-6}\Omega cm^2$ [39]. Braunstein et al. used boron implantation-doping of diamond. They have reported conductivity and Hall measurements showing results as a typical heavily doped semiconductor. Ohmic contacts were achieved by using sharp tungsten probes [40].

An annealed Ti/Pt/Au trilayer metallization is a commonly used procedure as reported by Hoff et al. for a naturally occurring type IIb diamond crystal where the Pt served successfully as a barrier to Ti diffusion into the Au capping layer [41], by Bormashov et al.

in the Van der Pauw configuration [27] and by Chen et al. on boron-doped homoepitaxial diamond films with a reported contact resistance of $1.3x10^5 \Omega cm^2$ [42].

Mo/Au contacts deposited on a type II b diamond crystal also reported to show ohmic behaviour with no indication of deterioration or degradation of performance [43].

In normal conditions Au contacts alone on top of boron doped (100) diamond would form rectifying contacts, however Chu et al. showed the fabrication of ohmic contacts by exposure to an argon sputtering prior to the deposition of Au onto semiconducting samples. They also observed that the presputtering step improved the adhesion of the Au film which is commonly a big challange to achieve without a transition metal between diamond and Au [44].

Indium has been used in the past years on semiconducting diamond but due to its low melting point it is not suitable for high temperature environments. Indium has been used successfully to make an ohmic contact on semiconducting diamond crystals where higher temperature regimes are not studied [39].

In diamond diode studies, high quality contacts are essential. Twitchen et al. showed an abstract demonstration of a $2.5kV$ diamond diode provided by electrical measurements using a circular gold Schottky contact, with an area of $1 > mm^2$,on large area free standing single crystal diamond consisting of a thin high purity layer $1 < 10^{13}[B]/cm^3$ on a thicker heavily boron-doped $1 > 10^{19}[B]/cm^3$ substrate with an ohmic back contact. The diode structures were fabricated using a microwave-assisted chemical vapor deposition process [45].

A Si/SiC/diamond multilayer structure has been investigated on natural type-IIb diamond by Fang et al [46]. They deposited $500\mathring{A}$ of Si by ion-beam mixing using Kr+ at 240 keV and substrate temperature of $700°C$. Following the ion beam mixing, an annealing step was processed at $1200°C$ for an hour in forming gas. Transmission line measurements

(TLM) showed measurements showed specific contact resistance of $5x10^{-3}\Omega cm^2$ for samples without ion mixing and $1x10^{-3}\Omega cm^2$ for samples with ion mixing. They have also compared Ta/Au contacts on top of diamond with a specific contact resistivity of $1x10^{-3}\Omega cm$ where it is reported to be non-uniform compared to the Si/diamond contacts.

Geis et al. have established ohmic contacts to type-IIb diamond using surface modification induced by argon-fluoride (ArF) excimer laser radiation with pulses of 193nm. It is reported that the modified layer was stable at $1800C^{\circ}$ and was approximately $40 - 60cm$ thick which was composed of diamond and graphite-like material with a minumum contact resistance of $(4 - 10)x10^{-4}\Omega cm^2$ [47].

Sandhu was able to form ohmic contacts at room temperature to formerly implanted layers in insulating diamond by a selected-area implantation method [48].

Selective doping is a critical method especially for more lightly doped diamond samples in order to obtain ohmic contacs. Borst et al. reported electrical transport characteristics for MPCVD grown B, P, Li and Na doped diamond films which were selectively grown as Hall bars by using a sputtered SiO_2 mask on the diamond substrates. Electrical metal contacts were electron-beam evaporated and annealed at high temperatures [9]. In another paper, Borst et al. have used a selective growth techique with a Hall bar geometry using a sputtered SiO_2 mask followed by bonding the gold wires to the Mo/Pt/Au contacts [4].

Prins et al. used implantation of boron ions to form low resistance ohmic contacts on a type IIb diamond, followed by annealing. Top ion-damaged layer was then removed by etching in a hot acid solution. The remaining higly doped thin surface was then processed with contact deposition [49].

1.3 Hall Effect Measurement Methodology

Resistivity and Hall effect measurements are taken according to the ASTM standard F76-08 [50] which includes best practices for measuring Hall effect for two different sample geometries of van der Pauw and Hall bar configurations as described in 1.3.1 and 1.3.2 respectively.

The Hall effect system includes the following components:

- Electromagnet (up to 1T field strength)
- Sample stage (cryostat with a high temperature stage)
- Current meter to provide current through the sample
- Voltmeter for measuring conductivity and Hall voltages
- Power supplies for the electromagnet and for temperature control of the sample stage
- A computer controlled switching system for controlling magnetic field direction and voltage measurements
- A temperature detector and heater

1.3.1 Van der Pauw Method

Van der Pauw specimens, can have various different geometries according to the standards [50]. Most commonly used one for this work is the square geometry shown in Fig. 1.3.

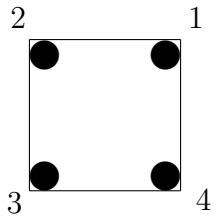

Figure 1.3 Van der Pauw configuration

Contact evaluation is required for measurement quality, ideally linear current voltage characteristics for each contact pair should be observed to be able to obtain reliable measurements. For this work, IV curves for all contact pairs have been tested for different temperature values between 300K to 700K. When the desired temperature stability is maintained, measurements start with resistivity, by applying current and measuring voltage as shown in Eq. 1.2 and 1.3 where the notation $V_{AB,CD}$ refers to the potential difference $V_C - V_D$ measured between contacts C and D when current enters Contact A and and exits Contact B. The constant $1.331 \sim \pi/4\ ln(2)$, units are in volts for voltages, V, centimeters for thickness, t, amperes for current, I, and the geometrical factors, f_A and f_B are function of resistance ratio, more details can be found in the ASTM standard F76-08[50].

$$\rho_A = \frac{1.1331 f_A t}{I}[V_{21,34} - V_{12,34} + V_{32,41} - V_{23,41}]\ \Omega.cm \tag{1.2}$$

$$\rho_B = \frac{1.1331 f_B t}{I}[V_{43,12} - V_{34,12} + V_{14,23} - V_{41,23}]\ \Omega.cm \tag{1.3}$$

If ρ_A is not equal to ρ_B within $\pm$ % 10, the specimen is inhomogenous and a more uniform specimen is required. Average resistivity ρ_{av} is shown in Eq. 1.4.

$$\rho_{avg} = \frac{\rho A + \rho B}{2} \ \Omega.cm \tag{1.4}$$

After the resistivity calculations, magnetic field ($+B$ is out of the sample) is introduced in both directions to calculate the Hall coefficient as shown in Eq. 1.5 and Eq. 1.6. Magnetic field and current directions are flipped to eliminate non-Hall contributions.

$$R_{HC} = \frac{2.5 \times 10^7 t}{BI}[V_{31,42}(+B) - V_{13,42}(+B) + V_{13,42}(-B) - V_{31,42}(-B)] \ cm^3.C^{-3} \tag{1.5}$$

$$R_{HD} = \frac{2.5 \times 10^7 t}{BI}[V_{42,13}(+B) - V_{24,13}(+B) + V_{24,13}(-B) - V_{42,13}(-B)] \ cm^3.C^{-3} \tag{1.6}$$

Similar to resistivity, If R_{HC} is not equal to R_{HD} within $\pm$ % 10, the specimen is inhomogenous and a more uniform specimen is required. Average Hall coefficient R_{Hav} is shown in Eq. 1.7. Units are in volts for voltages, V, centimeters for thickness, t, amperes for current, I, and Gauss for magnetic field, B.

$$R_{Hav} = \frac{R_{HC} + R_{HD}}{2} \ cm^3.C^{-3} \tag{1.7}$$

Hall mobility can be calculated using the average Hall coefficient, R_{Hav} and resistivity, ρ_{av} as shown in Eq. 1.8.

$$\mu_H = \frac{|R_{Hav}|}{\rho_{av}} \ cm.V^{-1}.s^{-1} \tag{1.8}$$

For n-type samples, Hall coefficient is negative whereas, for p-type samples Hall coefficient is positive. Carrier concentration for a p-type semiconductor can be calculated using the average Hall coefficient as shown in Eq. 1.9.

$$p = \frac{1}{R_{Havg} \times q} \; cm^{-3} \tag{1.9}$$

1.3.2 Hall Bar Method

Hall bar samples can have different type of geometries [50]. The thickness of the sample needs to be uniform to ± %1 and should be less than 0.1cm. Length of the specimen must be between 1cm to 1.5cm. Length to width ratio should be ideally greater than 5, however, 4 is the minimum ratio value that would be acceptable for measurements.

Similar to the Van der Pauw samples, Hall bar samples also should have linear current voltage characteristics. To evaluate the contacts, every contact pair should be separately tested for different temperature points. When the desired temperature stability is maintained, measurements start with resistivity, by applying current and measuring voltage as shown in Eq. 1.10 and 1.11 for Hall bar sample with 6 contacts where W is the width, $d_1^{'}$ and d_2 are the distances between the contacts in cm as shown in Fig. 1.4.

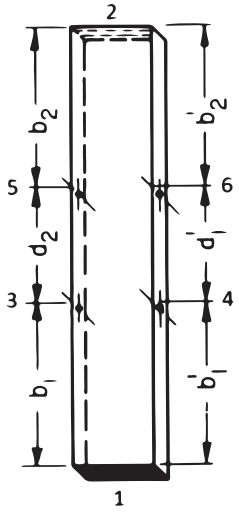

Figure 1.4 Hall bar configuration

$$\rho_A = \frac{Wt}{2Id_1^{'}}[V_{12,46} - V_{21,46}]\ \Omega.cm \tag{1.10}$$

$$\rho_B = \frac{Wt}{2Id_2}[V_{12,35} - V_{21,35}]\ \Omega.cm \tag{1.11}$$

If ρ_A is not equal to ρ_B within $\pm$ % 10, the specimen is inhomogenous and a more uniform specimen is required. Average resistivity ρ_{av} is shown in Eq. 1.12.

$$\rho_{avg} = \frac{\rho A + \rho B}{2}\ \Omega.cm \tag{1.12}$$

Once resistivity is calculated, magnetic field (+B is out of the sample) is introduced in both directions to calculate the Hall coefficient as shown in Eq. 1.13 and Eq. 1.14.

$$R_{HA} = \frac{2.5 \times 10^7 t}{BI}[V_{12,65}(+B) - V_{21,65}(+B) + V_{21,65}(-B) - V_{21,65}(-B)]\ cm^3.C^{-3} \tag{1.13}$$

$$R_{HB} = \frac{2.5 \times 10^7 t}{BI}[V_{12,43}(+B) - V_{21,43}(+B) + V_{21,43}(-B) - V_{12,43}(-B)]\ cm^3.C^{-3} \tag{1.14}$$

Similar to resistivity and hall coefficient in VdP samples shown in 1.3.1, If R_{HA} is not equal to R_{HB} within $\pm$ % 10, the specimen is inhomogenous and a more uniform specimen is required. Average Hall coefficient R_{Hav} is shown in Eq. 1.15. Units are in volts for voltages,V, centimeters for thickness, t, amperes for current, I, and Gauss for magnetic field, B.

$$R_{Hav} = \frac{R_{HA} + R_{HB}}{2}\ cm^3.C^{-1} \tag{1.15}$$

Hall mobility can be calculated using the average Hall coefficient, R_{Hav} and resistivity, ρ_{av}

as shown in Eq. 1.16.

$$\mu_H = \frac{|R_{Hav}|}{\rho_{av}}\ cm.V^{-1}.s^{-1} \tag{1.16}$$

Carrier concentration for a n-type semiconductor can be calculated using the average Hall coefficient as shown in Eq. 1.17.

$$n = \frac{1}{R_{Havg} \times q}\ cm^{-3} \tag{1.17}$$

1.3.3 Quantitative Mobility Spectrum Analysis

Quantitative Mobility Spectrum Analysis (QMSA) is a novel method for characterization of diamond films with mixed carrier conduction.

Conventional single magnetic field Hall characterization is not capable of providing a precise determination of the electronic transport properties in materials with mixed carrier conduction. When magnetotransport experiments are performed as a function of magnetic field, one can measure the data to obtain densities and mobilities for each carrier present as shown in the literature [51, 52, 53, 54].

QMSA is the most effective tool to characterize mixed conduction devices. It is possible to decide the number of carriers to fit the data and QMSA is capable of showing how well data fits that parameter without any prior assumption. When systematic temperature analysis are included in the study, more details can be obtained [55].

In the magnetic field dependent Hall Effect measurement, current is applied from terminal 1 to 2 on the Hall bar configuration as shown in Fig. 1.4 and a magnetic field, B_z, is applied perpendicular to the device. By measuring the voltage V_{35} between terminal 3 and 5, the resistivity $\rho(\Omega.Cm)$ is calculated by Eq. 1.18.

$$\rho = \frac{E_x}{J_x} = \frac{V_{35}/d_2}{I_{12}/(W.t)} \tag{1.18}$$

The Hall voltage, V_y, is measured between terminals 3 and 4, and the Hall coefficient $R_H(cm^3C^{-1})$ can be calculated by Eq. 1.19.

$$R_H = \frac{E_y}{B_z J_x} = \frac{V_y/d_y}{B_z I_x/(W.t)} = \frac{d_z V_y}{B_z I_x} \tag{1.19}$$

The carrier concentration $n(cm^{-3})$ and mobility μ are easily obtained from Eq. 1.20 and 1.21.

$$n = \frac{1}{eR_H} \tag{1.20}$$

$$\mu = -\frac{R_H}{\rho} \tag{1.21}$$

The conductivity tensor $\sigma_{ij}(\Omega^{-1}cm^{-1})$ can be calculated from Eq. 1.22 and 1.23.

$$\sigma_{xx}(B) = \frac{qn\mu}{1 + (\mu B)^2} \tag{1.22}$$

$$\sigma_{xy}(B) = \frac{qn\mu^2 B}{1 + (\mu B)^2} \tag{1.23}$$

The sheet resistivity can still be measured when film thickness is unknown as shown in Eq. 1.24.

$$\rho_s = \frac{d_y V_x}{d_x I_x} \left(\frac{\Omega}{sq}\right) \tag{1.24}$$

Sheet resistivity can lead to sheet carrier concentration $n_s(cm^{-2})$. Conductivity tensor can be shown as Eq. 1.25 and 1.26.

$$\sigma_{xx}(B_j) = \frac{en\mu}{1 + (\mu B_j)^2} \tag{1.25}$$

$$\sigma_{xy}(B_j) = \frac{en\mu^2 B_j}{1 + (\mu B_j)^2} \tag{1.26}$$

where e is the electron charge, n is the sheet carrier concentration, B_j is the variable magnetic field, and μ is the electron mobility. For the case of more than one carriers, each carrier can have different electron mobilities.

1.4 This Work

In this work boron doped single crystal diamond (SCD) films were deposited on high pressure high temperature SCD substrates in a microwave plasma-assisted chemical vapor deposition (MPACVD) bell-jar reactor. Dopant concentrations ranged from below 10^{17} cm^{-3} to over 10^{20} cm^{-3} [56].

A high temperature Hall effect system which operates in the temperature range of 300K to 700K was designed and built as a part of this thesis. System capabilities not only include temperature dependent resistivity, carrier concentration and mobility experiments but also include the effects of influences such as temperature stability and non-ohmic contacts on the electronic transport measurements [1].

Temperature dependent Hall effect measurements for p-type single crystal diamond have shown carrier concentrations from below $10^{17}cm^{-3}$ to approximately $10^{21}cm^{-3}$ with mobili-

ties ranging from 763(cm^2/Vs) to 0.15(cm^2/Vs) respectively.

This work is motivated by the investigation of diamond diodes with breakdown voltages of around 1200V, thus an extensive characterization of diamond films are essential. In this work, the developed Hall effect systems was designed with an open architecture which allows us to analyze all of the individual signals measured for both of Van der Pauw and Hall bar configurations from 300K to 700K. Compared to some existing systems, this measurement system includes the capability to accommodate both Van der Pauw and Hall bar (or inline) configurations in order to avoid electrical problems associated with the misalignment of the contacts, distances between the contacts are recorded and taken into account when calculating the Hall voltage according to ASTM standards [50]. Sample geometries are flexible and are not predefined in order to fit to the certain sample holders. This system has a broad range for low voltage measurements for metals as well as resistive materials.

Chapter 2

Temperature Dependent Hall Effect System

2.1 System Setup and Design

2.1.1 System Overview

Temperature dependent Hall effect system is an essential measurement tool for characterizing the temperature dependent transport properties of semiconductors such as resistivity, mobility and concentration. It is also critical for defining the type of mobile charges in a given semiconductor, either as positive or negative. Depending on the type of the charge carriers, a semiconductor can be defined as p or n type.

A new temperature dependent Hall effect system is presented to characterize the properties of new materials, primarily doped diamond films and thermoelectrics. This system is fully software automated, thus, all the inputs can be given to the computer independent of the user's physical location, i.e. a mobile phone access is sufficient to run the data acquisition and measurement system control and to check on the status of the measurements.

Heaters are hooked up to the stage and PID control is embedded to the software. Temperature control of the sample stage is accomplished by proportional-integral-derivative (PID) control of heater cartridges embedded in the oxygen free high conductivity (OFHC) copper

sample stage. Measurements of heating up from 300K to 700K with 25K steps takes less than 7h. Measurements are also taken when cooling back down to room temperature to be able to observe the repeatability of the measurement. The system is capable of computer controlled temperature dependent IV analysis to evaluate the quality of contacts, usually before the Hall voltage measurement since ohmic contacts are needed for accurate results. Temperature dependent I-V measurements also provide insightful information on the influence of annealing and help gain understanding of the impact of non-ohmic contacts on the Hall measurements. Fig. 2.1 shows Hall mobility for a moderately doped diamond sample with ohmic and non-ohmic contacts with comparable values (in the same order of magnitude) but significantly more scatter in the data for the non-ohmic contacts.

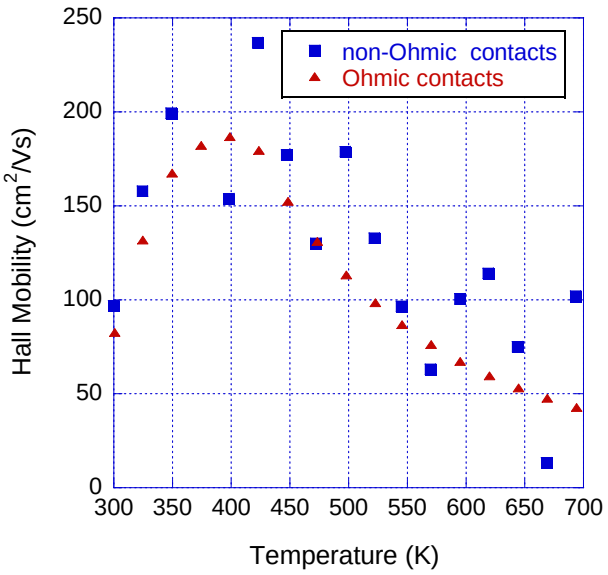

Figure 2.1 Hall mobility data comparison between Ohmic and non-Ohmic contacts for a moderately doped single crystal diamond sample (SND02)

The number of voltage and temperature readings taken can be controlled by the user, saving the average values and standard deviations in the measurement file for evaluation of repeatability and quality of the measurement.

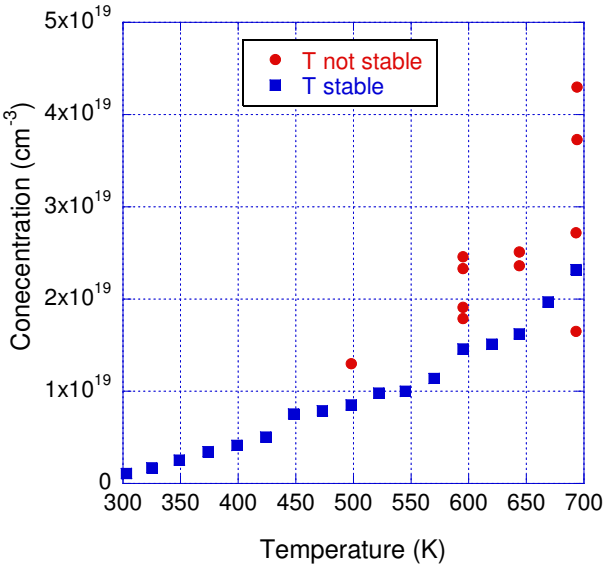

Figure 2.2 Temperature Stability Effects

Diamond was used as a reference sample to investigate the influence of temperature stability on the measured values of concentration as shown in Fig. 2.2. The influence of such non-stable conditions is depicted by the red circular symbols and leads to increased scatter in the measurements.

In this system, as seen in the flowchart, Fig. 2.3, after temperature stability is achieved, the resistivity and Hall coefficient measurements are taken, then the temperature is measured again for comparison. If the temperature has changed more than 2K over the course of the measurements, it is considered not stable and the measurement is repeated. Due to the efficient PID control in this system, same temperature repetitions have not been observed.

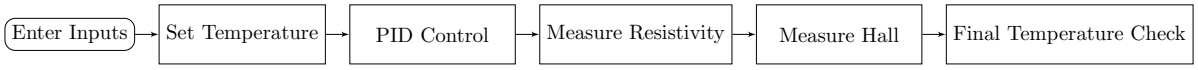

Figure 2.3 Hall Effect System Flow Chart

2.1.2 System Components

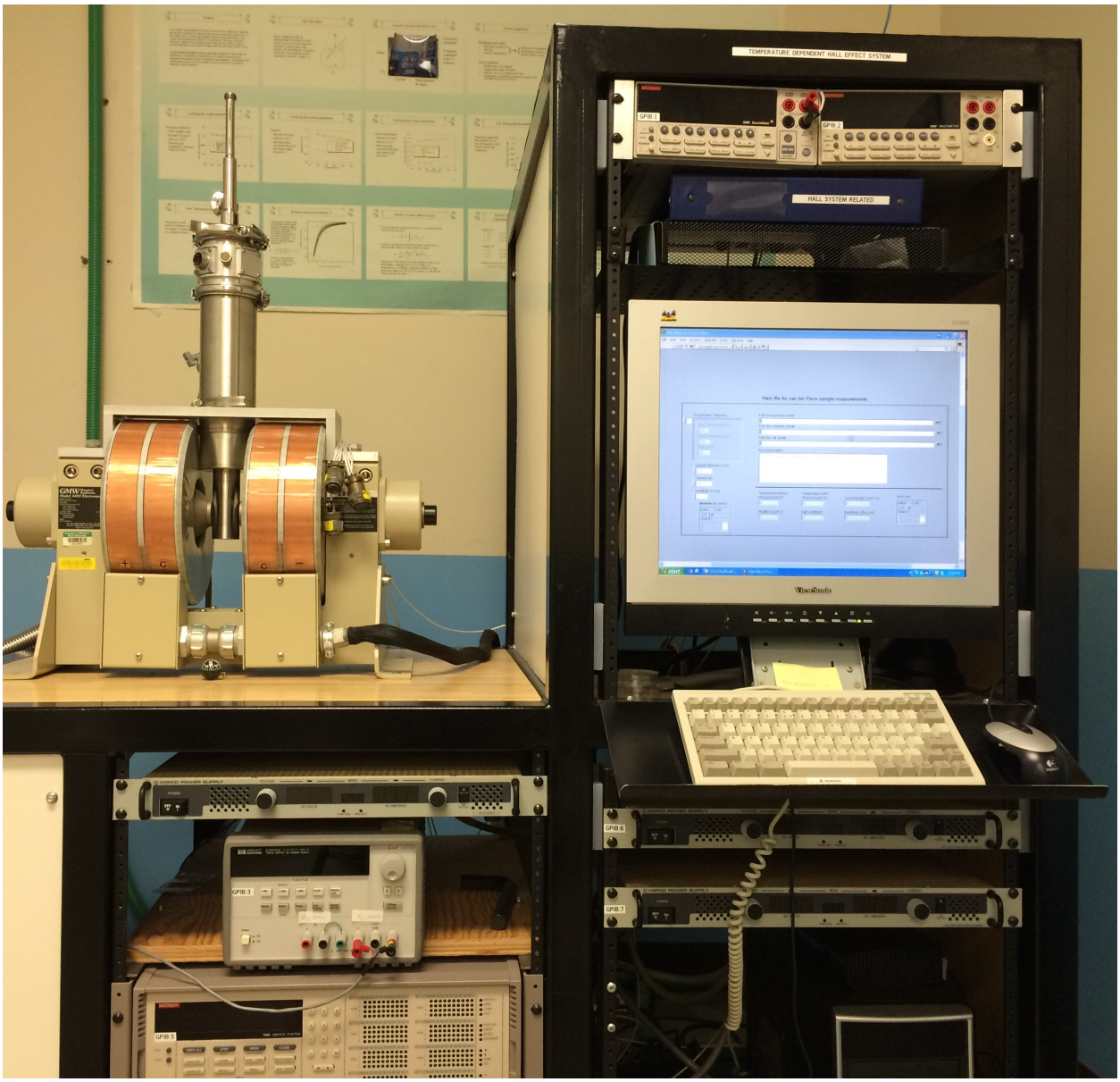

Figure 2.4 Hall Effect System

As seen in the Fig. 2.4, system utilizes a Janis continuous flow cryostat onto which a high temperature measurement stage has been added with heat shields, nichrome heaters, and a copper sample stage. Instruments used include: a source meter (Keithley 2400), a voltmeter (Keithley 2002), a switch system (Keithley 7002), total of three power supplies where two

of them connected to the nichrome heaters (KLP 150 and KLP 300) and the other one connected to the magnet (KLP 75).

Keithley's Series 2400 Source Measure Unit, which can practically be used as a voltage source, a current source, a voltage meter, a current meter, and an ohmmeter, is added as a source meter in this configuration due to the power source characteristics such as low noise, precision, and readback. The multimeter capabilities include but not limited to high repeatability and low noise. It has 0.012% accuracy with $5^1/_2$ digit resolution. The source voltage and measured voltage range from $5\mu V$ to $210V$ and $1\mu V$ to $211V$, respectively; the source current and measured current range from $50pA$ to $1.05A$ and $10pA$ to $1.055A$, respectively. Measurable resistance ranges from $100\mu\Omega$ to $211M\Omega$ and the maximum source power is $22W$. The Keithley 2400 is connected to the computer through a GPIB connection where 520 readings per second can be delivered.

Keithley's Series 2002 Voltage Measure Unit, among other functions, can measure DC voltage, AC voltage, DC current, AC current, two and four-wire resistance, frequency (voltage and current), and temperature (resistance temperature devices or thermocouples).

In this system, Keithley 2002 has been used to measure voltage and temperature. The measured voltage and the measured current range from $200mV$ to $1000V$ and $200\mu A$ to $2mA$ respectively. For temperature measurements with E type thermocouple, there are two possible methods. First one is to read the temperature directly from the meter where temperature range from $-200°C$ to $-1000°C$ with $\pm 0.5°C$ accuracy and second one is to convert the voltage readings into temperature.

The Model 7002 Switch System has been used for van der Pauw samples (VdP). One independent card slot is dedicated to direct the contact pairs to the current source and voltage meter. Use of the 7002 switching system allows for fewer measurement instruments and more

measurement connection configurations to the sample to more accurately measure sample uniformity and to average measurements in different configurations in order to eliminate spurious non-Hall contributions to the measurement.

Magnetic field is provided by GMW magnet system 5403 as seen with the magnetic field sensor in Fig. 2.5. Magnet is powered by the power supply, KLP 75 and provides a magnetic field of 0.7 Tesla.

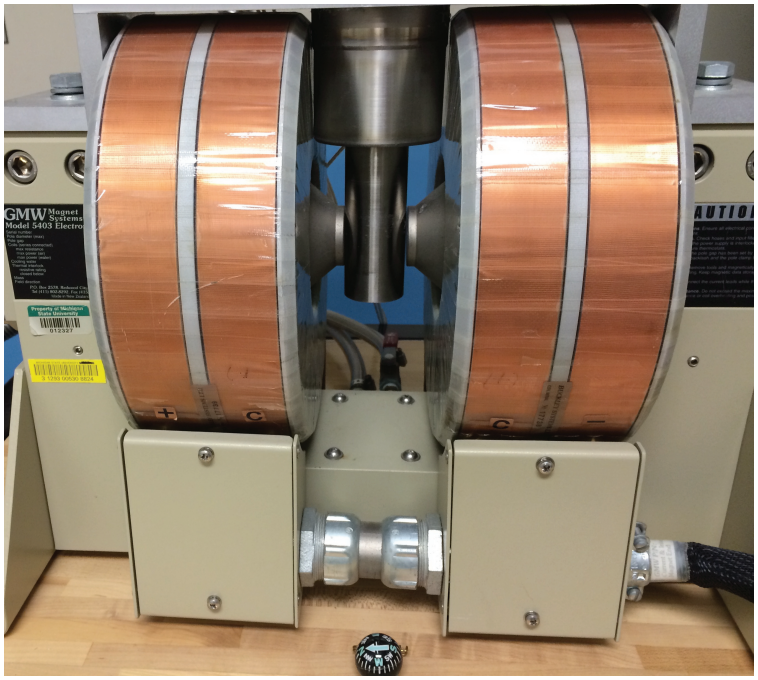

Figure 2.5 Hall Effect System Magnet Components

2.1.3 System Connections

The cryostat chamber is Janis ST100 which includes a 10 pin connector, labeled as connector A, there are two separate connectors to connector A, one for samples with VdP (Van der Pauw) geometry and one for Hall bar (in-line) geometry. Cryostat also includes a separate 19 pin connector, labeled as B, which stays connected during the measurement independent from the sample type. The schematic for the 19 pin connector can be seen in Fig. 2.6.

Wiring see from outside of the connector

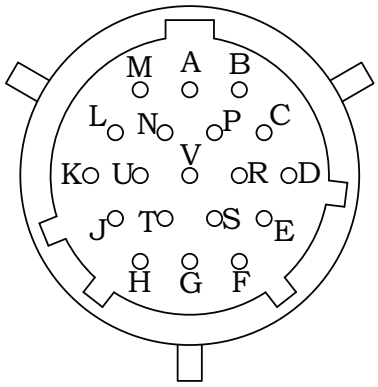

A	Anode (+) of Si diode on cryostat
B	Anode (+) of Si diode on cryostat
C	Cathode (-) of Si diode on cryostat
D	Cathode (-) of Si diode on cryostat
E	Power (+) to HT stage heater #1
F	Power (-) to HT stage heater #1
G	Power (+) to HT stage heater #2
H	Power (-) to HT stage heater #2
J	Power (+) to cryostat heater in epoxy
K	Power (-) to cryostat heater in epoxy
L	Type E - TC #1 (+) chromel
M	Type E - TC #1 (-) constantan
N	Type E - TC #2 (+) chromel
P	Type E - TC #2 (-) constantan
U	Type E - TC #3 (+) chromel
V	Type E - TC #3 (-) constantan

Figure 2.6 Stable Connections

Connector B is connected at all times during the measurement, independent from the sample type, either VdP or in-line geometry. Through the connector B, two nichrome stage heaters, each are sandwiched between the aluminum nitride plates, are connected to two Kepco power supplies. The nichrome heaters are the main part of the PID control system which is custom designed and software automated and will be explained in further detail in the following sections. Three E type Omega thermocouples are connected to the Keitley 2002 rear card, channel one and two. The third thermocouple is currently not active. The main reason for using E type thermocouples, which are combinations of chromel (nickel-chromium) and constantan (copper-nickel), is the low sensitivity to the magnetic field. Ten readings of the thermocouple voltage are averaged and saved to the data file along with the standard deviation.

For VdP samples, the connection schematic can be seen in Fig. 2.7. After Physical Vapor

Deposition (PVD) of metal contacts, silver paste was used to connect $50\mu m$ diameter gold wires to the contacts. Several pastes were investigated for electrical connection to the samples including a water based silver paste, an alcohol based silver paste, and a carbon paste. The water based silver paste was found to easily detach from the sample during the measurements, and the carbon paste was challenging to apply, required significant preparation time, had a shorter shelf-life, and was difficult to remove from the sample after the measurement. The alcohol based silver paste was found to be a good choice for ease of mounting, long shelf-life, ease of removal, and good repeatability in the measured data through several temperature cycles of data collection.

As part of the research for this dissertation, software was developed in the LabVIEW programming environment for system control and data acquisition. The measurement steps were programmed to follow the ASTM standard [50] for Hall effect measurements. The software was developed such that individual subroutines could be run independently allowing for open access to various measured values and open access testing of the samples. This is a critical feature of the system that empowers the user to troubleshoot measurement difficulties, further investigate unexpected results, and rapidly reconfigure the software control to develop new measurements. All voltage and current readings are averaged after taking ten measurements along with the standard deviations and the user is able to change the settings through the graphical user interface (or front panel) of the program. As a custom built open access system, user can be able to change the settings through the front panel of the program.

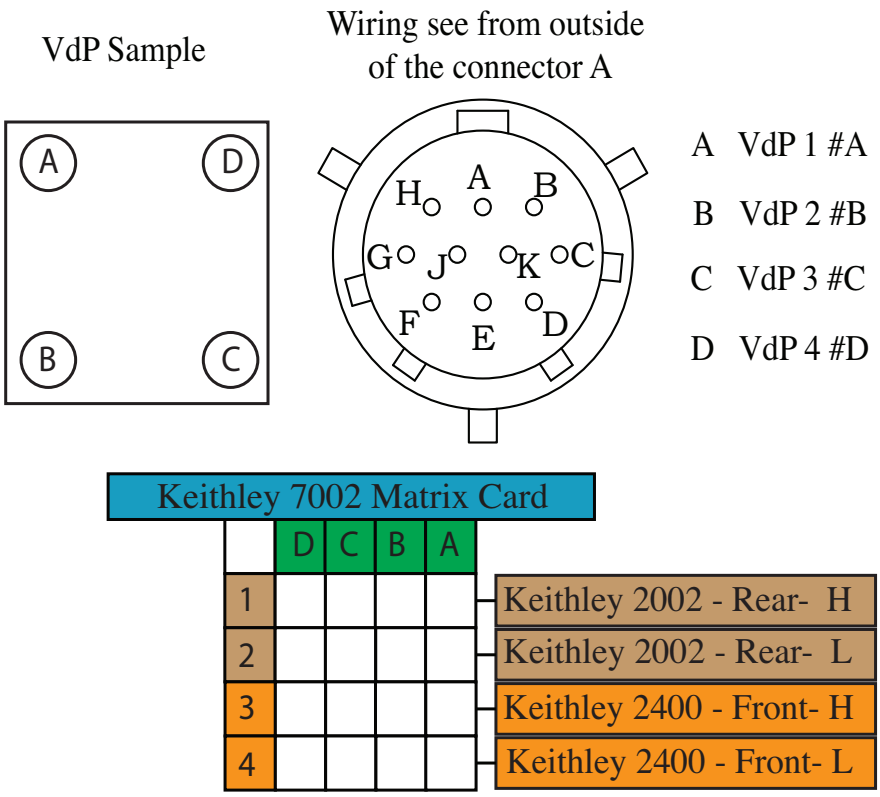

Figure 2.7 Van der Pauw Sample Connections

For the in-line samples, connection schematic can be seen in Fig. 2.8. After metal deposition of the contacts, 6 or 8 connections are made to the sample with $50\mu m$ thick gold wires attached using silver paste. All voltage and current readings are the average of ten measurements and recorded to a file along with the standard deviations.

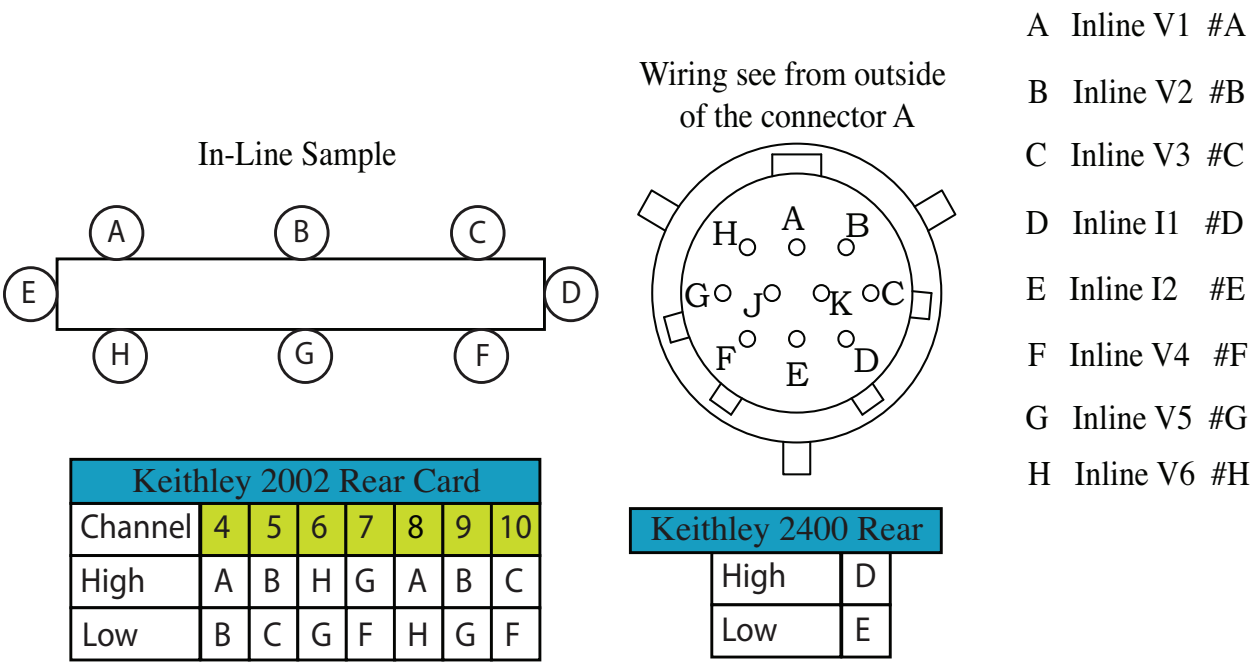

Keithley 2002 Rear Card							
Channel	4	5	6	7	8	9	10
High	A	B	H	G	A	B	C
Low	B	C	G	F	H	G	F

Keithley 2400 Rear	
High	D
Low	E

Figure 2.8 In Line Sample Connections

2.2 Sample Mounting Procedure

Both evaporation and sputtering of the metal contacts have been investigated. Both deposition techniques resulted in ohmic contacts after annealing. The e-beam evaporation system used allows for up to four different deposition materials in a single run. The sputtering system accommodates two sputtering targets and the total runtime is shorter due to the higher deposition rate and the less stringent vacuum requirements prior to starting the deposition. Thus, sputtering was more frequency used in this research.

Metals for ohmic contact fabrication are chosen by the electron affinity of the material and the work function of the metal which will be further discussed in Chapter 4. For the boron doped single or poly crystalline p-type diamond films, ohmic contacts are commonly formed by a Ti and Au layered structure, with thicknesses of $30nm$ and $100 - 300nm$ respectively.

For phosphorus doped single crystal n-type diamond films, in addition to Ti/Au, Al contacts are also widely used.

For thermoelectric or heavily doped samples, silver paste is sufficient to obtain ohmic contacts. Thus, no additional metal deposition is necessary.

The sample stage (Fig. 2.9) is made out of oxygen free high conductivity (OFHC) copper. For uniform temperature, a cylindrical copper shield surrounds the sample stage and consists of two copper cylinders - one inside the other with a thin sheet of thermal insulation between them. A screw at the end of the shield hold it in place. A thin plate of aluminum nitride electrically isolates the sample from the copper stage while providing good thermal connection and high temperature compatibility. Sample to be measured is then placed on an aluminum nitrite plate and wiring process is performed using silver paste under the microscope. The $50\mu m$ diameter gold wires are attached to the sample with silver paste which is allowed to dry for approximately 30 minutes. Care is taken during sample mounting to adjust the Au wires so there is no shorting of the wires to the copper shield, copper stage, or to other wires.

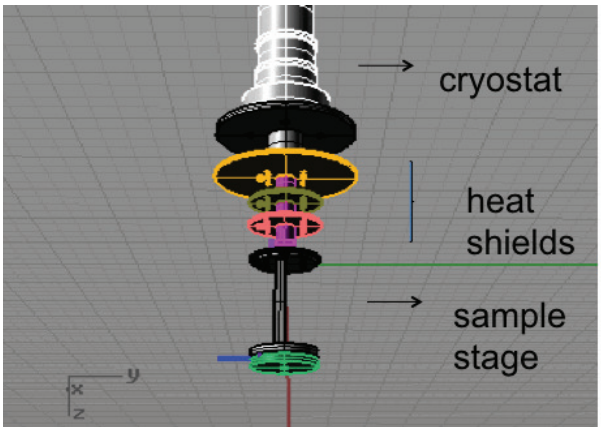

Figure 2.9 Hall Effect System Sample Stage

Once the sample is mounted into the system, the cryostat is carried from the microscope back to the Hall effect system. The sample orientation should be made perpendicular to the magnetic field. This orientation can be found by running some of the subroutines developed and monitoring the Hall voltage while adjusting the rotation of the cryostat relative to the magnetic field. When the Hall voltage reaches a maximum value, the proper orientation is established. Rough pump is turned on followed by the turbo pump. After this process, all of the measurements steps can be also operated by remote access, i.e. laptop or a smart phone. Once the required vacuum level is reached, a current versus voltage measurement sequence is initiated to study the effects of annealing on the ohmic nature of the contacts. Due to the temperature dependent IV measurement capabilities of the system, annealing effects can be simultaneously monitored starting from room temperature up to $750K$. The system can also by cycled in temperature a number of times (defined by the user) so repeatability studies can also easily be done. The switching system allows the user to monitor the IV measurements for 6 different contact pairs, including the neighbor and diagonal contacts which can be

chosen for VdP samples through the LabVIEW software. Thus, one can compare different contact pairs and confirm that they are sufficient to start the resistivity and Hall effect measurements at temperatures ranging from $300K$ to $750K$.

2.3 PID Control

The influence of temperature stabilization was shown in Fig. 2.2 and the importance of temperature stabilization is highlighted in the ASTM F76 Hall effect measurement standard. A program was therefore developed for temperature control and was based on the Ziegler Nichols method [57]. PID control is a form of feedback to obtain robustness. Instability is a risk unless the PID loop is properly tuned.

As Loo [58] explained in her Ph.D thesis, PID includes three components: Proportional (P) - also known as Gain, Integral (I) - also known as Automatic Reset or Reset, and Derivative (D) - also known as Rate.

The algorithm is commonly used in the following forms:

- Proportional only (P)
- Proportional and Integral (PI)
- Proportional, Integral and Derivative (PID)
- Proportional and Derivative (PD)

In a PID control system, response of the controller to an error, the degree to which the controller overshoots the set point and the degree of the system oscillations are the main parameters to take into account in order to build an efficient temperature control [59].

2.3.1 Proportional Control

The proportional term generates an output value that is proportional to the present error value. The proportional response can be tuned by multiplying the error by a constant, P, called the proportional gain constant.

P applies power, W, to the heater in proportion to the difference in actual temperature and the set-point. In terms of performance, proportional gain is preferable to an On-Off type controller.

$$W = Px(T_s - T_0) \tag{2.1}$$

T_s is the set temperature point and T_0 is the actual temperature of the system. In the presence of a large gain, the system responds faster to changes, however also becomes progressively under damped and eventually unstable. Contrarily, a small gain results in a relatively smaller output response to a large input error and a less sensitive controller.

2.3.2 Proportional + Derivative Control

High proportional control, P, can cause instability and overshoot problems. In order to eliminate this, a derivative gain or damping constant, D, can be added to the control which slows the rate of change of the controller output. In order to calculate the derivative of the process error, slope of the error over time (rate of change) is determined and multiplied by the derivative gain D.

In proportional and derivative, PD, control, a D term is added proportional to the time-derivative of the error signal.

$$W = Px\left((T_s - T_0) + Dx\frac{d}{dt}(T_s - T_0)\right) \tag{2.2}$$

D can be adjusted to achieve an optimally damped response. Too high damping will cause the system to be slow to stabilize, on the other hand, too low damping will result in overshoot.

2.3.3 Proportional + Integral+ Derivative Control

PD control can overcome the overshoot problems, however, accelerating the movement of the process towards set point and eliminating the residual steady-state error can be achieved by adding the integral term, I, to the function which is proportional to both the magnitude of the error and the duration of the error. The integral in PID controller is the total of the instantaneous errors over time and gives the accumulated offset which should have been corrected previously. The accumulated error is then multiplied by the integral gain, I, and added to controller output [60]. Due to fact that the integral term responds to accumulated errors from the past, it can cause the present value to overshoot the set point value. To prevent this condition from occurring in our work, we have introduced error reinitialize functions to the PID control software in LabVIEW environment.

$$W = Px\left((T_s - T_0) + Dx\frac{d}{dt}(T_s - T_0) + Ix\int(T_s - T_0)dt\right) \tag{2.3}$$

D term has not been used in our system, however it is commonly used to reduce the magnitude of the overshoot produced by the integral component and to improve the combined controller process stability. I term is used to change the heater power until the time averaged value of the temperature is zero.

For manual tuning, first I and D values are set to zero. Then the P is increased until periodic oscillations are observed, then P should be set to approximately half of that value for a quarter amplitude decay response. Then I is increased until any offset is corrected in sufficient time for the process. Too high I values will cause poor temperature stability. Finally increase D if required, until the loop is acceptably quick to reach its reference after a load disturbance. Too high D values will cause overshoot in the temperature. A fast PID loop tuning usually overshoots slightly to reach the set point more quickly, then stabilizes at the set temperature [61]. Effects of increasing a parameter independently are summarized in Table 2.1.

Parameter	Rise time	Overshoot	Settling time	Steady-state error	Stability
P	Decrease	Increase	Small change	Decrease	Degrade
I	Decrease	Increase	Increase	Eliminate	Degrade
D	Minor change	Decrease	Decrease	No effect in theory	Improve if small

Table 2.1 PID Manual Tuning [6]

2.3.4 PI Control in This System

For this system a custom made temperature controller is designed using two nichrome heaters and two power supplies controlled by LabVIEW program. Maximum allowed current for the power supplies are set to $2.5A$.

In order to determine the optimum PI parameters, for fixed temperatures over the measurement range, between 300K-700K, the proportional gain was incrementally increased until stable temperature oscillations were observed as seen in Fig. 2.10.

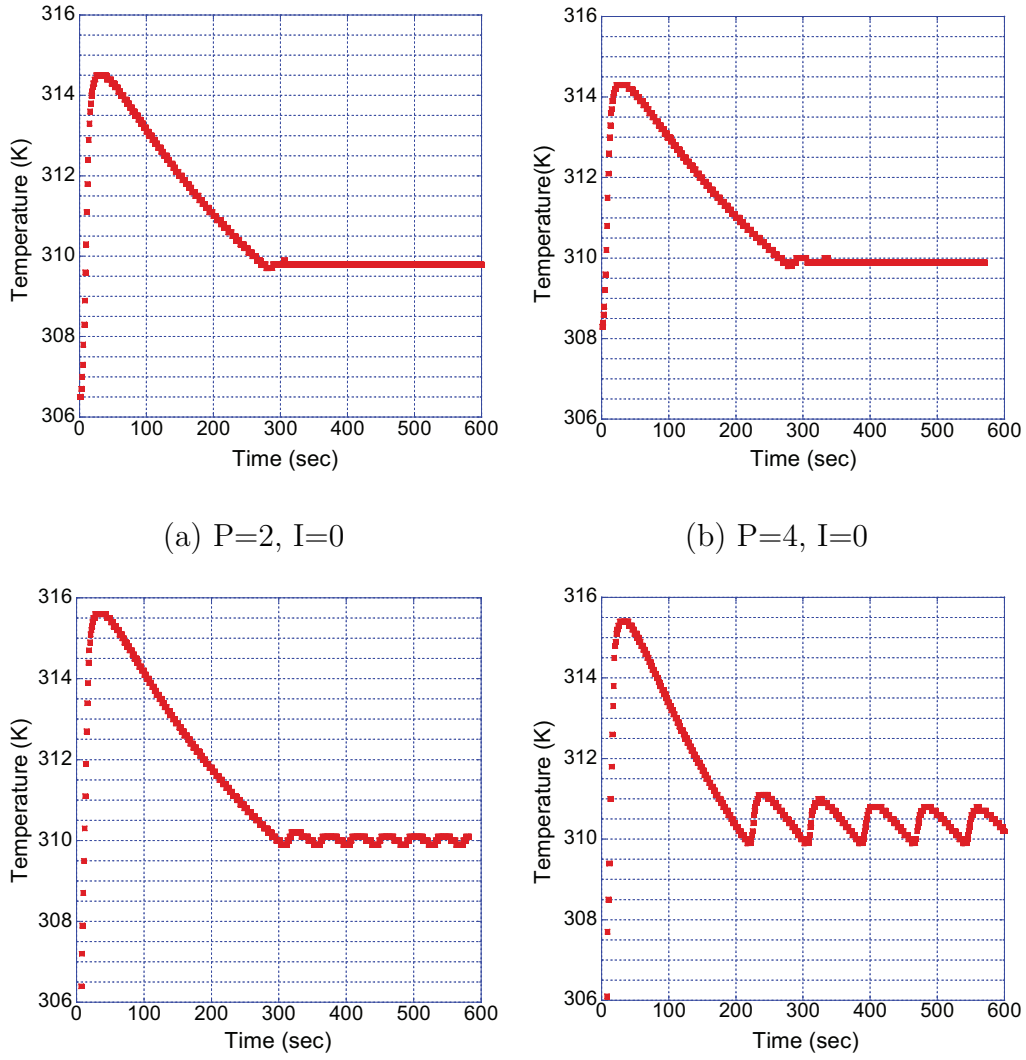

(a) P=2, I=0

(b) P=4, I=0

(c) P=8, I=0

(d) P=16, I=0

Figure 2.10 Effect of Proportional Gain to Temperature Stabilization

The proportional gain was then decreased to 0.45 of the value for sustained oscillations, and the period of these oscillations was used to determine the integral value as 1.2 times the proportional gain over the period of oscillation. This procedure was follwed by fine tuning the PI parameters in LabVIEW. The derivative gain was set equal to zero as summarized in Table 2.2.

Control Type	K_p	K_i
P	P_{OSC}	-
PI	$0.45P_{OSC}$	1.2P/T

Table 2.2 PI Control Summary Table

After the fully automated PID control software program is established. Temperature control consists of the following steps to achieve stabilization:

- Read the gain, P and the *integral* coefficients from the table which is created by optimizing and fine tuning the parameters for that temperature range.
- Save the data and execute the program when the following three conditions are met (i)Actual temperature is in the set temperature limits (ii) Actual temperature remains in the set temperature limits for 300 seconds (iii) Standard deviations of the last 1000 temperature readings are lower than 0.2.

This procedure gave satisfactory results over the temperature range of $300 - 750K$ with temperature variation less than $2K$ within the 7 minute long Hall effect and resistivity measurement.

In Fig. 2.11, PID control efficiency for this system can be seen between the temperature range of $300K$ to $500K$ with $50K$ temperature steps. Less than $5min$ is sufficient in order to reach to a stable temperature point.

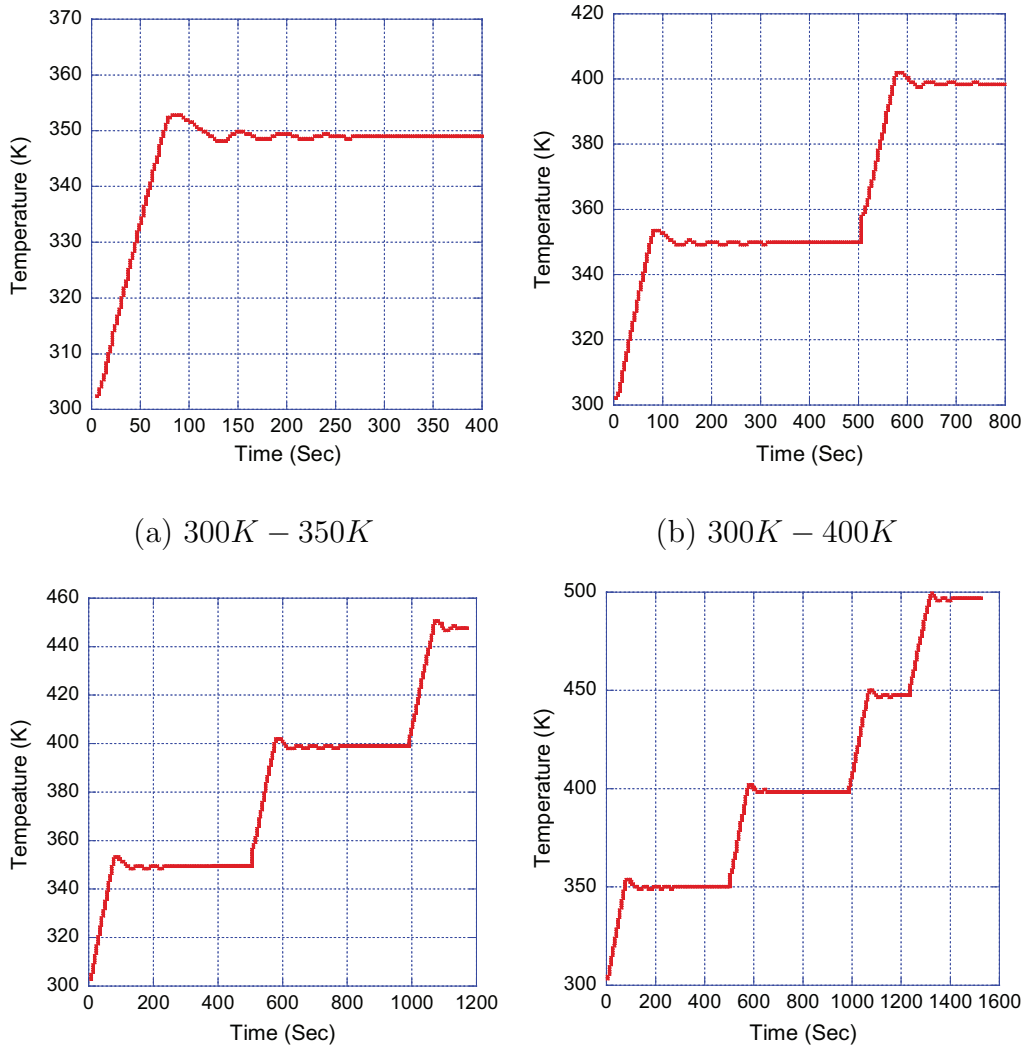

(a) $300K - 350K$

(b) $300K - 400K$

(c) $300K - 450K$

(d) $300K - 500K$

Figure 2.11 Temperature vs time representation for the PID control

2.4 Software Control

Except for the vacuum pumps, all of the instruments in the system are controlled by software developed in LabVIEW. The communication between the instruments and the computer is through GPIB address cables. Expected input values are the sample geometry, number of voltage and current readings to average, applied current value, temperature range with step

size and location of the measurement data file to be saved. Data is saved in three *.txt* files, one includes a summary data of resistivity, carrier concentration and mobility for all the temperature values and the other two data files include all the details of the measurement including the standard deviations for resistivity and Hall measurements, respectively. For samples with Van der Pauw geometry, in addition to the input values given above, thickness of the sample is a user input to the program. For samples with in-line (Hall bar) geometry, additional inputs are thickness and the width of the sample and distance between the contacts.

Once the user inputs are entered into the user interface of the LabVIEW program, the automated measurement starts running and it typically takes about 7 hours for resistivity and Hall effect measurements from $300K$ to $700K$ with $25K$ steps. During the measurement, the system can be remotely accessed through a smart phone, tablet or a laptop independent of the user's physical location. Measurements start with the PID control program to achieve a stable temperature point, once the set temperature point is achieved and stabilized, resistivity measurements are taken and saved into the data sheet, followed by the Hall effect measurements. After all of the measurements are taken at a certain temperature point, temperature is measured again and if it is less than $\pm 2K$ compared to the start temperature, the system moves to the next temperature set point. If the temperature difference is more than $\pm 2K$, the same temperature point is repeated and saved, until the ASTM conditions are met. Currently, in this system, due to the efficient PID control system built, temperature set point repetitions have not been observed.

Chapter 3

Measurement Results

Hall effect measurement is a very important technique for understanding the electrical conduction properties of semiconductors such as carrier density, electrical resistivity, and the mobility of carriers. It is also critical for defining the type of mobile charges in a given semiconductor, either as positive or negative, depending on the type of the charge carriers, a semiconductor can be defined as p or n type. This temperature dependent Hall effect system has been tested between 296-700K and for both in-line and van der Pauw samples. Resistivity and Hall measurements of n and p type GaAs and Ge materials with known properties has been measured as reference materials.

This system is fully software automated, thus, all the inputs can be given to the computer independent from user's physical location, i.e. a mobile phone access is sufficient to run the whole experiment. The typical time for measurements over the $300K$ to $700K$ temperature range with $25K$ steps takes less than 7 hours. Measurements are also taken when cooling back down to room temperature to be able to observe the repeatability of the measurement.

Temperature dependent IV measurements also provide critical information for observing the annealing effects specifically when the contacts are deposited on the sample with physical vapor deposition (PVD), e-beam or sputtering methods, thus, unexpected measurement results due to contacts can be easily detected and solved.

3.1 Reference Materials

3.1.1 p-Type GaAs

Before deposition of metal contacts, silver paste has been used to make contacts to the material. Current versus voltage (or I-V) measurements as seen in Fig. 3.1 show ohmic behavior only at $700K$ when no metal contacts have been deposited to the sample. This measurement process to 700K also anneals the contacts. After annealing, the sample is cooled back to $300K$ and another I-V measurement is taken for comparison to the pre-annealing data. The after annealing data are labeled as $300K_{AA}$ in Fig. 3.1 which shows that the I-V behavior changed after annealing, but remained non-ohmic.

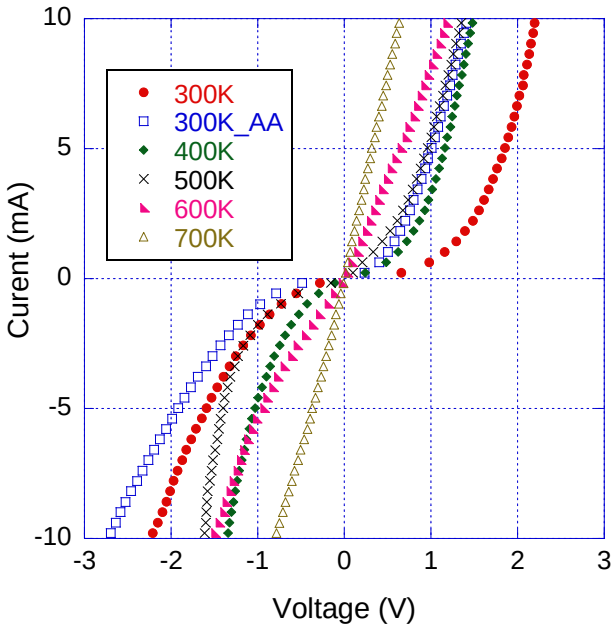

Figure 3.1 Temperature dependent IV curve for p-type GaAs without contact deposition

Resistivity and Hall effect measurements were taken on this p-type GaAs sample with the silver paste contacts in order to investigate the influence of non-ohmic contacts on the measured data.

In order to compare the effects of metal contacts custom made e-beam target (80wt% Ag, 10wt% In and 10wt% Zn) was used to deposit metal contacts on the four corners of the VdP sample. As Fig. 3.2 shows, the contacts initially showed non-ohmic behavior, however the I-V measurements became linear above approximately $500K$ and remained ohmic after annealing and cooling back to room temperature.

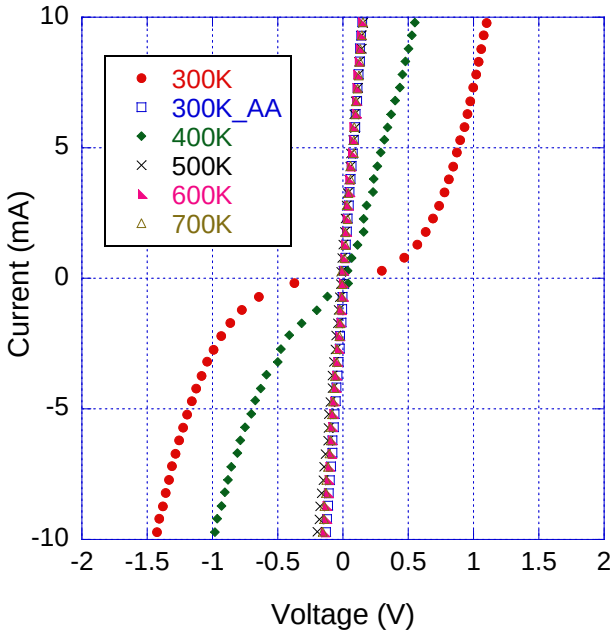

Figure 3.2 Temperature dependent IV curve for p-type GaAs with contact deposition

After achieving ohmic contacts, resistivity and Hall measurements were taken with different applied current levels to investigate the effect of applied current as seen in Fig.3.3, 3.4 and Fig. 3.5. No significant dependence on the applied current level could be seen as would be expected for low resistance contacts and high uniformity in the sample.

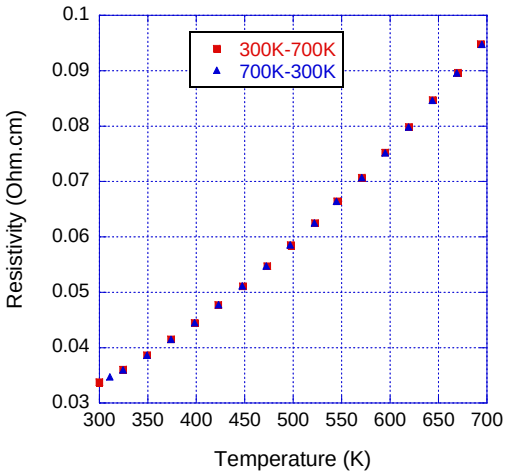

(a) I=20mA

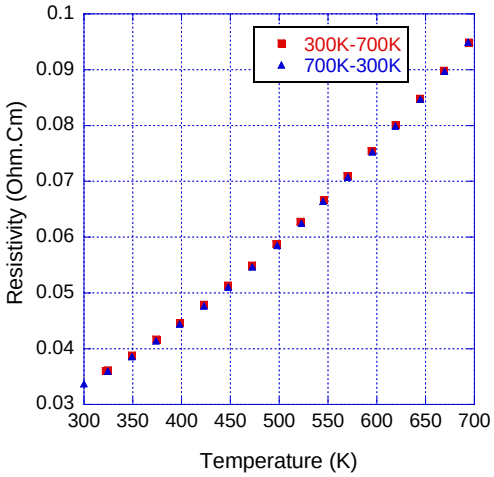

(b) I=15mA

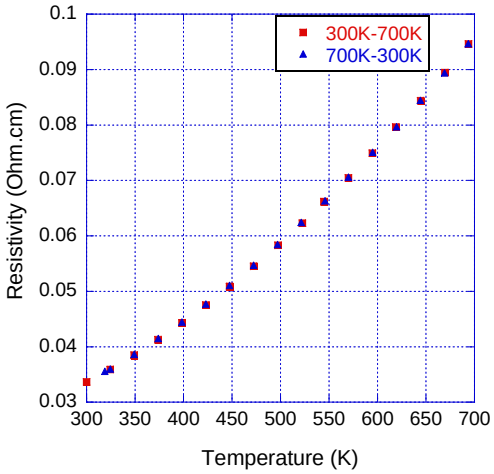

(c) I=10mA

Figure 3.3 Temperature dependent resistivity for p-type GaAs

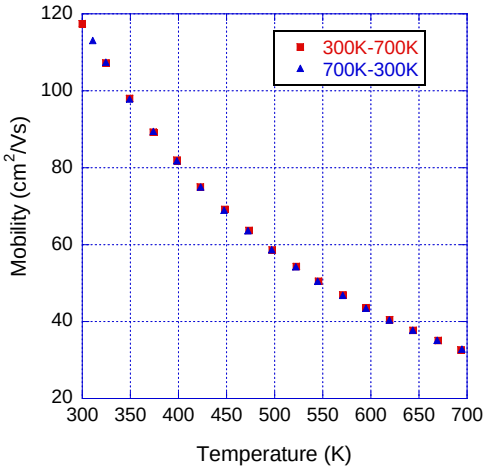

(a) I=20mA

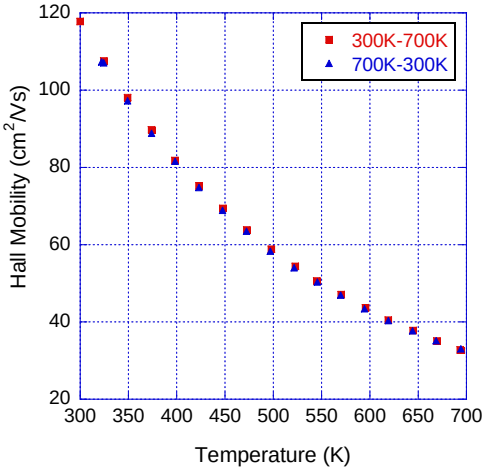

(b) I=15mA

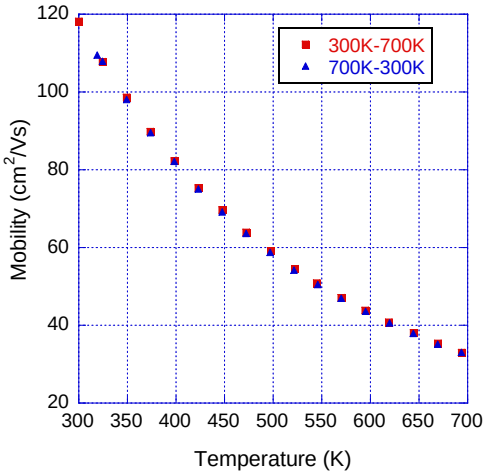

(c) I=10mA

Figure 3.4 Temperature dependent mobility for p-type GaAs

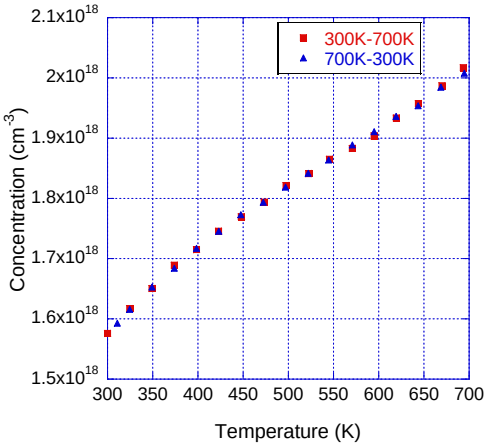

(a) I=20mA

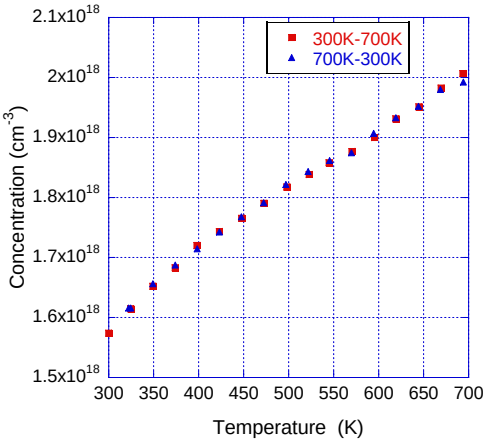

(b) I=15mA

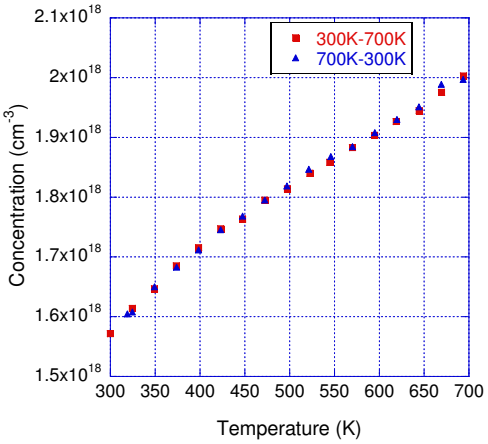

(c) I=10mA

Figure 3.5 Temperature dependent carrier concentration for p-type GaAs

3.1.2 n-Type GaAs

To test the measurement system, both p-type and n-type samples of GaAs were measured as reference samples. In addition, the influence of temperature stability was studied to see the effects of PID temperature control. Both van der Pauw (VdP) and Hall bar sample geometries were investigated with the n-type GaAs samples. Metal contacts to the samples were deposited by e-beam evaporation of target material made of (90wt% Ag, 5wt% In and

10wt% Ge). was used to deposit metal contacts on the four corners of the VdP and two ends of the Hall bar sample. The typical measurement procedures begin with current vs. voltage behavior of various contact pairs. This is repeated at various temperatures to investigate the annealing effects on the contacts. The IV measurements for contacts from one edge to the other of a Hall bar shaped sample of gallium arsenide show non-ohmic behavior until 650K above which linear IV behavior is found. After this annealing step to 700K, the IV behavior remained Ohmic even down to 300K as seen in Fig. 3.6.

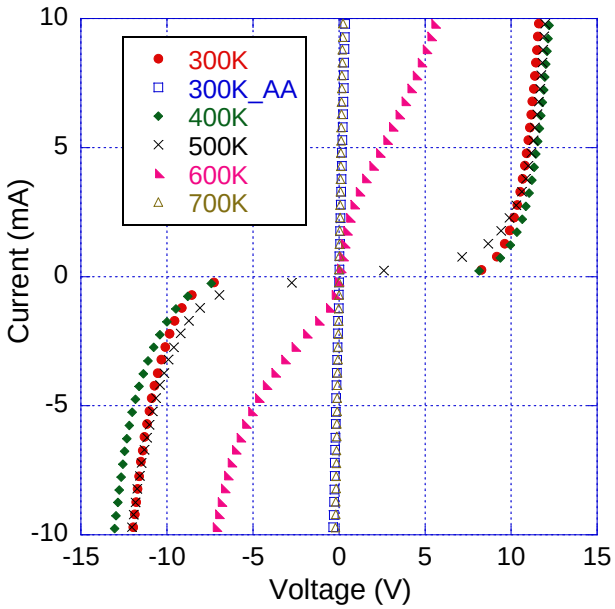

Figure 3.6 Temperature dependent IV curve for n-type GaAs with deposited metal contacts

Mobility data collected is in a good agreement with two different sample configurations, (VdP and Hall bar) and literature values [62] as seen in Fig. 3.7.

Temperature dependent carrier concentration can be seen from 300K-700K and 700K-300K in Fig.3.8 where $N_D = 6.3x10^{16}cm^{-3}$ at near room temperature.

To test the system accuracy we compared our results to those shown by Ioffe for comparably doped GaAs samples. For both van der Pauw and Hall bar configurations we showed

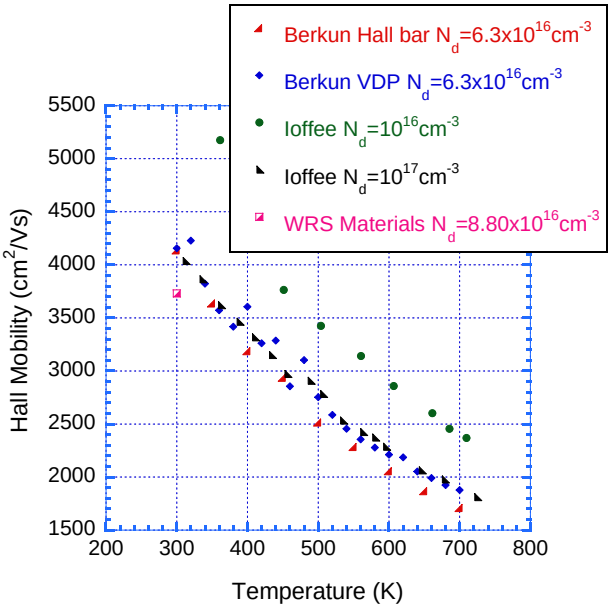

Figure 3.7 Temperature dependent mobility comparison for n-type GaAs with contact deposition

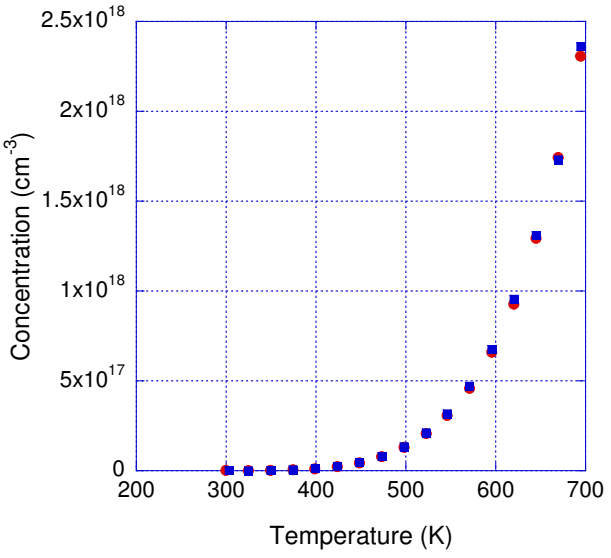

Figure 3.8 Temperature dependent concentration for n-type GaAs contact deposition

good agreement of the room temperature carrier concentrations reported by the sample manufacturer (WRS Materials). We also compared temperature dependent results with semi-empirical fit values given by Christou and Webb that we labeled as theory in our error analysis [63]. We found less than 20% difference with the theoretical values over the 300K-700K range, and less than 8% difference with the values reported for the $N_D = 10^{17} cm^{-3}$ sample reported in literature (Ioffe) [62].

3.1.3 p-Type Ge

For an additional reference material, p-type Ge was purchased from WRS Materials with known resistivity (0.01-0.04 $\Omega.cm$ at 300K), are performed. Annealing effects at 700K to current vs. voltage behavior is presented in Fig. 3.9.

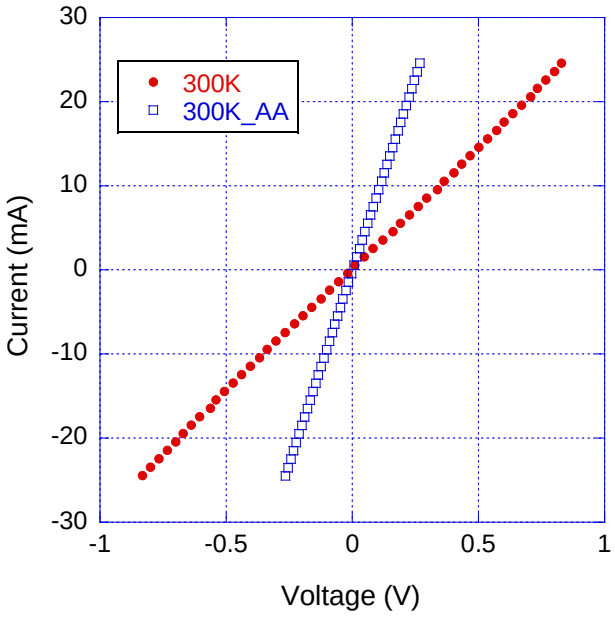

Figure 3.9 IV curve for p-type Ge

Measurements for resistivity show a good agreement with the given company values at 300K as shown in Fig. 3.10a. Measurements taken from 300K up to 700K and from 700K

back down to 300K, show the repeatability of the experiment.

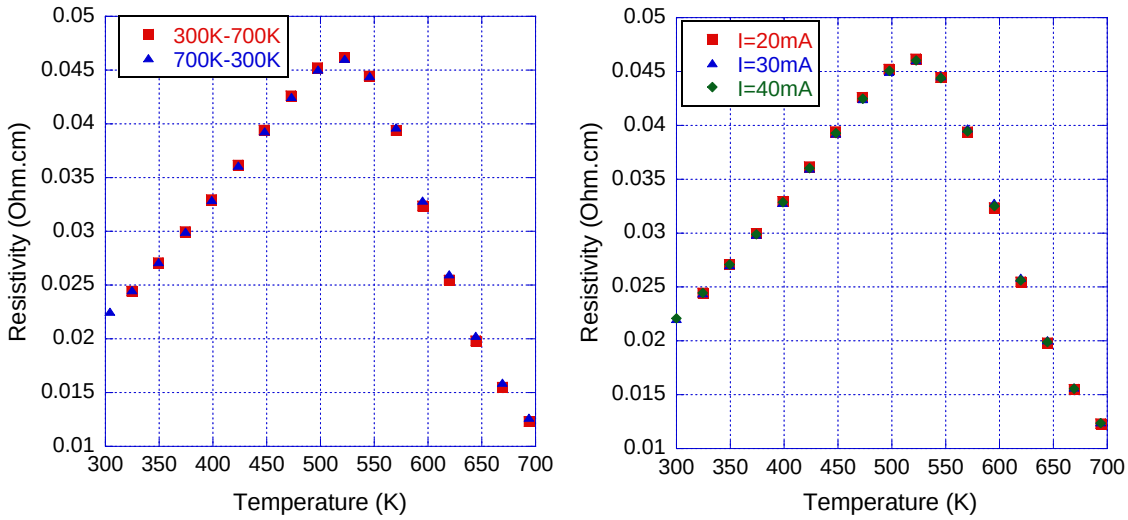

(a) Fixed current

(b) I=20,30 and 40mA

Figure 3.10 Temperature dependent resistivity for p-type Ge

Effects of the applied current level to the resistivity measurements also have been studied for applied current values of 20, 30 and 40mA. As expected, resistivity data is repeatable for all three current levels as shown in Fig. 3.10b.

At room temperature, measured resistivity is around 0.22 $\Omega.cm$ which corresponds to a concentration value around $3.5x10^{17}cm^{-3}$ according to semiconductor physics calculations [11] which falls in agreement with the measured concentration shown in Fig. 3.11a and 3.11b. There is a repeatable discontinuity in the measurement between 550K - 600K due to the transition from extrinsic region to intrinsic region.

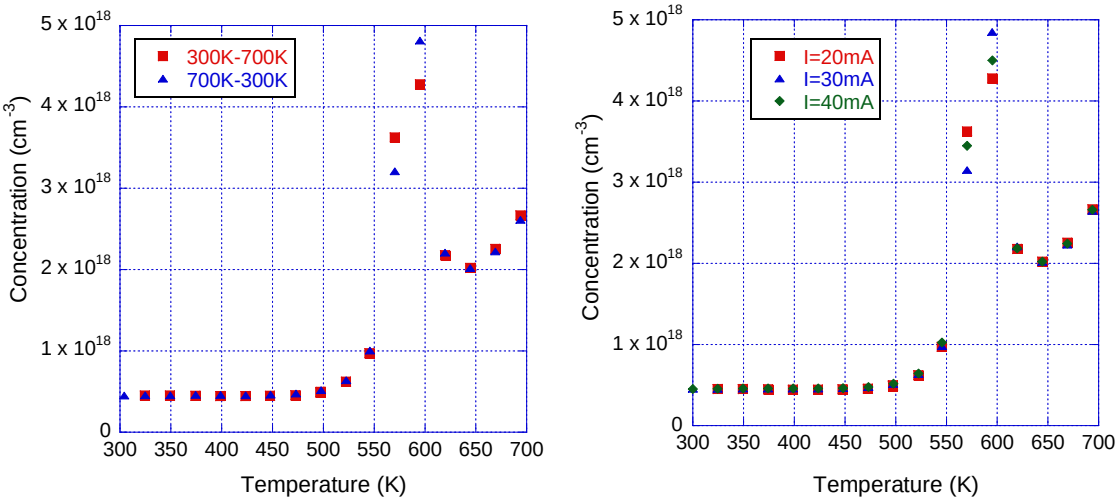

(a) Fixed current (b) I=20,30 and 40mA

Figure 3.11 Temperature dependent carrier concentration for p-type Ge

Extrinsic to intrinsic transition temperature range between 550K-600K which is repeatably observed in the temperature dependent mobility measurements as seen in Fig.3.12a and Fig. 3.12b.

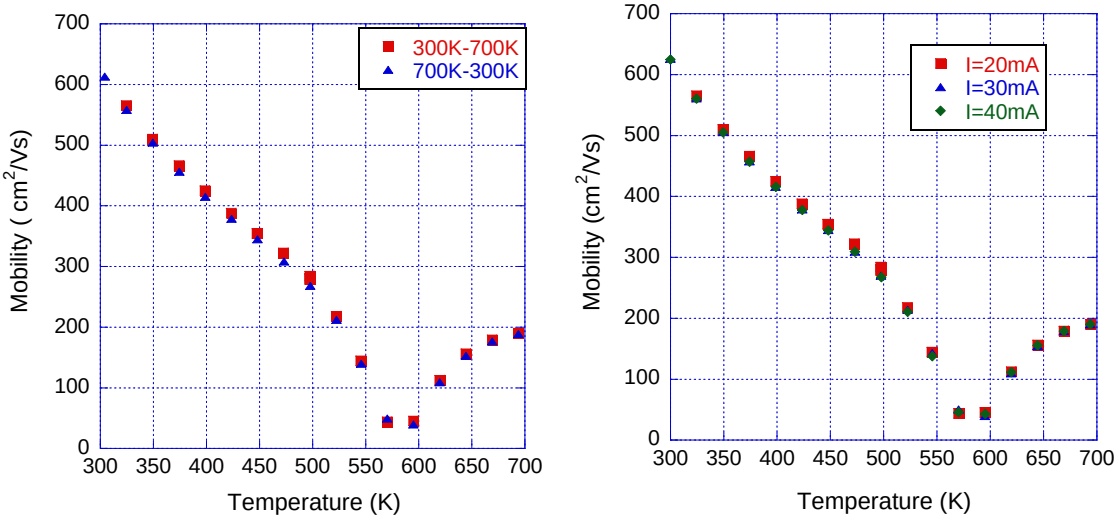

(a) Fixed current (b) I=20,30 and 40mA

Figure 3.12 Temperature dependent mobility for p-type Ge

Reference materials show good agreement between the measured transport properties, company given values and physical equations and can be used to calibrate the system regularly.

3.2 Single Crystal Diamond

3.5 mm 3.5 mm high pressure, high temperature (HPHT) substrates from Sumitomo Electric have been used to deposit the single crystal boron doped diamond films. Films are grown on top of the substrates using a microwave plasma-assisted CVD reactor [64], as reported in previous investigations [56]. Samples are acid cleaned and hydrogen plasma etched followed by the PVD deposition of gold or titanium/gold near the four corners of the sample for van der Pauw measurements as reported in our previous work [1].

For gold contacts, in order to achieve adhesion, a fine mesh technique has been developed using a transparency mask with four identical holes near the corners and a fine mesh structure similar to a TEM grid. Technique includes the following steps: (I) Hydrogen termination of the sample surface (II) Au deposition with mask and mesh structure (III) Removal of the mask and mesh structure (IV) Oxygen termination of the sample surface and (IV) Au deposition with mask. Samples are then oxygen plasma treated to remove surface conductivity effects. Ohmic contacts with good adhesion have been achieved via this technique. For Ti/Au contacts, annealing was sufficient to observe ohmic contacts without additional process steps.

3.2.1 Influence of Ohmic contacts

The influence of Ohmic and non-Ohmic contacts to the Hall effect measurements was studied as a part of this work. Near the origin of the current vs. voltage plots, non-Ohmic curves such as the one shown in Fig. 3.13 as dashed line for a 500K IV measurement were observed for the moderately doped diamond sample. In order to study the effects, temperature dependent measurements were taken for this sample, then the contacts were cleaned off, and new contacts deposited on the same sample. The new contacts exhibited Ohmic behavior as shown in straight line at 500K.

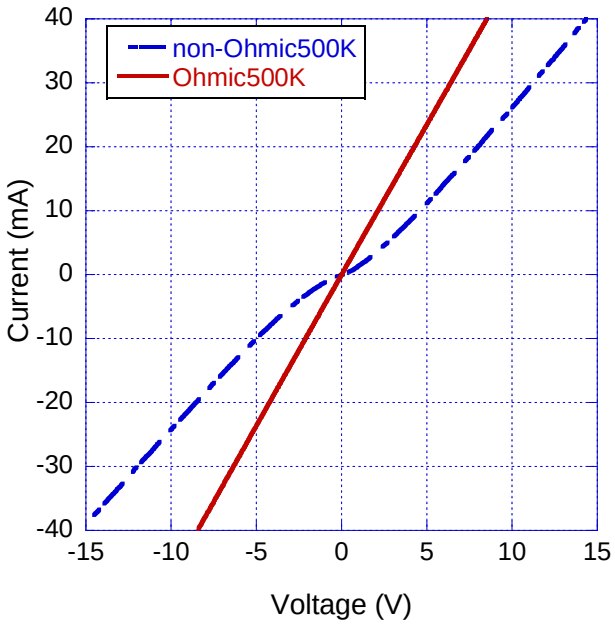

Figure 3.13 Current vs. voltage comparison for Ohmic and non-Ohmic contacts for a moderately doped single crystal diamond (SND02)

The resulting Hall mobility for the non-Ohmic and Ohmic contacts shows comparable values, but notably more scatter in the data for the non-Ohmic contacts as seen in Fig. 3.14.

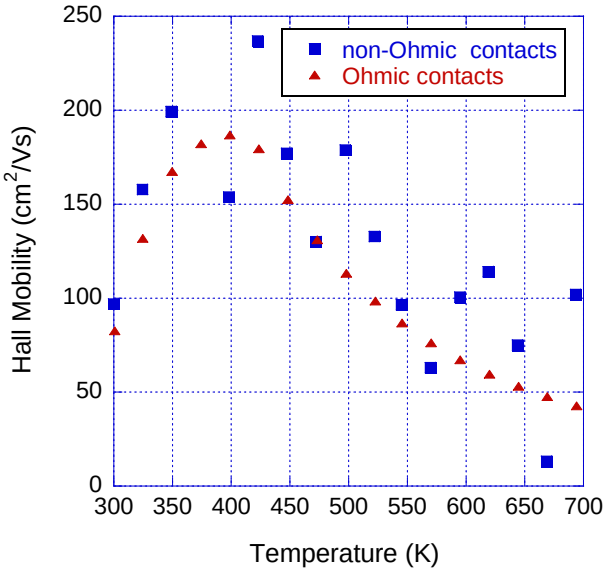

Figure 3.14 Hall mobility data comparison between Ohmic and non-Ohmic contacts for a moderately doped single crystal diamond sample (SND02)

IV measurements are performed for all samples in order to monitor the effects of annealing to the contacts. For a moderately boron doped single crystal diamond sample, IV curves showed annealing effects of the contacts as seen in Fig. 3.15. A considerable change in resistance and reduction in the non-linear behavior can be seen for the 300K curve measured after annealing (AA) compared with the 300K measurement before annealing to 700K. Non-linear behavior is observed for the lower temperature measurements at high voltages, however linearity is maintained as the IV measurements pass through the origin.

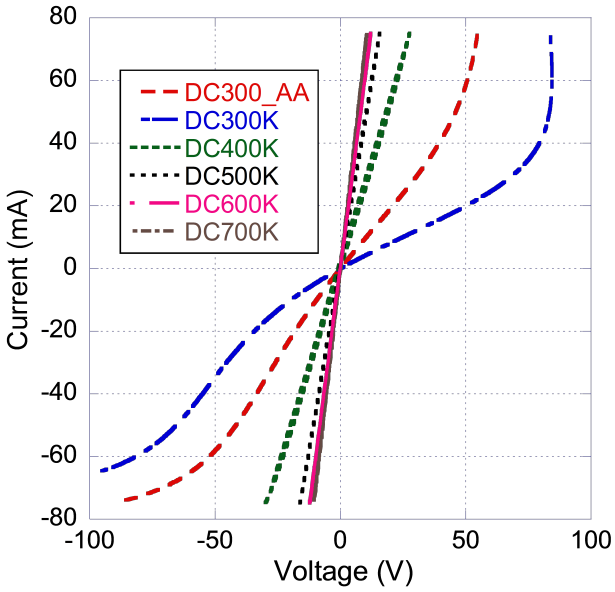

Figure 3.15 IV measurements for a moderately doped sample (SND02)

Followed by these contact studies, measurements of Hall effect according to ASTM standards were used to determine carrier concentration and mobility as seen in Fig. 3.16 and Fig. 3.17.

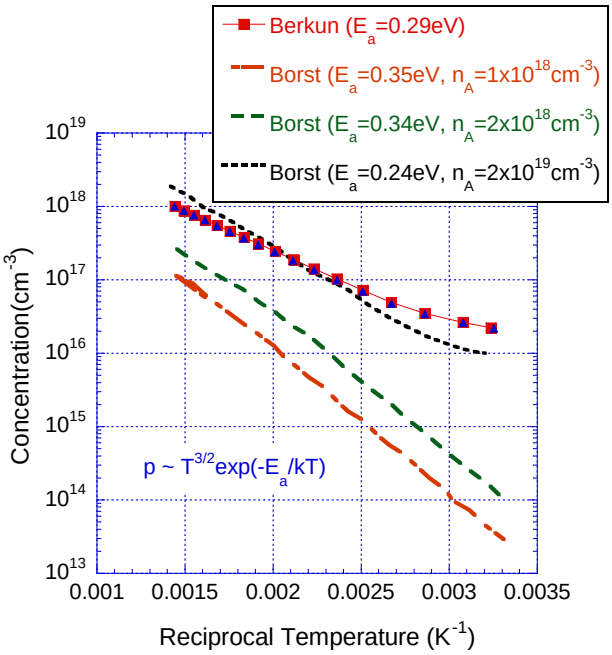

Figure 3.16 Temperature dependent concentration measurements for a moderately doped sample (SND02) with comparison to data reported by Borst, et al[9]

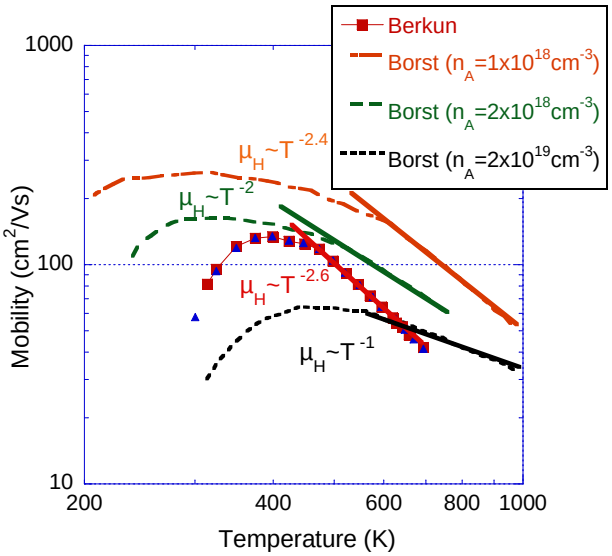

Figure 3.17 Temperature dependent mobility measurements for a moderately doped sample (SND02) with comparison to data reported by Borst, et al.[9]

The carrier concentration is observed to be in agreement with those reported by Borst and Weis [9], where literature data is extracted from the graphs reported and nA is the

fitted acceptor concentration. The resulting activation energy, obtained from the equation in Fig. 3.16, is slightly larger in the samples fabricated at MSU. The red (square) and blue (triangular) symbols indicate data points for measurements from 300K to 700K in red (square), and 300K to 700K in blue (triangular) which help to give the measure of repeatability.

The total mobility for semiconductor materials is commonly the sum of lattice-scattering mobility ($T^{-1.5}$) and the impurity scattering mobility ($T^{1.5}$). Mobility includes additional scattering mechanisms and is observed to be proportional to $T^{-2.6}$ for temperatures above $500K$ for the MSU diamond sample which is comparable to the $T^{-2.4}$ dependence reported by Borst and Weis [9] for similarly doped samples, however the mobility of these values are approximately 1.7 times larger than the mobility of the MSU sample at $400K$ due to higher acceptor concentration. Temperature dependence of the mobility is also comparable to the $T^{-2.8}$ value reported by Tsubota [31] for relatively smaller doping levels.

3.2.2 Effect of Applied Current to Hall Measurements

Non-linearities at higher voltages in the low temperature IV curves were the impetus for investigating the influence of current level on the temperature dependent measurements. The effect of applied current level for a moderately doped sample is investigated. Temperature dependent Hall effect measurements were taken between 300K and 700K using a measurement current of 30mA. This was then repeated at measurement currents of 50mA and 70mA. The resulting carrier concentration showed a systematic increase with increasing current at the lower temperatures, however significantly low dependence on the current is seen for temperatures above approximately 500K as seen in Fig. 3.18.

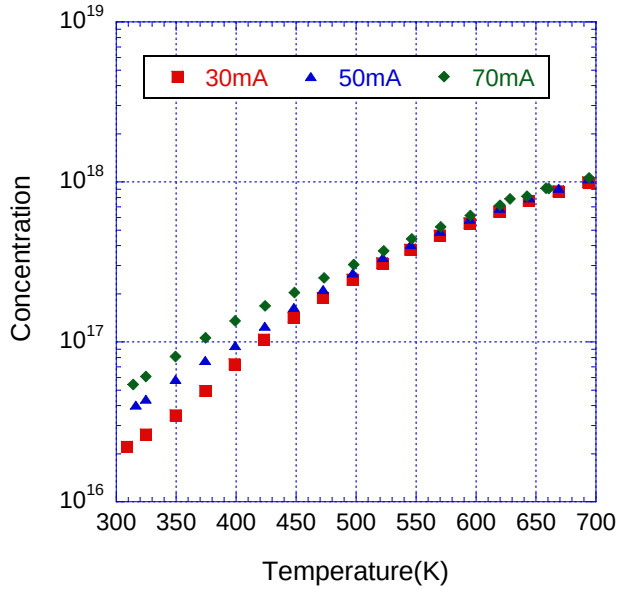

Figure 3.18 Effect of applied current level to concentration measurements for a moderately doped sample (SND02)

Similarly, as the current is increased a systematic decrease in mobility can be seen for the low temperatures in Fig. 3.19. It is not yet clear if this is related to the non-linear IV behavior seen at the higher current levels particularly evident in the low temperature IV curves and/or the possibility of self heating.

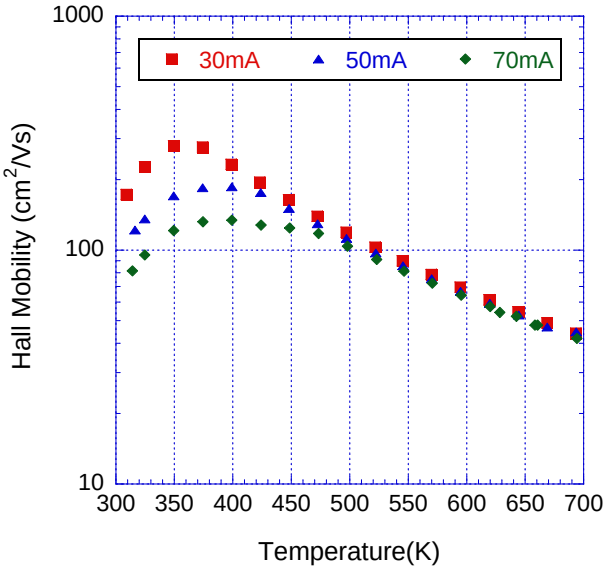

Figure 3.19 Effect of applied current to Hall mobility measurements for a moderately doped sample (SND02)

The differences are not seen in resistivity measurements for varying current levels as shown in Fig. 3.20. It is recognized that the measured Hall voltages are significantly smaller than the measured electrical resistivity voltages, thus if the error source is an offset error, this could have a stronger effect on the Hall measurements relative to the resistivity measurements. Further studies are needed to better understand such measurement dependencies.

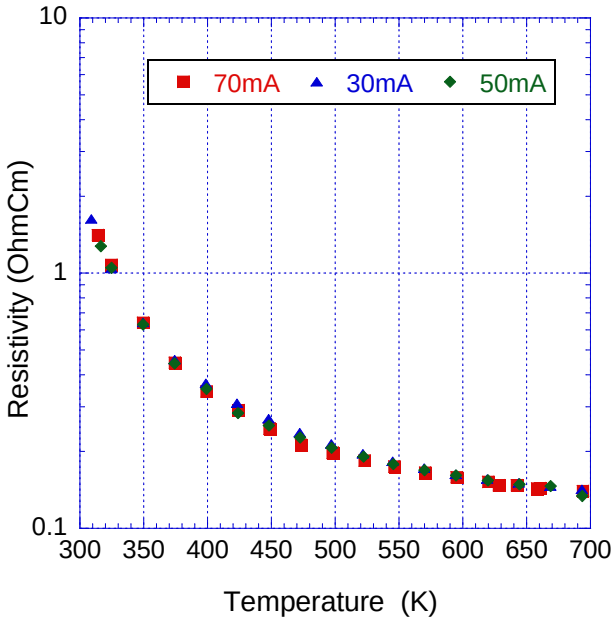

Figure 3.20 Effect of applied current to resistivity measurements for a moderately doped sample (SND02)

As a part of this work, resistivity, Hall and IV measurements of boron doped single crystal diamond films have been performed. Effects of system temperature stability, ohmic versus non-ohmic contacts, and measurement current amplitude have been studied.

3.3 Thermoelectric Materials

Through thermoelectric materials, heat can be directly converted to electricity using solid state energy conversion and heating/cooling can be achieved by applying a current through certain materials without any moving parts involved.

The efficiency of thermoelectric energy conversion depends on a materials properties, which could be evaluated by a dimensionless figure of merit, ZT:

$$ZT = \frac{S^2\sigma}{K}T \tag{3.1}$$

where S, σ and K are the Seebeck coefficient, electrical conductivity and thermal conductivity of the material. Generally $ZT = 1$ is the benchmark for good thermoelectric materials. In this work, $Mg_2(Si, Sn)$ compounds were synthesized using the molten salt sealing method and were powder processed, followed by pulsed electric sintering (PECS) densification by our group [2]. A set of $Mg_{2.08}Si_{0.4-X}Sn_{0.6}Sb_X (0 \leq X \leq 0.072)$ were characterized by temperature dependent hall effect system.

3.3.1 Carrier Concentration and Hall Mobility

The undoped sample (x=0) shows typical intrinsic behavior which is used to estimate the band gap, E_g, of the materials by fitting the temperature dependent carrier concentration n to Eq. 3.2,

$$n = 2 \times \frac{2\pi \times m^* k_B T}{h^2} \tag{3.2}$$

where m^* is the effective mass, k_B is the Boltzmann constant, T is the temperature in Kelvin, h is the Planck constant, E_C is the energy level of the bottom of the conduction band and E_F is the Fermi level. The assumption that the Fermi level of intrinsic semiconductors are in the middle of the bandgap was used and the temperature dependence of the band gap was neglected, a bandgap of $E_g = 0.594eV$ was obtained. The electric conductivity of the compound increases with increasing concentrations of Sb for $0 \leq x \leq 0.048$ as shown in Fig. 3.21. The Sb-doping is saturated when $x \geq 0.060$ and the carrier concentrations start to decrease as the doping level is further increased. Thus, electrical conductivities of the two most heavily doped samples (x=0.60 and x=0.072) are lower than that of x=0.048.

Hall mobilities of un-doped and moderately doped samples ($x \leq 0.036$) are shown in Fig.

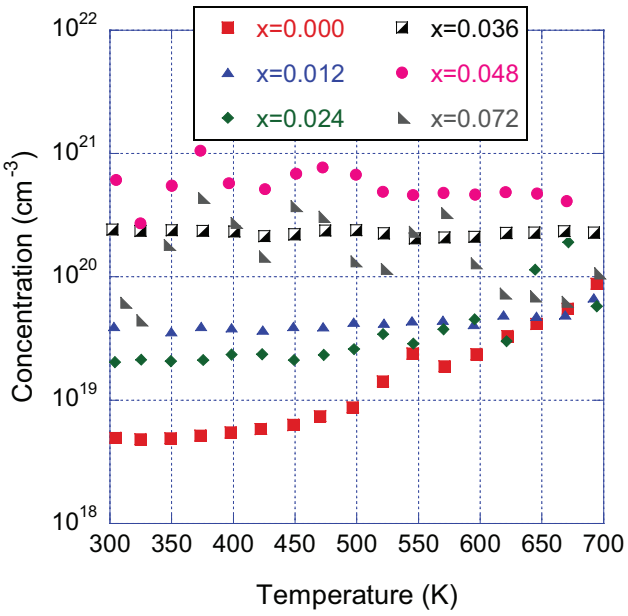

Figure 3.21 Carrier concentration versus temperature for nominal compositions of $Mg_{2.08}Si_{0.4-X}Sn_{0.6}Sb_X$

3.22. The temperature dependence of the Hall mobilities generally follows the relation of Eq. 3.3.

$$\mu_H \propto T^j \tag{3.3}$$

where j=-0.5 corresponds to alloy scattering and j=-1.5 indicates acoustic phonon scattering. Most of the Hall mobility indicates a mixed carrier scattering mechanism, j is in between -1.5 and -0.5. Measured hall mobility was fit to the empirical equation, Eq. 3.4 [65].

$$\frac{1}{\mu_H} = \frac{1}{\mu_{al}}(\frac{T}{300K})^{0.5} + \frac{1}{\mu_{ph}}(\frac{T}{300K})^{1.5} \tag{3.4}$$

where μ_{al} and μ_{ph} are the alloy disorder scattering mobility and acoustic phonon scattering mobility at room temperature, respectively. The alloy scattering can be related to the formation of the $Mg_2Si - Mg_2Sn$ solid solution. Disorder induced by Mg vacancies may

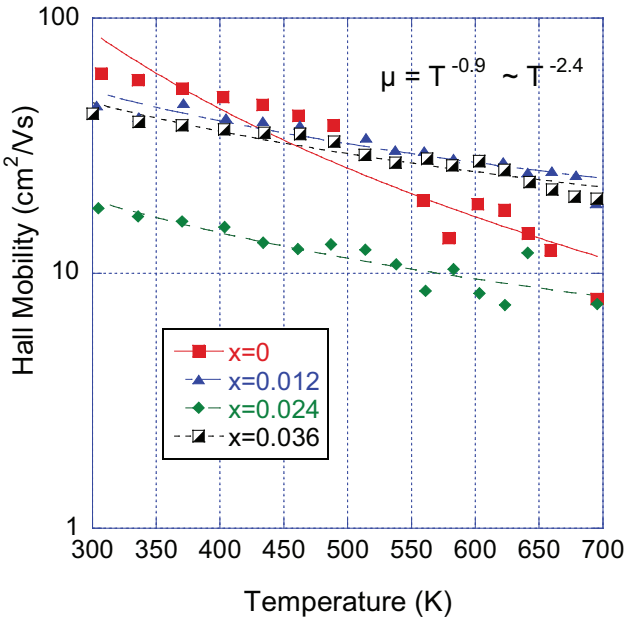

Figure 3.22 Hall mobilities for $Mg_{2.08}Si_{0.4-X}Sn_{0.6}Sb_X$

also be effecting the scattering. The value of μ_{al} decreases as the doping level increases, possibly indicating filling of the Mg vacancies. The values of μ_{ph} for the Sb-doped samples are higher than for the undoped sample, except for the x=0.024 specimen. This result is in agreement with the effect of Mg vacancies in Mg-deficient $Mg_2Si_{1-x}Sb_x$ materials reported by Dasgupta et al. [66].

For x=0.024, μ_{ph} value is lower due to internal cracks, which could also explains the lower electrical conductivity measured using ZEM-3 system and the Hall measurement system [2].

Chapter 4

Analysis and Discussion

4.1 Band Theory

Band hypothesis clarifies the purpose behind the contrasts between the properties of a decent insulator and of a metal. For a material in which the base of the conduction band is an energy E_g over the highest point of the valance band, a small number of electrons will be energized thermally into the unfilled band. The number will be relative to a Boltzmann factor $exp(-E_g/kT)$ so it shifts quickly with temperature. For insulators, energy needed to excite an electron from the valance band to the conduction band is larger than that of visible light and is in the order of $5 - 10eV$. At $300K$ temperature, $kT \simeq 1/40eV$. Consequently, at room temperature, the Boltzmann factor will allow a very small number of electrons to be energized. In any case it is expected to assume that if in some material, E_g was sufficiently small, then a considerable number of electrons could be energized at a moderate temperature. In that material, the variety of the Boltzmann factor with temperature would lead to an exponential variation of conductivity. At the point when this happens, electrons in the conduction band and holes in the valance band both adds to conduction, so called "intrinsic conduction" [10]

Sign of the Hall coefficient depends on the type of the doping which makes the semiconductor either p-type or n-type. Thus, all samples of germanium or diamond do not have the same sign Hall coefficient. These facts drove studies to calculate the effects of conduction

electrons in those samples [67].

The band diagram occasionally studied assumes that the crystal is a perfectly periodic structure containing no defects. In the case that now an additional atom is added inside the crystal, it will impact the periodicity which will be seen in the band structure. The quantity of levels in the conduction band will still be multiple of the number of atoms present (counting the additional one), yet while the levels got from the ordinary atoms will be grouped together and effect to the states of motion through the crystal. The levels associated with the additional atom can be displaced from the fundamental group levels and may fall into the energy gap between this band and the filled band. These levels represent a localized state centered on the extra space. Subsequently additional atoms result to a physical perturbation of the crystal and is reflected in the band diagram by relocation of some of the levels which may impact the appearance of levels in the gap between the full and empty bands as seen in Fig 4.1.

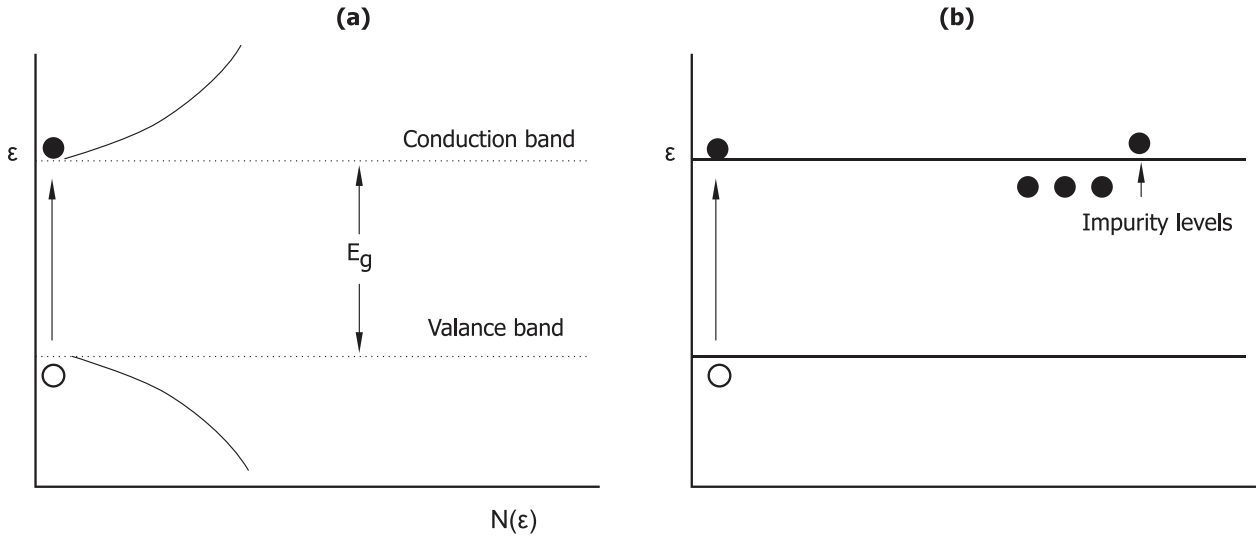

Figure 4.1 Intrinsic conduction. (a) Density of levels plotted for two separated bands separated by energy gap, ϵ_g. A hole in the valance band is formed when energy not less than ϵ_g is supplied to the system. The electron from the valance band is liberated in the conduction band. (b) Impurity levels supply electrons to the conduction band.[10]

An additional atom can be added in variety of ways. For instance, lead sulphide forms an ionic crystal of rock salt structure in which Pb^{2+} ions and S^{2-} ions alternate. Presume extra Pb atoms were added into the sample, there are two possibilities, either they might occupy an interstitial position or they might fill a typical Pb^{2+} site. If they fill a typical Pb^{2+} site, a vacant S^{2-} site ought to be created, in a way that adding a Pb atom would be same as extracting an S atom. In the final crystal, localized levels will be related with the Pb atom and the system will have two more electrons in addition to those required to ionize the entire sulphur atoms. In a defect free crystal, ideally there are just enough electrons to fill the valance band fully. The two additional electrons currently present will take up the localized levels associated with the additional lead atom, in the form of the lowest energy and remain with their parent atom. In case that these levels are located in the gap between the valance and conduction bands, then the energy needed to excite them into the conduction band will be smaller than the energy needed to excite electrons from the valance band. As a result this situation will supply mobile conduction electrons at a smaller temperature than the intrinsic mechanism [10].

In the case of impurities being dominant, the quantity of conduction electrons will vary with the concentration of impurity, therefore, different from the intrinsic mechanism, this mechanism can clarify the large difference in conductivity of different samples of the same type of material. Suppose an extra sulphur atom is added to lead sulphide, a similar behavior is expected to occur, but in this specific condition the sulphur center forms levels near the top of the valance band. Mentioned levels trap electrons and leave two holes in the band. Conduction in that case can be obtained and the Hall coefficient will have a positive sign. Another way of this behavior occurs when one extra sulphur atom is present and has tendency to capture two electrons from the lead atoms. If there is one extra S atom, it will be almost

impossible for them to get fully ionized. At absolute zero the un-ionized atom would be present close to the Pb^{2+} vacant site, however at higher temperatures, electrons can add to the conduction by differentiating their distribution on the S atoms [10].

4.2 Metal-Semiconductor Contacts

Followed by Wilson's formula of the transport theory of semiconductors based on the band theory of the solids in 1931 [68], as explained in Section 4.1, band theory was then applied to the metal-semiconductor contacts. In 1938, Schottky reported that, without the presence of a chemical layer, a potential barrier could be observed due to the stable space charges in the semiconductor [69]. "Schottky barrier" model is coming from this observation. In the same year, Mott came up with a more appropriate theoretical model, so called "Mott barrier" model [70]. Bethe et al. improved upon these models in 1942, so called "thermionic-emission" model. [71]. Further models on metal-semiconductor contacts can be found in References [72, 73, 74, 75].

Ohmic contacts are a critical since they could drastically enhance high temperature and the high power device capabilities, such as diamond diodes and are required in electrical transport characterization techniques, such as Hall effect. The high operating temperatures may convey challenge because of the diffusion processes in the contact layer and the reactions between the contact components. These reactions could prompt to changes of the contact properties during operation at high temperatures, and can either enhance or hinder the performance of the devices. If the contact resistivity is not low enough, a high voltage drop could emerge due to the high current density in the contact of the high power devices and leading to significant power loss and heating at the contacts. This high voltage drop is not

a desired phenomenon due to its divergence from the linear I-V behavior of the contacts, which also impacts Hall effect measurements.

As a result, the following properties are required in order to obtain high quality ohmic contacts [76]:

- *Work function match* - The work function of the contact metal, F_{metal}, needs to be close to the work function of the semiconductor, F_{semi} (thermal ionic). In some conditions, a thin layer of narrow bandgap material between metal and semiconductor is embedded. For low doped semiconductors, selectively highly doped regions can be created (tunneling assisted).

- *Low contact resistivity* - There is a small resistance associated with an ohmic contact between two materials. Contact resistivity, ρ_c, is proportional to the area of the contact, A as seen in Eq. 4.1.

$$\rho_c = R_c * A \tag{4.1}$$

- *High temperature stability* - This becomes a challenge for the wide band-gap semiconductors. In GaAs and Si devices, with melting temperatures of around 1238 °C and 1414 °C respectively, the maximum operating temperature is constrained by the metal contacts' stability and onset of intrinsic carriers. For materials which can perform at the higher temperatures, such as diamond, SiC and III-V nitrides, it is required to have thermally stable, reliable contacts which do not react with oxygen.

- *Reproducibility* - This criteria is essential in the case of the device production as well as Hall effect measurements. Therefore the contact fabrication process should provide

reproducibility as well as high quality. Contact materials and semiconductors need to have smooth morphology and clean surface.

The nature of the contact can be investigated further by considering the energy structure at the metal-semiconductor interface where an energy barrier can prompt to non-ohmic, Schottky, behavior and the lack of a potential barrier results in linear current versus voltage behavior, or an ohmic contact.

For the condition depicted in Fig. 4.2, the Fermi level in the semiconductor is closer to the vacuum level than the Fermi level in the metal. Thus, electrons will move from the semiconductor to the lower energy states in the metal. This will continue until the two Fermi levels align and the Fermi level in the semiconductor is reduced by an amount which is identical to the difference between the two work functions.

The work function, $q\phi_m$ (for metal) and $q(\chi + \phi_n)$ (for semiconductor), is nothing but the energy difference between the vacuum level and the Fermi level. $q\chi$ is the electron affinity measured from the bottom of the conduction band E_c to the vacuum level, and $q\phi_n$ is the energy difference between the E_c and the fermi level, E_F. The contact potential, $\phi_m - (\chi + \phi_n)$, is defined as the difference between the work function of the metal and the semiconductor. As the gap distance, δ, becomes smaller, electric field in the gap region increases. As a result of this increased electric field, negative charge is built up at the metal surface. In order to satisfy equilibrium, an equal amount of opposite (in this case positive) charges must exist in the semiconductor depletion region. There is similarity here with the n-type side of a p+ - n junction. When the metal and semiconductor come in contact, the energy band diagram of the junction is found as shown in Fig. 4.2d. The limiting value of the barrier height, $q\phi_{Bn0}$, is given by the difference between the work function and the

electron affinity of the semiconductor in Eq. 4.2.

$$q\phi_{Bn0} = q(\phi_m - \chi) \tag{4.2}$$

If a p-type semiconductor is used instead of the n-type semiconductor, then the barrier height, $q\phi_{Bp0}$, is given in Eq. 4.3.

$$q\phi_{Bp0} = E_g - q(\phi_m - \chi) \tag{4.3}$$

For any given metal-semiconductor pair, the sum of the barrier heights for n and p-type semiconductor is accepted to be equal to the bandgap as in Eq. 4.4.

$$q(\phi_{Bp0} + phi_{Bn0}) = E_g \tag{4.4}$$

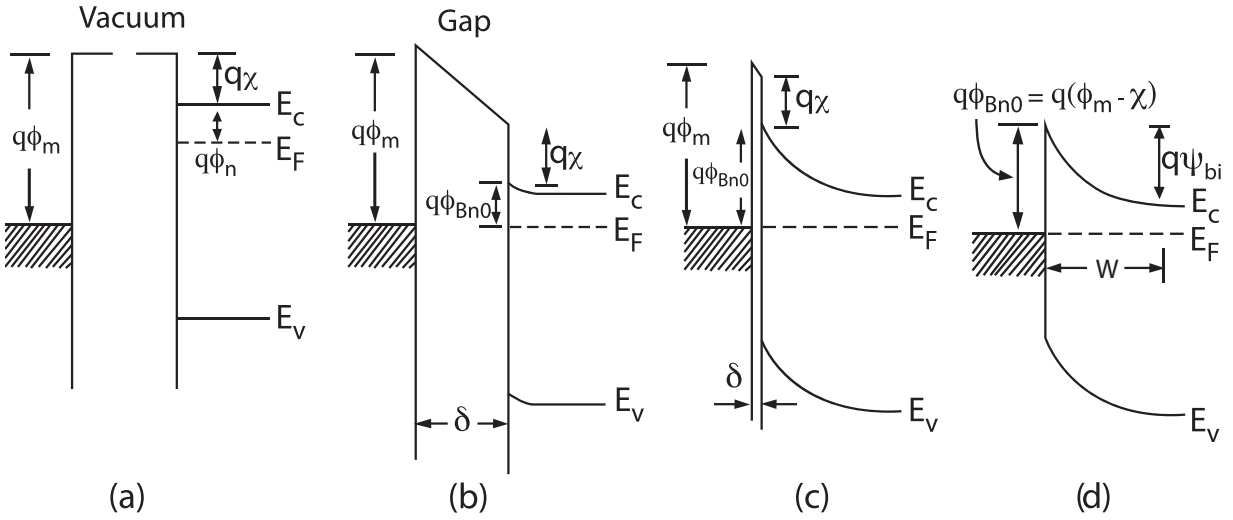

Figure 4.2 Energy band diagrams of metal-semiconductor contacts. Metal and semiconductor (a) in separated systems, and (b) connected into one system. As the gap δ (c) is reduced and (d) becomes zero. [11].

Eq. 4.2 and 4.3 are theoretically ideal however, experimentally it is very challenging,

almost impossible to achieve. The main reasons causing this deviations of experimental barrier heights from ideal are:

- An unavoidable interface layer, $\delta \neq 0$, as shown in Fig. 4.2c.
- The presence of interface states

In order to achieve the desired metal to semiconductor contacts, consideration of the metal work functions and semiconductor electron affinities provide an initial guide. Typically for metals, $q\phi_m$ is of the order of a few electron volts $(2 - 6eV)$, which is very sensitive to surface contamination. Some commonly used metal contacts in this thesis are Ag, Al, Ti and Au with $q\phi_m$ values of $4.26 - 4.73eV$, $4.06 - 4.26eV$, $4.33eV$ and $5.1 - 5.47eV$ respectively. Values are given as a range since the numbers may differ depending on the crystal face. The electron affinity of diamond (χ) and work function (ϕ) for different doping levels and different crystal orientation is given in Fig. 4.3.

Ohmic and Schottky contacts are the two types of metal-semiconductor contacts. A Schottky barrier is established in the Schottky metal-semiconductor contacts. The ohmic contacts are another type of metal-semiconductor contacts, which have linear and symmetrical I-V characteristic. Ohmic contacts have a relatively small contact resistance. I-V characteristics, such as the linearity around the origin, are used to determine the presence of ohmic properties. A high quality ohmic contact should not hinder the performance of the device which can also supply the current with a relatively small voltage drop. In order the characterize an ohmic contact, specific contact resistance, so called contact resistivity, is being used. Contact resistivity is defined as one over the derivative of the current density with respect to the voltage across the interface, as shown in Eq. 4.5 [76].

(a) Low-B-doped (100) surface

T (°C)	H-plasma	400	600	1100
χ (eC)	-1.0	-0.8	0.3	1.3
ϕ (eV)	3.9	3.9	4.9	5.3

(b) Low-B-doped (111) surface

T (°C)	H-plasma	400	600	1100
χ (eVI)	-0.9	-0.5	0.3	1.5
ϕ (eV)	4.2	4.4	4.9	5.6

(c) High B-doped (100) surface

T (°C)	H-plasma	400	600	1100
χ (eV)	-1.1	-0.6	-0.5	1.8
ϕ (eV)	3.7	4.2	4.3	5.7

(d) High N-doped (100) surface

T (°C)	H-plasma	400	600	1100
χ (eV)	/	-0.2	-0.3	0.7
ϕ (eV)	/	3.1	3.3	4.7

Figure 4.3 Electron affinity of diamond (χ) and work function (ϕ) for different doping and orientation [12]

$$\rho_c = \frac{\partial J}{\partial V}^{-1}_{V=0} \tag{4.5}$$

Thus, the contact resistivity can be determined from the I-V characteristics of the junction and the area of the contact [77]. When forward biased, there are four main contributions to current transport across the metal semiconductor contact: 1) Emission of electrons from the semiconductor into the metal over the top of the barrier (thermionic emission). 2) Quantum-mechanical tunnelling through the barrier (field emission). 3) Recombination in the space-charge region. 4) Hole injection from the metal into the semiconductor [13]. Comparing the doping, E_{00}, to temperature, kT, decision of the current transport mechanism through the contact is realized. These mechanisms mainly include thermionic emission

(TE), thermionic field emission (TFE) or field emission (FE). At a low or moderate semiconductor doping level and/or moderately high temperatures, $kT \gg E_{00}$, standard thermionic emission mechanism dominates with the contact resistivity exponentially dependent on the barrier height as shown in Eq. 4.6.

$$\rho_c = \frac{k}{A**Tq} exp(\frac{q\phi_{Bn}}{kT}) \propto exp(\frac{q\phi_{Bn}}{kT}) \tag{4.6}$$

Since applied voltage is small, the voltage dependence of the barrier height can be neglected. In order to obtain small contact resistance, ρ_c, small barrier height, ϕ_{Bn}, is required.

In the case of higher doping levels, $kT \approx E_{00}$, the depletion layer width lowers; the barrier becomes smaller and a part of electrons tunnel through it. In this case, current transport is dominated by the thermionic field emission mechanism through the barrier only as shown in Eq. 4.7.

$$\begin{aligned} \rho_c = \frac{k\sqrt{E_{00}} cosh(E_{00}/kT) coth(E_{00}/kT)}{A**Tq\sqrt{\pi q(\phi_{Bn} - \phi_n)}} exp[\frac{q(\phi_{Bn} - \phi_n)}{E_{00} coth(E_{00}/kT)} + \frac{q\phi_n}{kT}] \\ \propto exp[\frac{q\phi_{Bn}}{E_{00} coth(E_{00}/kT)}] \end{aligned} \tag{4.7}$$

where ϕ_n is negative for degenerate semiconductors. The factor kT/E_{00} (where k is the Boltzmanns constant, and T is the absolute temperature) is the criteria for the relation between thermionic and field emission processes. The characteristic energy E_{00} is related with the tunnelling probability and, as a result of the decrease of the depletion layer width, increases with the semiconductor doping level. The thermionic emission occurs at $kT/E_{00} >> 1$. When $kT/E_{00} = 1$ these two processes can be comparable and the current transport mechanism is named as thermionic-field emission. The field emission is predominating at $kT/E_{00} << 1$ as shown in Eq. 4.8 [78].

$$\rho_c = \frac{ksin(\pi c_1 kT)}{A**Tq} exp(\frac{q\phi_{Bn}}{E_{00}}) \propto exp(\frac{q\phi_{Bn}}{E_{00}}) \tag{4.8}$$

In order to achieve low contact resistivity, low barrier height should be used [77]. Low barrier height is very challenging to achieve, a high quality ohmic contact is required to operate in the tunneling regime.

Contact resistivity is a function of barrier height in all regimes, doping concentration (in TFE and FE), and temperature (more sensitive in TE and TFE) as shown in Fig. 4.4. In TE regime, ρ_c is independent of doping concentration and dependent only on the barrier height, ϕ_B. In FE regime however,ρ_c is dependent on $\propto exp(N^{-0.5})$ in addition to ϕ_B.

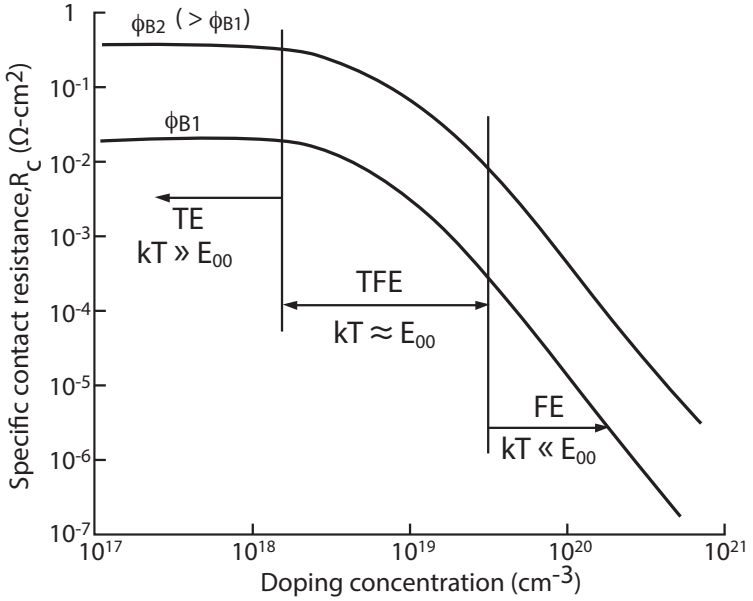

Figure 4.4 Dependence of specific contact resistanceon doping concentration (and E_{00}), barrier height, and temperature. TE, TFE and FE are indicated [11]

As the contact resistivity, ρ_c, is the most critical factor to quantify the quality of the ohmic contacts, various methods for contact resistivity measurement have been used: two probes method, four probes method, extrapolation method, differential method, method of the interface probes and Transmission line model method (TLM) [13]. The commonly used

method is the TLM method due to relatively low measurement error with I-V characteristic linearity determination. TLM method includes two structures, linear [79] and circular [80]. The linear TLM method needs formation of mesa structures. Circular TLM method does not require mesa structures; however it is practical for very small sheet resistance of the metals. The values of the contact resistivity shown here are determined using a linear TLM method as seen in Fig. 4.6.

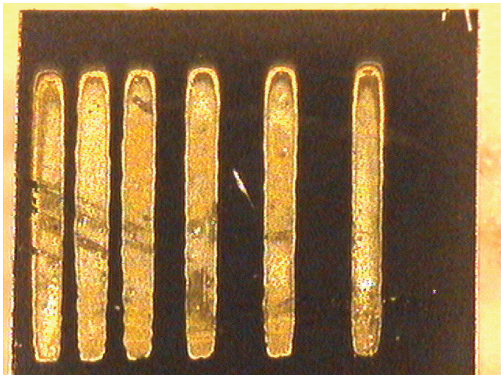

Figure 4.5 Sample image for transmission line measurements (TLM).

The contact resistance and resistivity for Ti/Au contacts after annealing were calculated as $R_c = 0.13957\Omega$ and $\rho_c = 3.07 * 10^{-4}\Omega cm^2$ respectively. The order of magnitude for the specific contact resistance in literature were in the order of $\rho_c = 10^{-4}\Omega cm^2$ [81].

Two main techniques can be used to achieve ohmic contacts: by increasing the semiconductor doping level and/or by decreasing the barrier height as seen in Fig. 4.7.

It is challenging to achieve low resistivity ohmic contacts to p-type wide band-gap semiconductors due to the high electron affinity and large width of the band-gap. For example, the electron affinity of SiC and GaN is $3.3eV$ and $1.84eV$, respectively. For the commonly used SiC materials, the band-gap width is in the range of $2.3 - 3.2eV$, while for GaN it is $3.44eV$ for wurtzite polytype and $3.2eV$ of the zinc-blended structure. This results a high Schottky barrier which is formed at the interface metal/p-type (SiC, GaN).

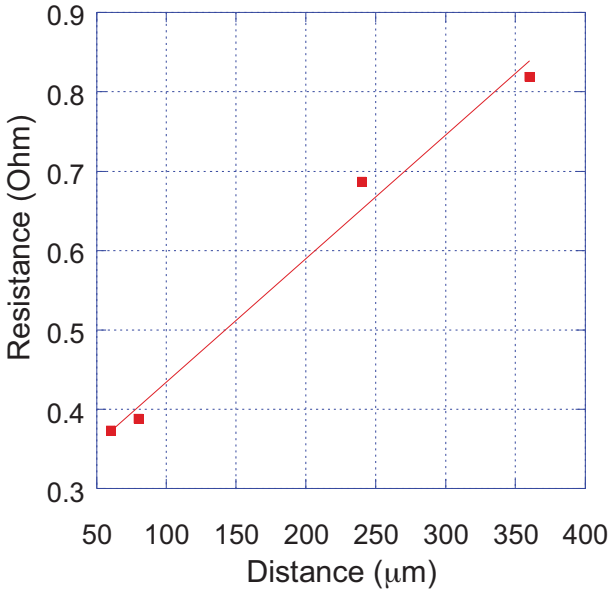

Figure 4.6 Transmission line measurements (TLM).

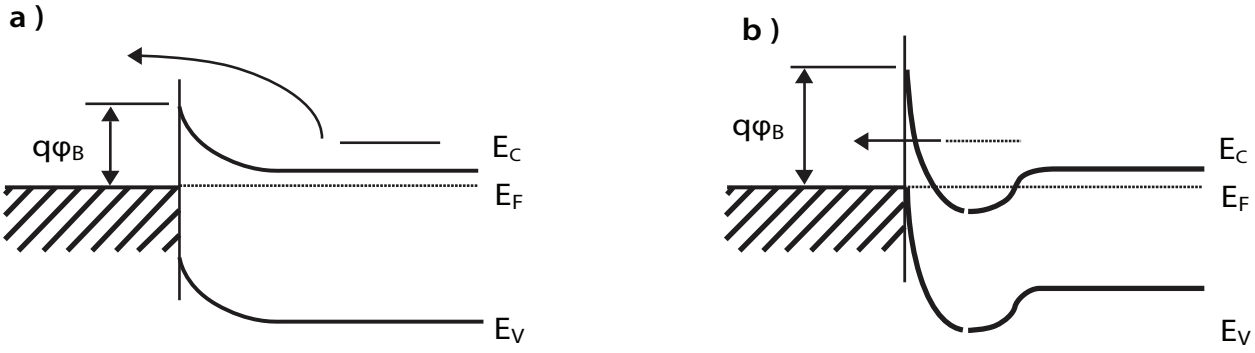

Figure 4.7 A zone diagram of an ohmic contact with a) low barrier height and b) high doping level [13].

A metal with a work function which is enough to yield a low barrier at the interface for a low doped diamond sample does not generally exist. Techniques for making ohmic contacts for such samples involves shallow diffusion, alloy regrowth, in-diffusion of a dopant contained in the contact material. Selective doping process for a lightly boron doped single crystal diamond sample, LB04 has been carried through as shown in Fig. 4.8.

LB04 started with a $\sim 7.5\mu m$ thick low boron doped film. Then a $\sim 0.6\mu m$ thick highly boron film was deposited on top of the low boron doped film. Etching process was performed

with a $\sim 1.2\mu m$ thick Al hard mask applied through a tape mask. Using Reactive Ion Etch (RIE), $\sim 1.6\mu m$ is etched into the sample as seen in Fig. 4.8. The low boron doped film has shown a carrier concentration of $\sim 1.3 * 10^{17} cm^{-3}$ from FTIR estimation.

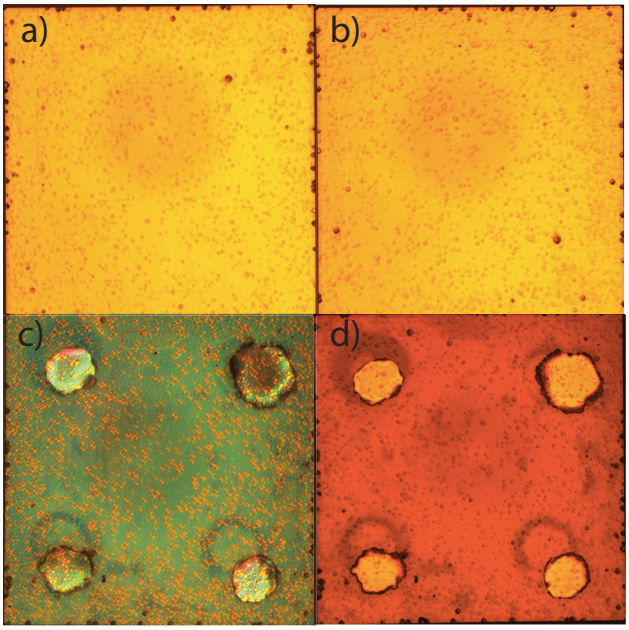

Figure 4.8 Low boron doped diamond (LB04) selective doping process steps. a)Low boron doped surface b)High boron doped surface c) Surface with Al mask before etching d) Surface with Al mask after etching.

Most commonly used process for obtaining low resistivity contacts involves annealing. Followed by the metal deposition, annealing process involves heating at the eutectic temperature for an optimal time either under vacuum environment or in an ambient of an inert gas. Annealing results metal to be alloyed into the semiconductor lowering the barrier height at the interface. Ohmic contacts can be obtained without annealing with molecular-beam epitaxy (MBE), metal-organic chemical vapour deposition (MOCVD) epitaxy and ion implantation by obtaining high doping level ($10^{20} cm^{-3}$) of the epitaxial layers during the growth.

For this work, annealing process has been performed followed by metal contact fabrication. Properly aligned shadow mask has been positioned over the selectively doped p+

layers as seen in Fig. 4.9. Ti/Au ($30nm$ and $300nm$ thick respectively) contacts have been deposited by sputtering under the argon gas with a starting pressure of $2 * 10^{-5} Torr$.

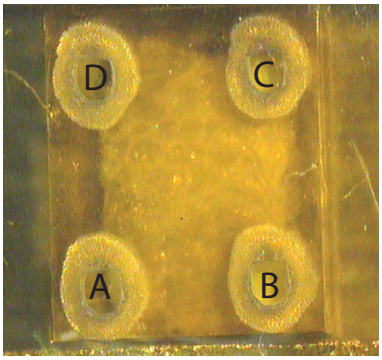

Figure 4.9 Shadow mask alignment prior to Ti/Au deposition on boron doped diamond sample (LB04)

Followed by metal contact fabrication annealing has been performed in the Hall effect measurement system while monitoring the I-V behavior of the contacts at various temperatures for LB04. Due to selective doping, even at room temperature with no anneal, ohmic nature of the contacts around the origin can be observed as seen in Fig. 4.10. IV behaviors for six different contact pairs at various temperature regimes have been measured and uniformity has been observed between different contact pairs. After annealing, IV behavior at room temperature has been observed to remain ohmic. Thus, resistivity and Hall effect measurement have been performed on this sample.

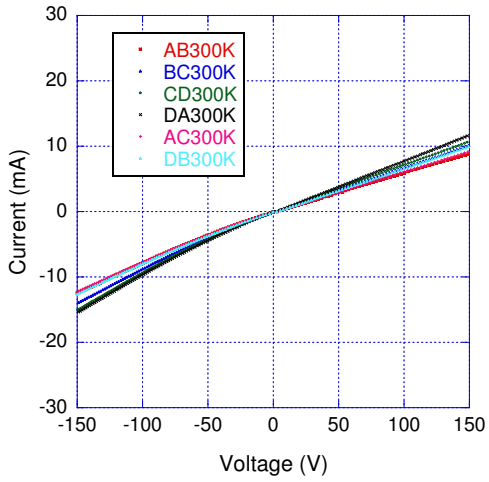

(a) T=300K

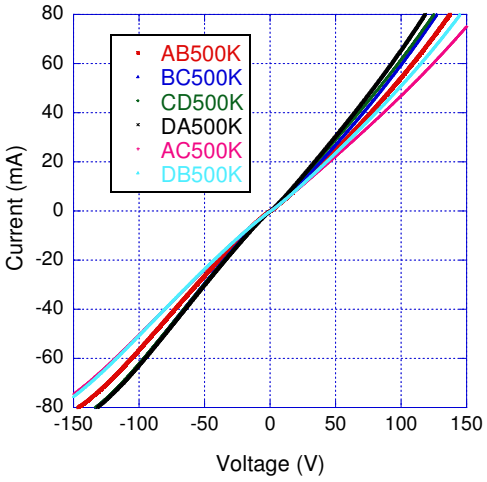

(b) T=500K

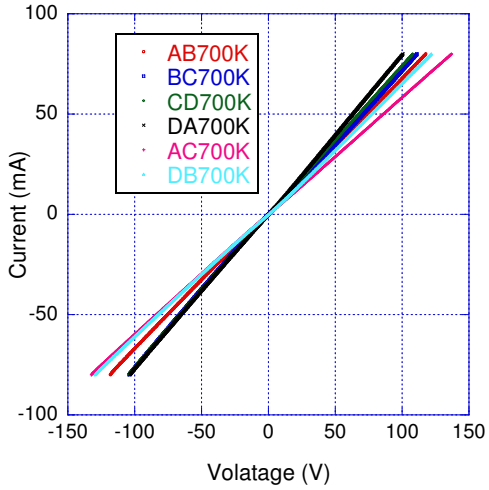

(c) T=700K

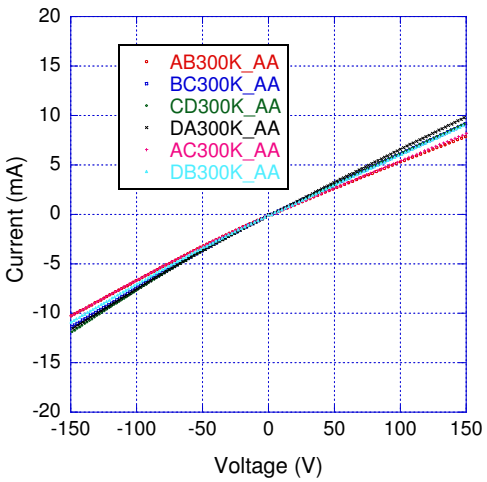

(d) T=300K (AA*=after anneal)

Figure 4.10 IV curves at various temperatures (300K to 700K) for boron doped diamond sample (LB04).

4.3 Characterization of Silicon and Germanium

Silicon played an important role in the development of microwave radar during World War II. This resulted to an in-depth study of silicon and of germanium where the impurity content during the fabrication of the material could be precisely controlled. Intrinsic and

impurity conduction was studied from quantification of the variation of the Hall coefficient and conductivity with temperature. Thus Fig. 4.11 and 4.12 shows the results of some of the early experiments on germanium. In these figures, the logs of R and ρ are plotted against $1/T$. During the estimation of n where Boltzman term is $exp(\epsilon/kT)$, plot yields a straight line. Slope of this line gives the activation energy, E_a and E_d, for acceptors and donors respectively. At low temperatures, the conductivity and Hall coefficient of different samples may vary from one another by a factor of almost 10^4 however at high temperatures, the measurements for all samples have a tendency to be on the same straight line. The line found at high temperatures demonstrates the intrinsic region. From the slope on the intrinsic line the energy gap, E_g between the conduction and the valance band was calculated to be about $0.74eV$ [10].

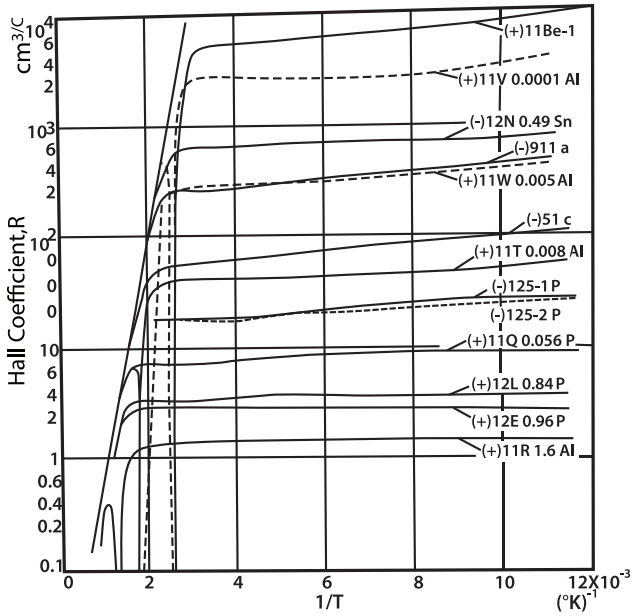

Figure 4.11 Hall coefficient data for Ge [10]

Amount of impurities added to a sample effects the point at which the curve for a given specimen leaves the intrinsic line. With decreasing temperature, the concentration of intrinsic carriers fall down. At the point where the intrinsic carrier concentration is less than the

concentration of the impurities, the behavior will be dominated by the impurities.

Fig. 4.11 shows that on leaving the intrinsic line the Hall coefficient initially appears to be independent of temperature, but at still lower temperatures the Hall coefficient starts to rise slowly, suggesting that the carrier concentration is decreasing. This is related to the energy required to excite carriers from the impurity levels being very small (about $0.2eV$). Considering the room temperature is equivalent to about $0.025eV$, at room temperature all the impurity carriers are expected to be excited. In order to observe the impurity activation energy, much lower temperatures are needed. A different behavior can be seen in the plot of resistivity, on leaving the intrinsic range the resistivity initially decreases as the temperature is lowered. Resistivity then passes through a minimum and then starts to increase moderately as the temperature decreases. This seems fairly conflicting but can be explained by the relationship between the concentration of carriers and their mobility. At temperatures just below the intrinsic range, the carrier concentration is constant, as a result, the variation of resistivity will be determined by that mobility. It is known that, as the temperature decreases, mobility increases. At moderate temperatures, scattering of electrons by lattice vibrations have a dominant effect on the mobility. Significant results can be obtained by taking a closer look to the the amplitude of these vibrations which should fall as the temperature lowers, as a result the mobility should rise and accordingly the resistivity should decrease. In the intrinsic range, the mobility still falls as the temperature rises, but its impact to the conductivity is dominated by the considerably fast variation of the exponential component.

At the lower temperatures, Hall coefficient starts to increase again, which shows that the free carriers are falling into the impurity levels. The resistivity is also seen to rise at lower temperatures due to several factors including the reduction in the carrier concentration as well as the effects of the mobility. At the lowest temperatures, Hall coefficient does not

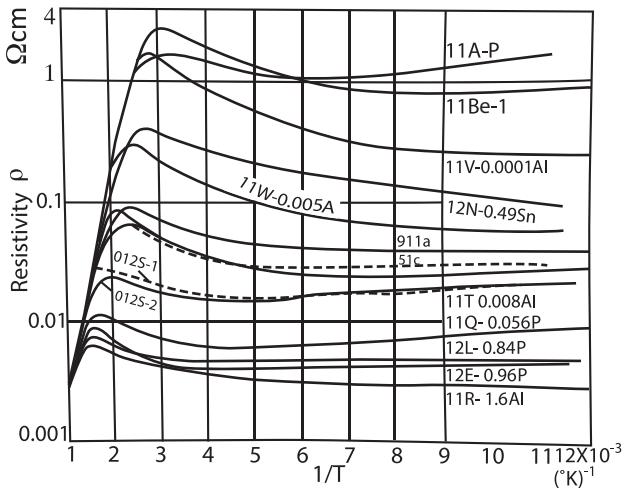

Figure 4.12 Resistivity data for Ge [10]

continue to increase, but either approaches to a constant value, or, often falls down. The reason of this behavior is impurities and imperfections in the sample are dominating over the lattice vibrations. In the past years, materials had more defects and more imperfection than current materials, so it shows the presence of impurity scattering very clearly. As a result, it is observed that at the lowest temperatures the resistivity increases more rapidly than the Hall coefficient.

Common impurities for germanium include but not limited to boron, aluminum and phosphorus. Germanium has four electrons in the outermost shell and is a member of group IV of the periodic table. These four electrons fill the valance band. Phosphorus belongs to Group V, and has five outer electrons, while aluminum and boron belongs to Group III, with three outer electrons. One impurity electron is available for each phosphorus atom which makes the sample n-type. In aluminum and boron doping case, a hole could be created by every impurity atom which makes the sample p-type. Since a phosphorus atom has one unit of positive charge and one additional electron on its nucleus more than the germanium atom, a sole phosphorus atom in a germanium crystal is equivalent to a single hydrogen atom

embedded in a medium with the dielectric constant of germanium. Using the Bohr theory of the atom, energy required to ionize this hydrogen atom can be calculated which is around $0.02eV$, this is equivalent to the energy required to take the electron from the phosphorus atom and place it in the conduction band. The ionization energy of the hydrogen atom model is found by dividing the Rydberg energy by the square of the dielectric constant which is around $0.04eV$, for germanium. For impurities like aluminum, by considering them as inverted hydrogen atoms with a negative nuclear charge and planetary positive hole, this model can also hold. Ionization energy will be the identical to the energy calculated for an electron [10].

In order to investigate and test the Hall effect system, germanium and gallium arsenide samples have been measured and tested as seen in 4.3.1 and the following sections.

4.3.1 p-Type Ge

p-Type Ge sample purchased from WRS materials is measured in Van der Pauw (VdP) configuration. Ohmic contacts observed without any metal deposition. Silver paste used to connect $50\mu m$ gold wires to the sample. Sample thickness is $0.037cm$, $40mA$ is used as applied current, 10 readings has been taken to average. Conductivity and Hall effect have been measured from $300K$ to $700K$ with $25K$ steps. To show repeatability, measurement is also performed cooling back down from $700K$ to $300K$.

Optimization results quantified four parameters for p-Ge as $N_A = 6.615 * 10^{17} cm^{-3}$, $E_a = 0.0115eV$, $N_D = 1 * 10^{16} cm^{-3}$ and $E_d = 1.379eV$ as seen in Fig. 4.13 which is comparable with the carrier concentration of acceptors as provided by WRS materials. Future studies, possibly measurements with varied magnetic field with the QMSA technique, are needed to further investigate the donor concentration and activation energy for this sample.

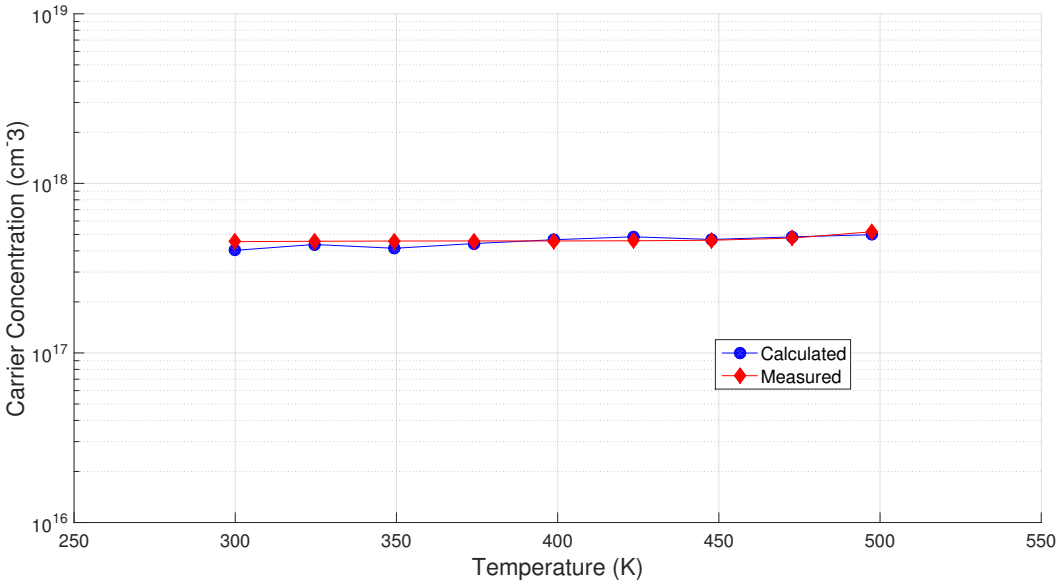

Figure 4.13 Concentration vs temperature fit for p-type germanium

In order to study the mixed carrier conduction mechanism for p-type germanium, concentration dependence of the electron and hole mobilities have been taken into account in Eq. 4.9 and results are shown in Fig. 4.14.

$$\sigma = \mu_n + \mu_p \tag{4.9}$$

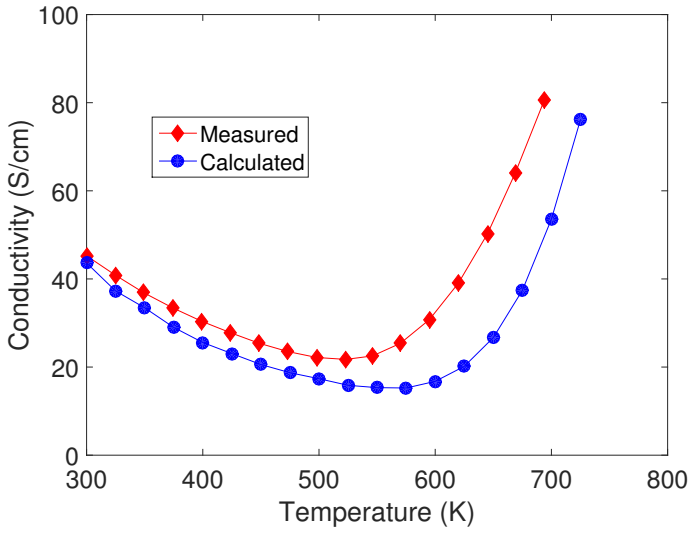

Figure 4.14 Conductivity vs temperature fit for p-type germanium

Both measurement and physical analysis results show a transition from extrinsic to intrinsic conduction at a temperature range of approximately around $550K$.

4.4 Characterization of Diamond Materials

Boron is one of the most common acceptor impurity for diamond where $E_i = 0.37eV$. In boron doped diamond samples, transition from a semiconductor to a metal and ultimately to a superconductor can be observed as the boron doping level increases above $5x10^{20}cm^3$.

In this thesis, the Hall mobility of single crystalline and polycrystalline boron doped diamond is investigated in a large temperature range $(300K - 700K)$and large doping range for samples grown by different groups at Michigan State University. Literature studies show that for low boron-doping level, the low- temperature mobility is controlled by ionized impurity scattering primarily because of the compensation and the high- temperature mobility by phonon scattering (acoustical or optical with an intraband or interband process) [28].

For heavily boron doped diamond samples, the low-temperature mobility is extensively constrained by the neutral impurity scattering (neutral boron atoms), as a result, the maximum room-temperature mobility is dependent of the doping level.

Boron doped single crystal diamond samples and the effects of substrate temperature and growth rate on the doping efficiency for diamond samples, SND25, SND26, SND33 and SND34 are reported by Demlow et al. [14]. Hall effect and resistivity has been studied and shown in this thesis.

Ohmic contact fabrication is necessary to obtain high quality Hall effect and resistivity measurements. An acid cleaning step is used prior to physical vapor deposition of metal contacts consisting of Ti(30nm)/Au(150nm) on the four corners of the sample in a Van der Pauw configuration.

IV measurements are taken between $300K$ and $700K$ for 6 different contact pairs. Linear IV curves are measured as seen in Figure 1 and the effect of annealing is shown in Fig. 4.15.

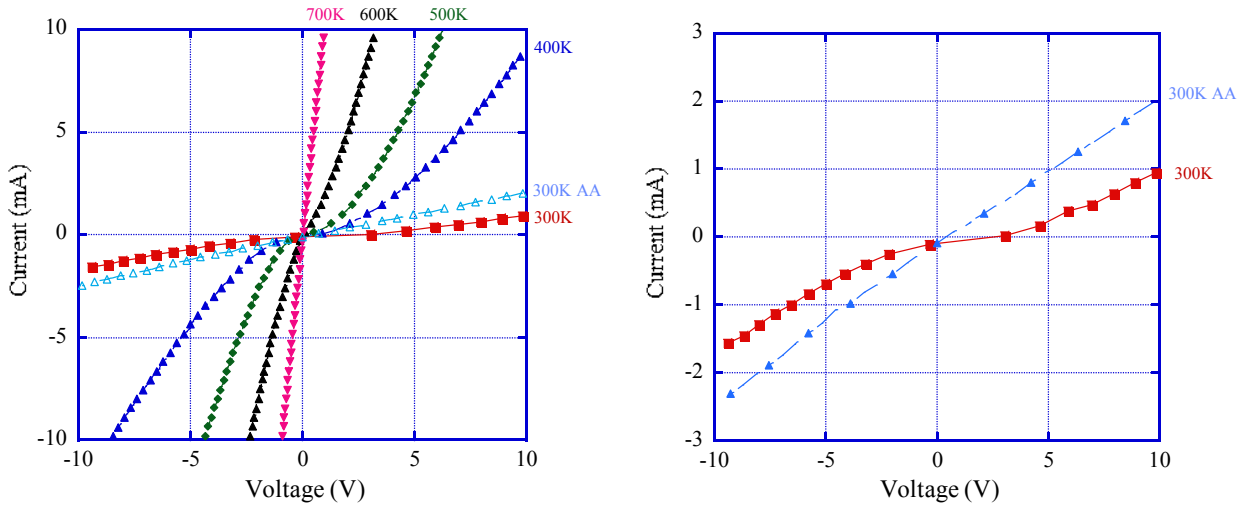

(a)IV curve (b)Effect of annealing (SND26)

Figure 4.15 Temperature dependent IV curves for SND26. (a)Temperature range of 300K-700K (b)Effect of annealing at 300K.

Followed by achieving permanent ohmic contacts, resistivity and Hall effect measurements are performed.

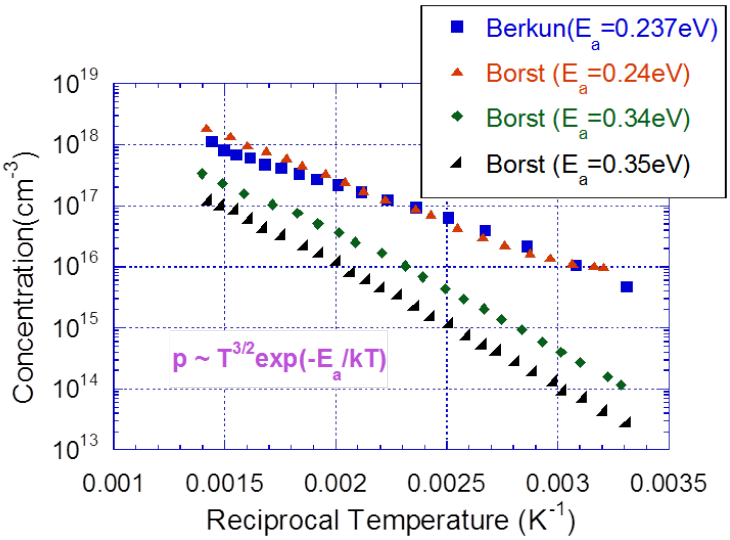

Figure 4.16 Concentration vs temperature fit for SND26

Temperature dependent concentration compared with the literature is shown in Fig. 4.16. Concentration measurements show a good agreement with the similarly doped single crystal samples in the literature [4]. The remaining samples with relatively higher activation energy (Ea) belongs to the low doped samples.

According to Barjon et al. [82], activation energies are different for high and low temperature regimes, which commonly shows a ratio of 2. For SND26 diamond sample, using a similar activation energy calculation approach, a ratio of 1.9 with activation energies of $0.130eV$ for high temperature region and $0.248eV$ for low temperature region is observed as shown in Fig. 4.17.

The comparison of single carrier model and mixed carrier model has been studied and shown in Fig. 4.18. Hall effect measurements show a reliable repeatability between the measurements of heating up ($300K$ to $700K$) and cooling down ($700K$ to $300K$) as indicated in red squares and blue triangles respectively. The fitting with a boron concentration of

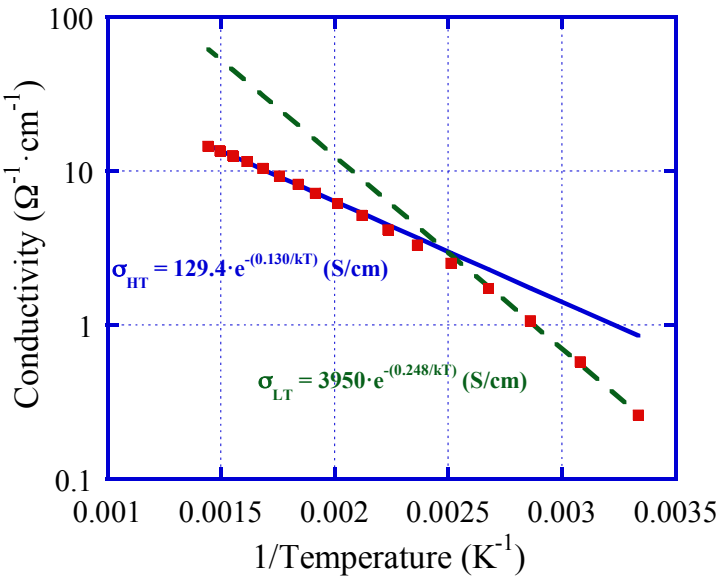

Figure 4.17 Activation energy for SND26

$6x10^{18}cm^{-3}$ where activation energy is $0.254eV$ with a concentration of compensating impurities of $3x10^{17}cm^{-3}$ where activation energy is $1.7eV$ for nitrogen. Single carrier model, indicated with a dashed line, deviates from the experimental results whereas mixed carrier model, indicated with a straight line, agrees well as shown with a straight line.

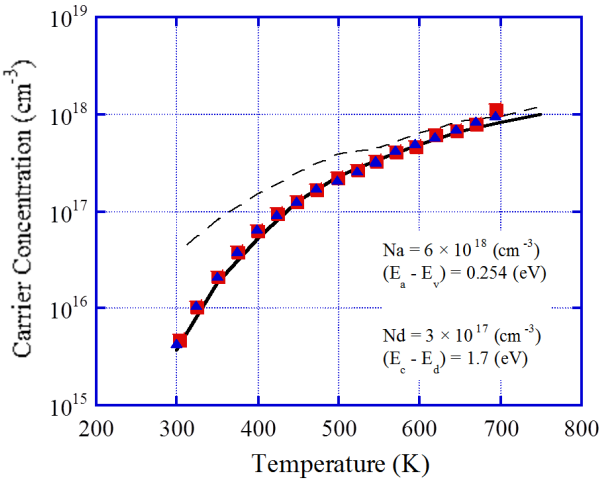

Figure 4.18 Fitting vs experimental results using single carrier (dashed line) and mixed carrier (straight line) model for SND26

Assuming the concentration of the compensating donors is zero, the simulation results of

varied carrier concentration with the activation energy of $0.25eV$ is shown in Fig. 4.19.

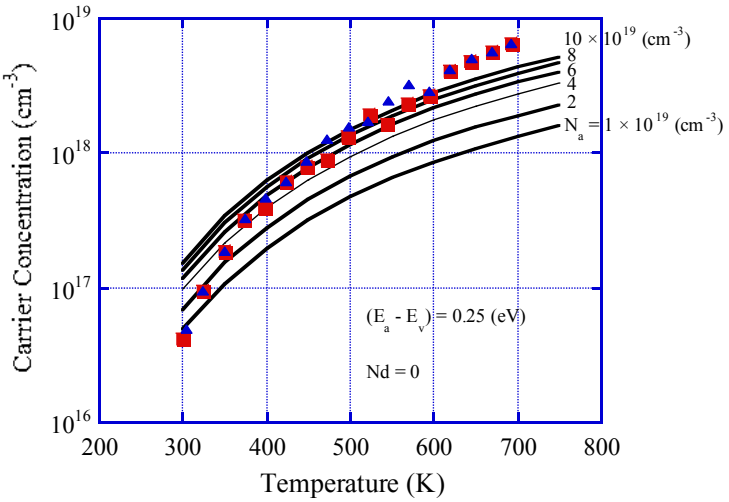

Figure 4.19 Fitting with varied Na for SND26

Simulation results suggest the presence of the compensating impurities in the sample. Activation energy has a big impact to the carrier concentration as seen in Fig. 4.20 where the activation energy is ranging between $0.10eV$ to $0.30eV$. There assumed to be no compensation doping involved.

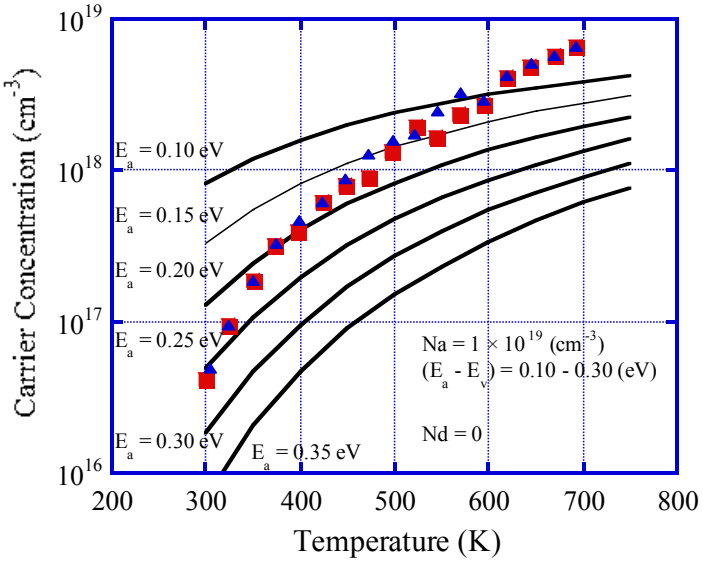

Figure 4.20 Fitting with varied Ea for SND26

Effects of compensating donor concentration was studied and presented in Fig. 4.21 where Nd varies from $10^{15}cm^{-3}$ to $10^{19}cm^{-3}$. Fittings results with Nd values of $10^{15}cm^{-3}$, $10^{16}cm^{-3}$ and $10^{17}cm^{-3}$ did not show a significant difference whereas $Nd = 10^{18}cm^{-3}$ and $Nd = 10^{19}cm^{-3}$ shows significant difference in carrier concentration.

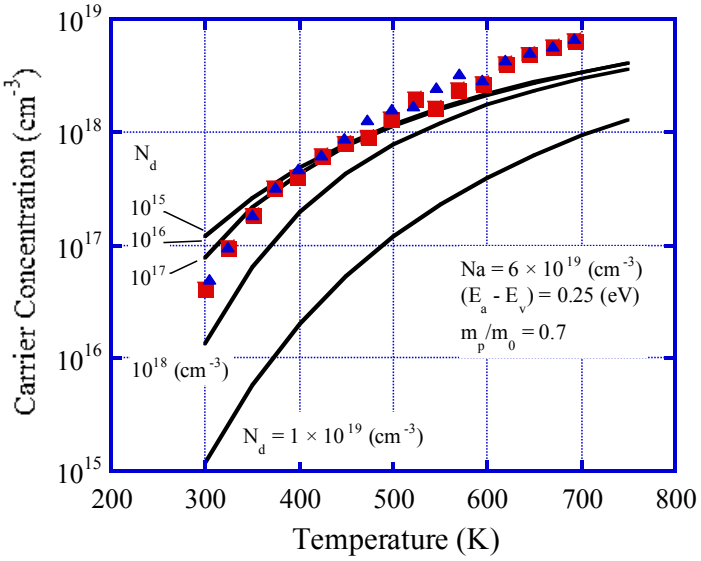

Figure 4.21 Fitting with varied Nd for SND26

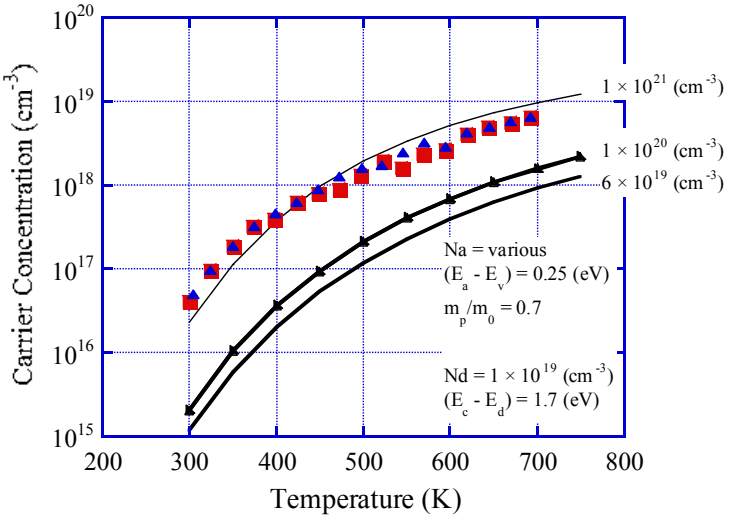

Figure 4.22 Fitting with varied Na for SND26

The effect of the effective mass to carrier concentration is shown in Fig. 4.23 where

mp/mo is ranging between 0.7 to 1. There is a minimal change in the carrier concentration with varied effective mass.

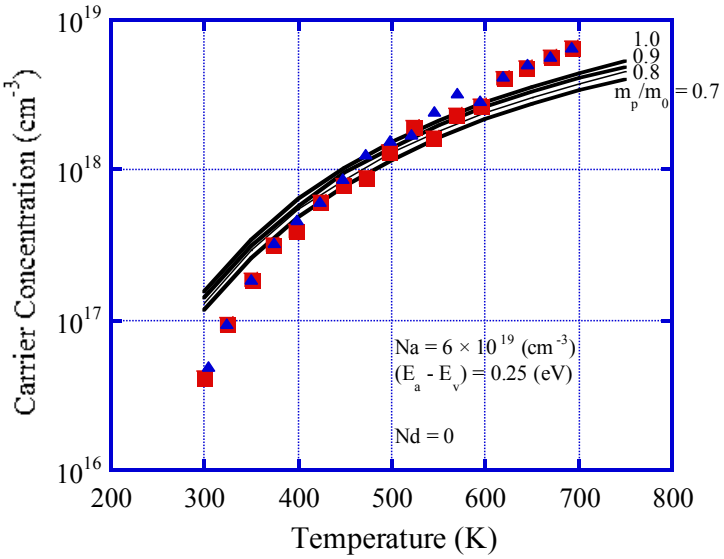

Figure 4.23 Fitting with varied mp/mo for SND26

Mobility analysis were also performed for sample SND26 using the empirical model parameters implemented in Silvaco finite element based software, reported by Marechal et al. [26]. Analysis shown in Fig. 4.24 takes the doping concentration and temperature dependency of the mobility into account.

Our activation energy calculation studies using the same approach shows 2.2 with activation energies of $0.115eV$ for high temperature region and $0.254eV$ for low temperature region for SND25 as shown in Fig. 4.25.

A ratio of 1.150 with activation energies of $0.130eV$ for high temperature region and $0.224eV$ for low temperature region is observed as shown in Fig. 4.26.

A ratio of 1.38 with activation energies of $0.140eV$ for high temperature region and $0.193eV$ for low temperature region is observed as shown in Fig. 4.27.

Temperature dependency of the mobility ranges from around $T^{-1.78}$ to T^2 as seen in

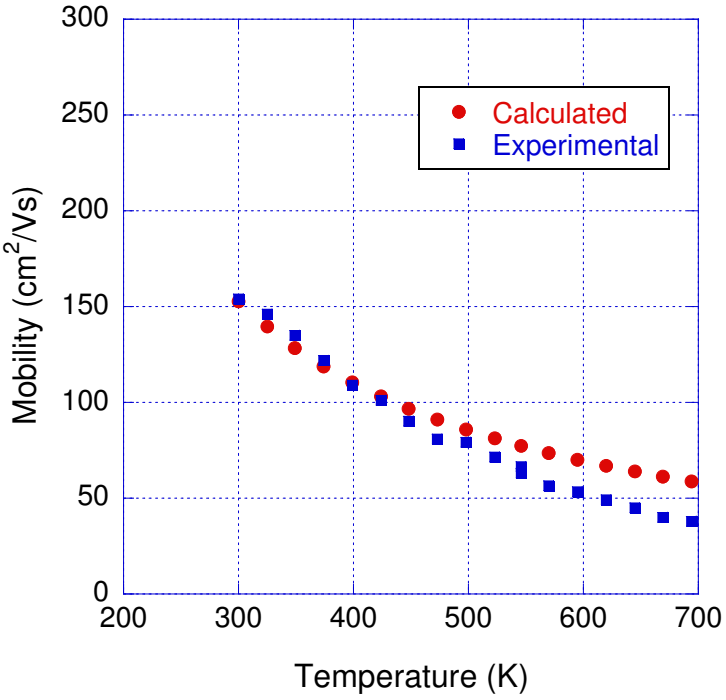

Figure 4.24 Mobility analysis, simulation and experimental values for SND25

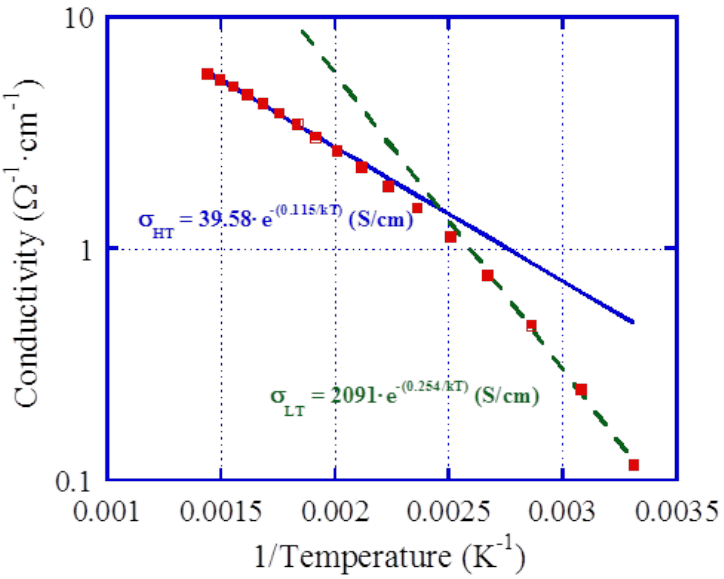

Figure 4.25 Activation energy for SND25

Fig. 4.28. Mobility is impurity dependent and includes a combination of different scattering mechanisms. Volpe et al. reported an extensive study of temperature dependency of the mobility for boron doped single crystal diamond and revealed the temperature dependency

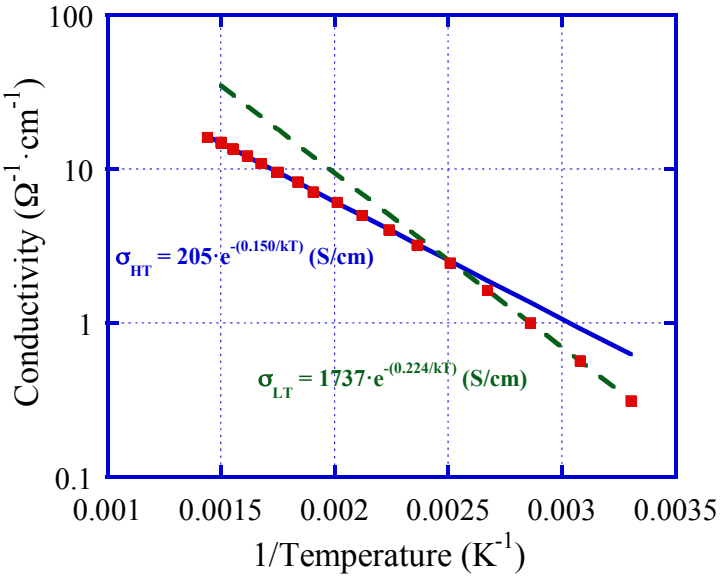

Figure 4.26 Activation energy for SND33

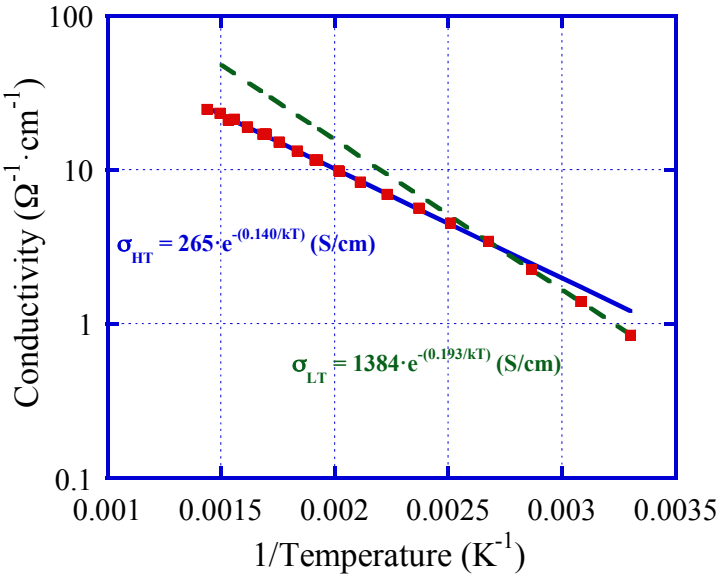

Figure 4.27 Activation energy for SND34

as $T^{-\beta}$ where $\beta_{max} = 3.11$ for pure material and $\beta_{min} = 0$ highly doped material [5].

Concentration measurements for diamond films with varied doping levels can be seen in Fig. 4.29.

Reliable high temperature measurements of resistivity and Hall effect for boron doped single crystal diamond can be achieved in the presence of high quality ohmic contacts. Phys-

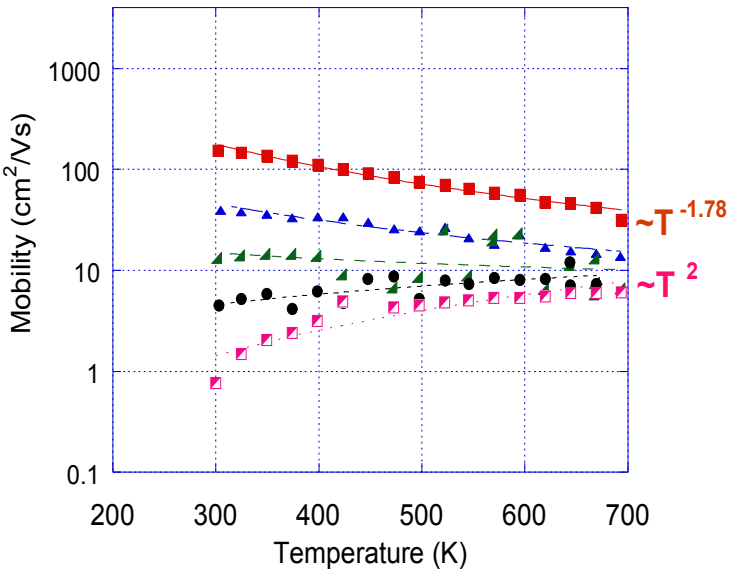

Figure 4.28 Temperature dependent mobility

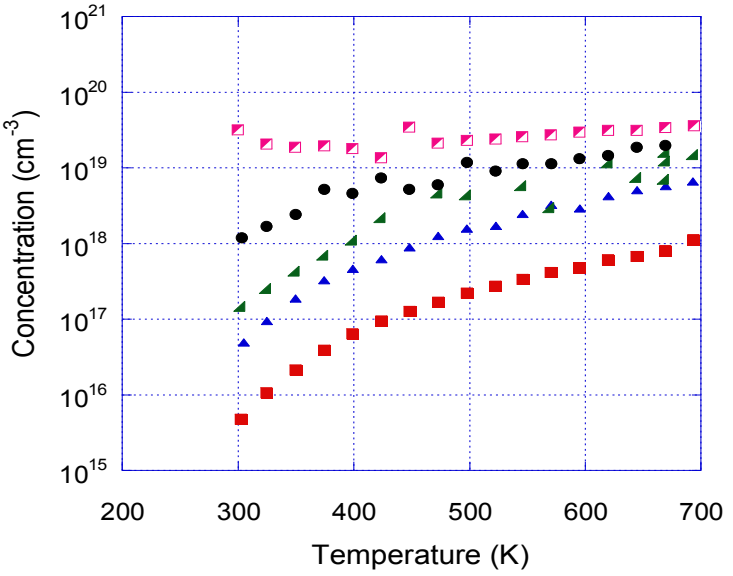

Figure 4.29 Temperature dependent concentration

ical analysis for the identification of unintentional doping can be a very essential tool for providing feedback to MPCVD fabrication of single crystal diamond.

In our studies, we have reported the effect of annealing to the Ohmic characteristics of the contacts. Simulation results have shown the effect of each variable, Na, Nd, Ea, Ed, mp/mo to the carrier concentration. Nitrogen was assumed to be one of the unintentional

impurities and mixed carrier concentration simulation results showed a good agreement with the experimental results.

Carrier concentration of all the samples are consistent with the FTIR and SIMS studies as shown in Demlow et al.s work [14].

4.5 Physical Analysis Results

Least squares method, using *fmincon* algorithm has been implemented for optimization analysis. Details can be found in Sec. 4.6. First analysis carried through with equal weight on each temperature point in the whole temperature range.

Optimization results quantified four parameters for SND25 as $N_A = 9.11 * 10^{18} cm^{-3}$, $E_a = 0.277eV$, $N_D = 1 * 10^{16} cm^{-3}$ and $E_d = 1.489eV$ as seen in Fig. 4.30.

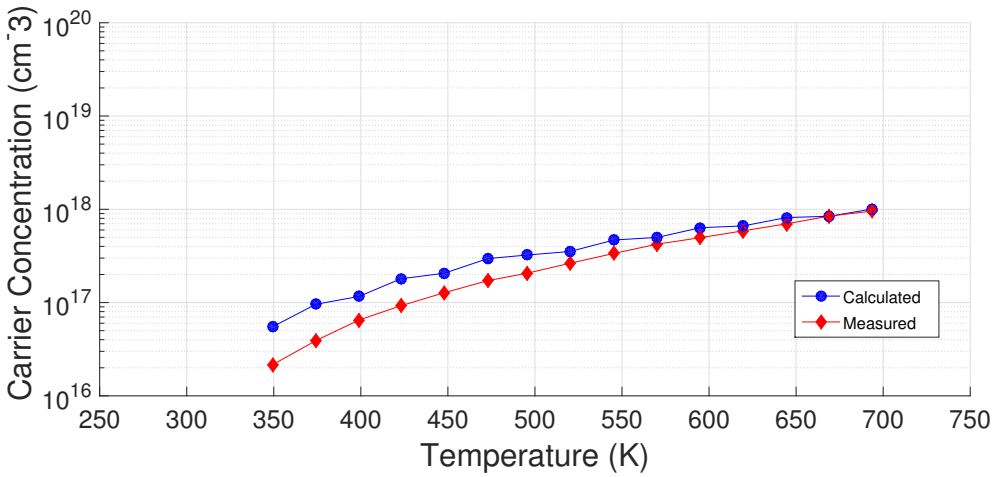

Figure 4.30 Concentration vs temperature fit for SND25

Optimization results quantified four parameters for SND34 as $N_A = 3.64 * 10^{20} cm^{-3}$, $E_a = 0.13eV$, $N_D = 1 * 10^{16} cm^{-3}$ and $E_d = 1.06eV$ as seen in Fig. 4.31.

Deviation of E_d from the ionization energy of nitrogen, $1.7eV$, may be related to the broadening of the energy levels based on the Schrodinger equation and/or possible existence

of unidentified defects contributed as donors.

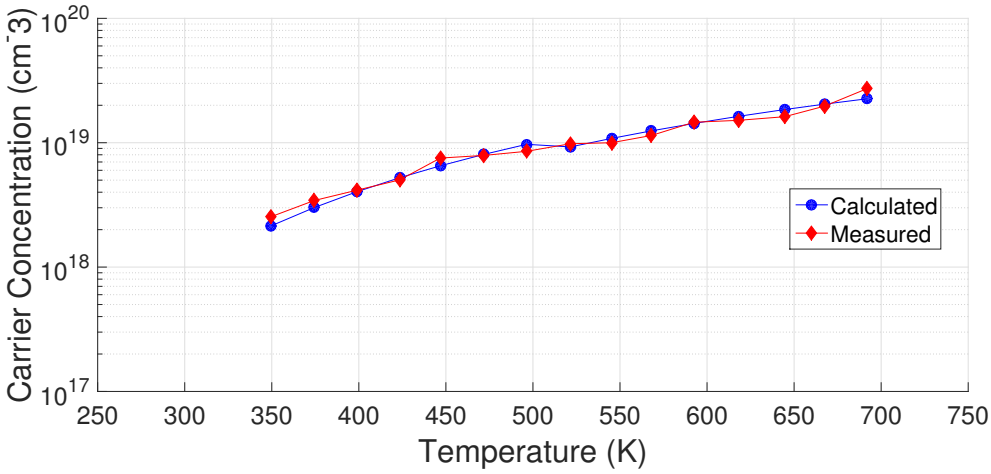

Figure 4.31 Concentration vs temperature fit for SND34

Deposition temperature for SND25 is 850 °C, whereas, for SND34, deposition temperature is 950 °C as reported by Demlow et al.[14]. Depth profile of SIMS measurements showing uniformity of doping profile through the sample depth. SIMS results for samples SND25, SND26, SND33 and SND34 are in good agreement with Hall effect measurments as seen in Fig. 4.32 even after the possible error reported in the SIMS calibration.

The heavily boron doped sample SND34 grown at 950 °C, was measured by SIMS to have 39% more incorporated boron than SND33, which was grown under the same reactor conditions but at 850 °C.

Heavily boron-doped diamond samples grown with a substrate temperature of 950 °C show fewer defects and higher doping efficiency than those grown at 850 °C.

Finally, for the selectively doped diamond sample, LB04, where IV measurements were presented in Fig. 4.10, carrier concentration fit using $N_A = 5 * 10^{17} cm^{-3}$, $E_a = 0.35eV$, $N_D = 2.25 * 10^{15} cm^{-3}$ and $E_d = 1.7eV$ is compared with the measurement result in Fig. 4.33.

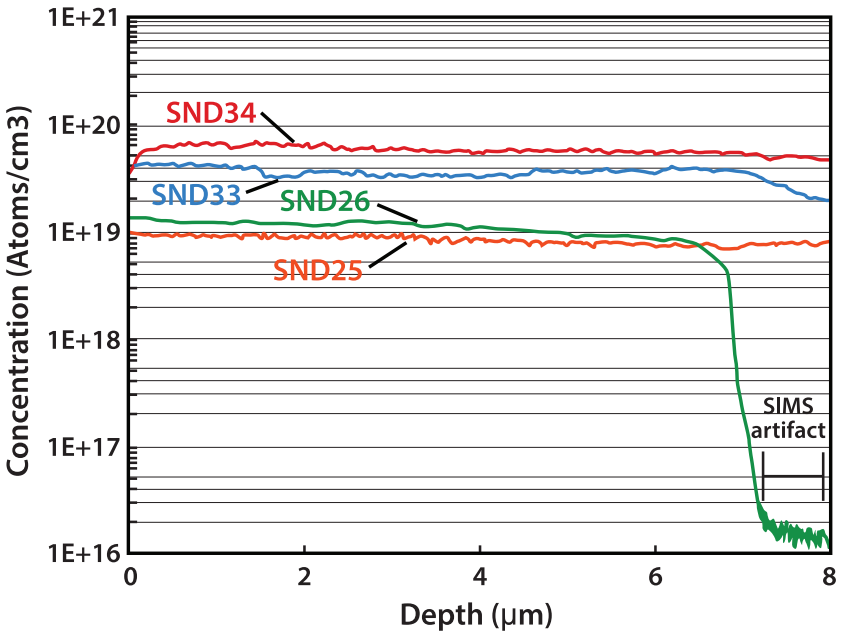

Figure 4.32 SIMS measurements for diamond samples [14]

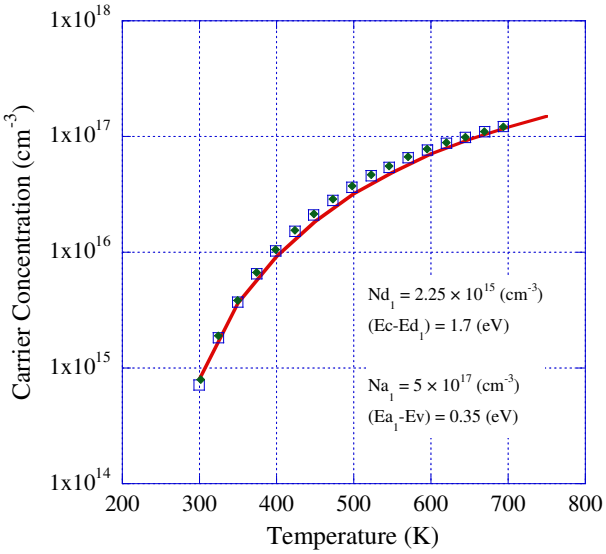

Figure 4.33 Concentration vs temperature fit for LB04

4.6 Software Tools for Analysis

In semiconductor physics, the neutrality equation can be approximated as shown in Eq. 4.10 [11].

$$n + N_A^- = p + N_D^+ \tag{4.10}$$

The total negative charges are shown on the left hand side of the equation with n and N_A, electrons and ionized acceptors, respectively. Positive charges are shown on the right hand side of the equation with p and N_D, holes and ionized donors, respectively.

Electron concentration has been calculated as shown in Eq. 4.11 where N_C is the effective density of states in the conduction band and $F_{1/2}$ is the Fermi-Dirac integral.

$$n = N_C \frac{2}{\sqrt{\pi}} * F_{1/2} * (\frac{E_F - E_C}{kT}) \tag{4.11}$$

In most cases, there is both intentional doping and unintentional doping during the fabrication of single cyrtsal diamond samples. Thus, in this work, we have implemented two acceptor concentrations with two activation energies in order to calculate ionized acceptors as shown in Eq. 4.12a where N_{A1}, N_{A2} and E_{a1}, E_{a2} are the user input values, corresponding to the acceptor concentrations and their activation energies, respectively.

$$N_A^- = N_{A1}^- + N_{A2}^- \tag{4.12a}$$

$$N_{A1}^- = (N_{A1}/(1 + 4 * exp(\frac{E_{a1}}{k_B * T}))) \tag{4.12b}$$

$$N_{A2}^- = (N_{A2}/(1 + 4 * exp(\frac{E_{a2}}{k_B * T}))) \tag{4.12c}$$

Hole concentration has been calculated as shown in Eq. 4.13 where N_V is the effective density of states in the valance band and $F_{1/2}$ is the Fermi-Dirac integral.

$$p = N_V \frac{2}{\sqrt{\pi}} * F_{1/2} * (\frac{E_V - E_F}{kT}) \tag{4.13}$$

Similar to the acceptor concentration approach shown above, we have implemented two donor concentrations with two activation energies in order to calculate ionized donors as shown in Eq. 4.14a where N_{D1}, N_{D2} and E_{d1}, E_{d2} are the user input values, corresponding to the donor concentrations and their activation energies, respectively.

$$N_D^+ = N_{D1}^+ + N_{D2}^+ \tag{4.14a}$$

$$N_{D1}^+ = (N_{D1}/(1 + 2 * exp(\frac{E_{d1}}{k_B * T}))) \tag{4.14b}$$

$$N_{D2}^+ = (N_{D2}/(1 + 2 * exp(\frac{E_{d2}}{k_B * T}))) \tag{4.14c}$$

In order to the satisfy the neutrality equation, Eq. 4.10, using the physical components described above, Fermi-Dirac integral has been calculated with changing variables, $\eta = (E - E_C)/kT$ and $\eta_F = (E_F - E_C)/kT$ as shown in Eq. 4.15a - 4.15c.

$$F_{1/2}(\frac{E_F - E_C}{kT}) \equiv F_{1/2}(\eta_F) \tag{4.15a}$$

$$F_{1/2}(\eta_F) = \int_{E_C}^{\infty} \frac{[(E - E_C)/kT]^{1/2}}{1 + exp[(E - E_F)/kT]} \frac{dE}{kT} \tag{4.15b}$$

$$F_{1/2}(\eta_F) = \int_0^{\infty} \frac{\eta^{1/2}}{1 + exp(\eta - \eta_F)} d\eta \tag{4.15c}$$

Approximation of Boltzmann statistics have not been applied in this work. At the value of the chosen Fermi level, where neutrality equation (Eq. 4.10) is satisfied and emphasized with a yellow circle on the left and shown in more detail on the right in Fig. 4.34.

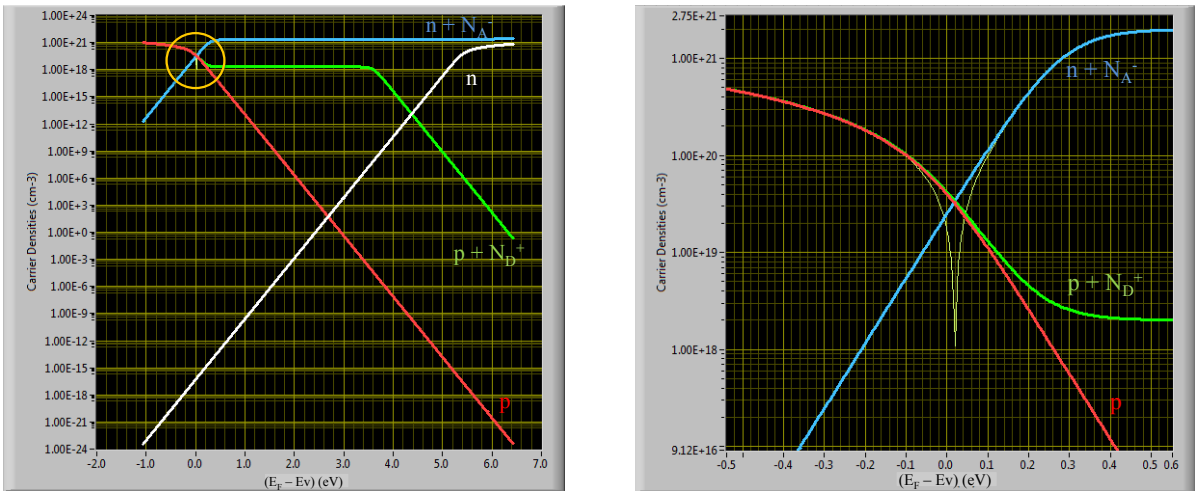

Figure 4.34 Left: All the postivite and negative charges are shown. Right: Zoomed in image where the neutrality equation is satisfied.

Using the LabVIEW based software for physical analysis simulations, expected intentional and unintentional concentrations of the impurities can be calculated. In order to make the analysis computationally inexpensive, MATLAB has been used for physical analysis. A similar approach has been implemented in order to calculate the acceptor and donor concentrations. However, instead of a graphical technique, minimization technique has been used.

To solve the optimization problem, we use the Matlab built-in function fmincon. *fmincon* function aims to find a constrained minimum of a scalar function of numerous variables starting at an initial estimate. Number and duration of iterations depend on the initial guess provided to the program. This is generally referred to as constrained nonlinear optimization or nonlinear programming.

To apply *fmincon*, the gradient of the objective function must be given. In addition, the Hessian matrix of the objective function can greatly speed up the convergence of the optimization problem. But the new problem is that the cost of computing the Hessian matrix is too much. In order to solve this problem, we can use a good approximation to the Hessian

and the cost of calculating the approximation can be accepted relatively.

For any given starting point, we can find a local minimizer through optimization process, but it is hard to determine whether it is a global minimizer or it is sufficiently close to the global minimizer. Therefore, a good choice of the starting point acepptor concentration and activation energy,N_a, E_a and donor concentration and activation energy N_d and E_d, respectively can increase the probability of finding the global minimizer and speed up the convergence rate of the method. In addition, the computational cost of the optimization algorithm can be greatly reduced with a good starting point.

Chapter 5

Conclusions and Future Work

5.1 Conclusion

A temperature dependent Hall Effect measurement system with software based data acquisition and control was built and tested in hardware and software automation level as a part of this PhD work [1].

The system differs from the previously reported systems by adding several control features including a software based PID temperature controller, temperature dependent I-V measurements for monitoring the annealing effects on contact resistances, and the ability to accommodate samples for both van der Pauw and inline configurations.

Transport measurements are primarily shown for boron-doped single crystal diamond (SCD) films deposited in a microwave plasma-assisted chemical vapor deposition (MPCVD) reactor, as well as phosphorus doped single crystal diamond films, poly crystal diamond films, thermoelectric bulk samples and reference samples including germanium and gallium arsenide. The influence of the ohmic contacts and stability of the temperature control to the measurements are studied. For a temperature range of 300K-700K IV curves, Hall mobilities and carrier concentrations are presented. Software analysis and optimization algorithms based on the neutrality equation are developed and results are compared with the measured data.

There are some systematic errors related to temperature gradients present in the speci-

mens subjected to Hall measurements. If a longitudinal temperature gradient $\triangle T_x$ is present in a specimen then a transverse voltage V_N appears in it by virtue of the Ettingshausen-Nerst effect and also a transverse temperature gradient $\triangle T_y$ can generate a thermoelectric error voltage between the Hall electrodes if the specimen and its Hall contacts have a significant thermoelectric power between them and if the thermoelectric power is itself a significant function of the magnetic field [83].

In addition to the Ettingshausen-Nerst effect, there is also Righi-Leduc effect which basically occurs when a magnetic field is applied at proper angles to the direction of a temperature gradient in a conductor, a new temperature gradient is produced perpendicular to both the direction of the original temperature gradient and to the magnetic field [84]. The Ettingshausen-Nerst and Righi-Leduc effects can be eliminated by preventing longitudinal heat flow [85]. Since the Ettingshausen-Nerst effect is a function of electron flow, in a magnetic field, the transverse temperature gradient $\partial T/\partial y$ is always present under usual experimental conditions and the Hall voltage is than adiabatic. To avoid those errors, choosing an appropriate specimen symmetry is helpful but not enough. Permutation of the current polarity and magnetic field orientation are needed to get rid of the errors introduced by such thermomagnetic effects on Hall measurements. Thus, the Hall effect measurement system in this work includes these permutations and eliminates the non-Hall contributions.

5.2 Future Work

Future work includes the following :

- An improved fitting routine will be investigated upon the existing analysis for further investigation of the transport properties of the semiconductor materials. New fitting

routine will be computationally less expensive.

- Thermal-power measurement will be coupled with hall effect to detect effective mass. Followed by the addition of Nernst effect, effective mass can be detected. From thermal-power measurements, fermi level location can be also determined. Diamond materials may require a significant power flow, as a result, effective mass measurements can be more challenging compared to other semiconductor materials.

- Analysis and software implementation of resulting measurements including mixed carrier conduction modeling (QMSA).

BIBLIOGRAPHY

BIBLIOGRAPHY

[1] I. Berkun, S. N. Demlow, N. Suwanmonkha, T. P. Hogan, and T. A. Grotjohn, "Hall Effect Measurement System for Characterization of Doped Single Crystal Diamond," in *MRS Proceedings*, vol. 1511, Cambridge Univ Press, 2013.

[2] P. Gao, I. Berkun, R. D. Schmidt, M. F. Luzenski, X. Lu, P. B. Sarac, E. D. Case, and T. P. Hogan, "Transport and Mechanical Properties of High-ZT Mg2. 08si0. 4- x Sn0. 6sb x Thermoelectric Materials," *Journal of Electronic Materials*, pp. 1–14, 2013.

[3] S. J. Rashid, A. Tajani, D. J. Twitchen, L. Coulbeck, F. Udrea, T. Butler, N. Rupesinghe, M. Brezeanu, J. Isberg, A. Garraway, M. Dixon, R. Balmer, D. Chamund, P. Taylor, and G. Amaratunga, "Numerical Parameterization of Chemical-Vapor-Deposited (CVD) Single-Crystal Diamond for Device Simulation and Analysis," *IEEE Transactions on Electron Devices*, vol. 55, pp. 2744–2756, Oct. 2008.

[4] T. H. Borst and O. Weis, "Boron-Doped Homoepitaxial Diamond Layers: Fabrication, Characterization, and Electronic Applications," *physica status solidi (a)*, vol. 154, pp. 423–444, Mar. 1996.

[5] P.-N. Volpe, J. Pernot, P. Muret, and F. Omns, "High hole mobility in boron doped diamond for power device applications," *Applied Physics Letters*, vol. 94, p. 092102, Mar. 2009.

[6] J. Zhong, "PID Controller Tuning: A Short Tutorial, http://saba.kntu.ac.ir/eecd/pcl/download/PIDtutorial.pdf," 2006.

[7] A. Bennett, "Diamond A Laser Engineer's Best Friend," *Optik & Photonik*, vol. 9, no. 4, pp. 49–52, 2014.

[8] J. P. Lagrange, A. Deneuville, and E. Gheeraert, "Activation energy in low compensated homoepitaxial boron-doped diamond films1," *Diamond and Related Materials*, vol. 7, pp. 1390–1393, Sept. 1998.

[9] T. H. Borst and O. Weis, "Electrical characterization of homoepitaxial diamond films doped with B, P, Li and Na during crystal growth," *Diamond and Related Materials*, vol. 4, pp. 948–953, May 1995.

[10] E. H. Putley, *The Hall Effect and Semi-Conductor Phsyics*. 1960.

[11] S. Sze, *Physics of semiconductor devices*. John Wiley and Sons, NY, 2nd ed., 1981.

[12] L. Diederich, O. M. Kttel, P. Aebi, and L. Schlapbach, "Electron affinity and work function of differently oriented and doped diamond surfaces determined by photoelectron spectroscopy," *Surface Science*, vol. 418, pp. 219–239, Nov. 1998.

[13] K. Takahata, "Micro electronic and mechanical systems," *InTech, December*, vol. 1, 2009.

[14] S. N. Demlow, R. Rechenberg, and T. Grotjohn, "The effect of substrate temperature and growth rate on the doping efficiency of single crystal boron doped diamond," *Diamond and Related Materials*, vol. 49, pp. 19–24, Oct. 2014.

[15] M. Hupert, A. Muck, J. Wang, J. Stotter, Z. Cvackova, S. Haymond, Y. Show, and G. M. Swain, "Conductive diamond thin-films in electrochemistry," *Diamond and Related Materials*, vol. 12, pp. 1940–1949, Oct. 2003.

[16] J. A. Carlisle, "Diamond films: Precious biosensors," *Nature Materials*, vol. 3, pp. 668–669, Oct. 2004.

[17] R. C. Burns, A. I. Chumakov, S. H. Connell, D. Dube, H. P. Godfried, J. O. Hansen, J. Hrtwig, J. Hoszowska, F. Masiello, L. Mkhonza, M. Rebak, A. Rommevaux, R. Setshedi, and P. V. Vaerenbergh, "HPHT growth and x-ray characterization of high-quality type IIa diamond," *Journal of Physics: Condensed Matter*, vol. 21, p. 364224, Sept. 2009.

[18] J. Lu, Y. Gu, T. A. Grotjohn, T. Schuelke, and J. Asmussen, "Experimentally defining the safe and efficient, high pressure microwave plasma assisted CVD operating regime for single crystal diamond synthesis," *Diamond and Related Materials*, vol. 37, pp. 17–28, Aug. 2013.

[19] K. A. Borup, E. S. Toberer, L. D. Zoltan, G. Nakatsukasa, M. Errico, J.-P. Fleurial, B. B. Iversen, and G. J. Snyder, "Measurement of the electrical resistivity and Hall coefficient at high temperatures," *Review of Scientific Instruments*, vol. 83, no. 12, pp. 123902–123902–7, 2012.

[20] C. Wood, A. Lockwood, A. Chmielewski, J. Parker, and A. Zoltan, "High temperature Halleffect apparatus," *Review of Scientific Instruments*, vol. 55, pp. 110–113, Jan. 1984.

[21] T. M. Dauphinee and E. Mooser, "Apparatus for Measuring Resistivity and Hall Coefficient of Semiconductors," *Review of Scientific Instruments*, vol. 26, pp. 660–664, July 1955.

[22] J. M. Lavine, "Alternate Current Apparatus for Measuring the Ordinary Hall Coefficient of Ferromagnetic Metals and Semiconductors," *Review of Scientific Instruments*, vol. 29, pp. 970–976, Nov. 1958.

[23] N. Z. Lupu, N. M. Tallan, and D. S. Tannhauser, "Apparatus for Measuring the Hall Effect of LowMobility Samples at High Temperatures," *Review of Scientific Instruments*, vol. 38, pp. 1658–1661, Nov. 1967.

[24] J. Lyding, H. Marcy, T. Marks, and C. Kannewurf, "Computer automated charge transport measurement system," *IEEE Transactions on Instrumentation and Measurement*, vol. 37, pp. 76–80, Mar. 1988.

[25] G. L. Guthrie, "Sensitive ac Hall Effect Circuit," *Review of Scientific Instruments*, vol. 36, pp. 1177–1179, Aug. 1965.

[26] A. Marchal, N. Rouger, J.-C. Crbier, J. Pernot, S. Koizumi, T. Teraji, and E. Gheeraert, "Model implementation towards the prediction of J (V) characteristics in diamond bipolar device simulations," *Diamond and Related Materials*, vol. 43, pp. 34–42, 2014.

[27] V. S. Bormashov, S. A. Tarelkin, S. G. Buga, M. S. Kuznetsov, S. A. Terentiev, A. N. Semenov, and V. D. Blank, "Electrical properties of the high quality boron-doped synthetic single-crystal diamonds grown by the temperature gradient method," *Diamond and Related Materials*, vol. 35, pp. 19–23, May 2013.

[28] J. Pernot, P. N. Volpe, F. Omns, P. Muret, V. Mortet, K. Haenen, and T. Teraji, "Hall hole mobility in boron-doped homoepitaxial diamond," *Physical Review B*, vol. 81, p. 205203, May 2010.

[29] M. Nesladek, A. Bogdan, W. Deferme, N. Tranchant, and P. Bergonzo, "Charge transport in high mobility single crystal diamond," *Diamond and Related Materials*, vol. 17, pp. 1235–1240, July 2008.

[30] J. Isberg, J. Hammersberg, E. Johansson, T. Wikstrm, D. J. Twitchen, A. J. Whitehead, S. E. Coe, and G. A. Scarsbrook, "High Carrier Mobility in Single-Crystal Plasma-Deposited Diamond," *Science*, vol. 297, pp. 1670–1672, Sept. 2002.

[31] T. Tsubota, T. Fukui, T. Saito, K. Kusakabe, S. Morooka, and H. Maeda, "Surface morphology and electrical properties of boron-doped diamond films synthesized by

microwave-assisted chemical vapor deposition using trimethylboron on diamond (100) substrate," *Diamond and Related Materials*, vol. 9, pp. 1362–1368, July 2000.

[32] J. Barjon, N. Habka, C. Mer, F. Jomard, J. Chevallier, and P. Bergonzo, "Resistivity of boron doped diamond," *physica status solidi (RRL) Rapid Research Letters*, vol. 3, pp. 202–204, Sept. 2009.

[33] K. Das, V. Venkatesan, K. Miyata, D. L. Dreifus, and J. T. Glass, "A review of the electrical characteristics of metal contacts on diamond," *Thin Solid Films*, vol. 212, pp. 19–24, May 1992.

[34] K. L. Moazed, J. R. Zeidler, and M. J. Taylor, "A thermally activated solid state reaction process for fabricating ohmic contacts to semiconducting diamond," *Journal of Applied Physics*, vol. 68, pp. 2246–2254, Sept. 1990.

[35] V. Venkatesan and K. Das, "Ohmic contacts on diamond by B ion implantation and Ti-Au metallization," *IEEE Electron Device Letters*, vol. 13, pp. 126–128, Feb. 1992.

[36] V. Venkatesan, D. M. Malta, K. Das, and A. M. Belu, "Evaluation of ohmic contacts formed by B+ implantation and TiAu metallization on diamond," *Journal of Applied Physics*, vol. 74, pp. 1179–1187, July 1993.

[37] J. A. V. Windheim, V. Venkatesan, D. M. Malta, and K. Das, "Electrical characterization of semiconducting diamond thin films and single crystals," *Journal of Electronic Materials*, vol. 22, pp. 391–398, Apr. 1993.

[38] C. A. Hewett and J. R. Zeidler, "Ohmic contacts to epitaxial and natural diamond," *Diamond and Related Materials*, vol. 2, pp. 1319–1321, Aug. 1993.

[39] M. Geis, "Diamond transistor performance and fabrication," *Proceedings of the IEEE*, vol. 79, pp. 669–676, May 1991.

[40] G. Braunstein and R. Kalish, "Effective ptype doping of diamond by boron ion implantation," *Journal of Applied Physics*, vol. 54, pp. 2106–2108, Apr. 1983.

[41] H. A. Hoff, G. L. Waytena, C. L. Vold, J. S. Suehle, I. P. Isaacson, M. L. Rebbert, D. I. Ma, and K. Harris, "Ohmic contacts to semiconducting diamond using a Ti/Pt/Au trilayer metallization scheme," *Diamond and Related Materials*, vol. 5, pp. 1450–1456, Dec. 1996.

[42] Y. Chen, M. Ogura, S. Yamasaki, and H. Okushi, "Ohmic contacts on p-type homoepitaxial diamond and their thermal stability," *Semiconductor Science and Technology*, vol. 20, p. 860, Aug. 2005.

[43] M. Roser, C. A. Hewett, K. L. Moazed, and J. R. Zeidler, "High Temperature Reliability of Refractory Metal Ohmic Contacts to Diamond," *Journal of The Electrochemical Society*, vol. 139, pp. 2001–2004, July 1992.

[44] C. B. Childs and W.-K. Chu, *Coated substrates and process*. Google Patents, Nov. 1991. US Patent 5,068,020.

[45] D. Twitchen, A. Whitehead, S. Coe, J. Isberg, J. Hammersberg, T. Wikstrom, and E. Johansson, "High-voltage single-crystal diamond diodes," *IEEE Transactions on Electron Devices*, vol. 51, pp. 826–828, May 2004.

[46] F. Fang, C. Hewett, M. Fernandes, and S. Lau, "Ohmic contacts formed by ion mixing in the Si-diamond system," *IEEE Transactions on Electron Devices*, vol. 36, pp. 1783–1786, Sept. 1989.

[47] M. W. Geis, M. Rothschild, R. R. Kunz, R. L. Aggarwal, K. F. Wall, C. D. Parker, K. A. McIntosh, N. N. Efremow, J. J. Zayhowski, D. J. Ehrlich, and J. E. Butler, "Electrical, crystallographic, and optical properties of ArF laser modified diamond surfaces," *Applied Physics Letters*, vol. 55, pp. 2295–2297, Nov. 1989.

[48] G. S. Sandhu, *Ion-beam processing of diamonds*. Ph.D., The University of North Carolina at Chapel Hill, United States – North Carolina, 1989.

[49] J. F. Prins, "Preparation of ohmic contacts to semiconducting diamond," *Journal of Physics D: Applied Physics*, vol. 22, p. 1562, Oct. 1989.

[50] ASTM Standard F76-08, "Test Methods for Measuring Resistivity and Hall Coefficient and Determining Hall Mobility in Single-Crystal Semiconductors," tech. rep., ASTM International, 2008.

[51] W. A. Beck and J. R. Anderson, "Determination of electrical transport properties using a novel magnetic fielddependent Hall technique," *Journal of Applied Physics*, vol. 62, pp. 541–554, July 1987.

[52] T. H. Cunningham, *Quantitative Mobility Spectrum Analysis of III-V Heterostructures On Silicon*. thesis, Nov. 2012.

[53] J. R. Meyer, C. A. Hoffman, F. J. Bartoli, D. A. Arnold, S. Sivananthan, and J. P. Fauri, "Methods for magnetotransport characterization of IR detector materials," *Semiconductor Science and Technology*, vol. 8, p. 805, June 1993.

[54] I. Vurgaftman, J. R. Meyer, C. A. Hoffman, D. Redfern, J. Antoszewski, L. Faraone, and J. R. Lindemuth, "Improved quantitative mobility spectrum analysis for Hall characterization," *Journal of Applied Physics*, vol. 84, pp. 4966–4973, Nov. 1998.

[55] G. Li, N. Hauser, C. Jagadish, J. Antoszewski, and W. Xu, "Study of subband electronic structure of Si doped GaAs using magnetotransport measurements in tilted magnetic fields," *Journal of Applied Physics*, vol. 79, pp. 8482–8487, June 1996.

[56] S. N. Demlow, I. Berkun, M. Becker, T. Hogan, and T. A. Grotjohn, "Dopant Uniformity and Concentration in Boron Doped Single Crystal Diamond Films," in *MRS Proceedings*, vol. 1395, pp. mrsf11–1395, Cambridge Univ Press, 2012.

[57] J. G. Ziegler and N. B. Nichols, "Optimum Settings for Automatic Controllers," *Journal of Dynamic Systems, Measurement, and Control*, vol. 115, pp. 220–222, June 1993.

[58] S. Y. Loo, *Transport characterization of new high temperature quaternary thermoelectric materials and devices*. Ph.D., Michigan State University, United States – Michigan, 2003.

[59] N. Ismail, N. Hashim, and R. Baharom, "A comparative study of Proportional Integral Derivative controller and Fuzzy Logic controller on DC/DC Buck-Boost Converter," in *2011 IEEE Symposium on Industrial Electronics and Applications (ISIEA)*, pp. 149–154, Sept. 2011.

[60] Y. Li, K. H. Ang, and G. Chong, "PID control system analysis and design," *IEEE Control Systems*, vol. 26, pp. 32–41, Feb. 2006.

[61] "Integrator Manual, http://www.vdwalle.com/Norte/EMC2_integrator_manual.pdf," Jan. 2012.

[62] "Ioffe Institute, http://www.ioffe.ru/SVA/NSM/Semicond/GaAs/electric.html#Hall," 2001.

[63] A. Christou and W. M. Webb, *GaAs MMIC Reliability-High Temperature Behavior*. RIAC, 2006.

[64] K.-P. Kuo and J. Asmussen, "An experimental study of high pressure synthesis of diamond films using a microwave cavity plasma reactor," *Diamond and Related Materials*, vol. 6, pp. 1097–1105, July 1997.

[65] G. A. Slack and M. A. Hussain, "The maximum possible conversion efficiency of silicon-germanium thermoelectric generators," *Journal of Applied Physics*, vol. 70, pp. 2694–2718, Sept. 1991.

[66] T. Dasgupta, C. Stiewe, R. Hassdorf, A. J. Zhou, L. Boettcher, and E. Mueller, "Effect of vacancies on the thermoelectric properties of Mg2si1-xSbx (0 x 0.1)," *Physical Review B*, vol. 83, p. 235207, June 2011.

[67] A. H Wilson, "A Note on the Theory of Rectification," *Proceedings of the Royal Society of London. Series A, Containing Papers of a Mathematical and Physical Character*, vol. 136, no. 830, pp. 487 – 498, 1932.

[68] A. H. Wilson, "The theory of electronic semi-conductors," *Proceedings of the Royal Society of London. Series A, Containing Papers of a Mathematical and Physical Character*, pp. 458–491, 1931.

[69] W. Schottky, "Halbleitertheorie der Sperrschicht," *Naturwissenschaften*, vol. 26, pp. 843–843, Dec. 1938.

[70] N. F. Mott, "Note on the contact between a metal and an insulator or semi-conductor," *Mathematical Proceedings of the Cambridge Philosophical Society*, vol. 34, pp. 568–572, Oct. 1938.

[71] H. A. Bethe, *Theory of the boundary layer of crystal rectifiers*. Radiation Laboratory, Massachusetts Institute of Technology, 1942.

[72] E. H. Rhoderick, "Metal-semiconductor contacts," *IEE Proceedings I (Solid-State and Electron Devices)*, vol. 129, no. 1, pp. 1–14, 1982.

[73] E. H. Rhoderick, "Transport processes in Schottky diodes," *Metal-Semiconductor Contacts. Institute of Physics, London. 1974, 3-19*, 1974.

[74] V. L. Rideout, "A review of the theory, technology and applications of metal-semiconductor rectifiers," *Thin Solid Films*, vol. 48, no. 3, pp. 261–291, 1978.

[75] R. T. Tung, "Recent advances in Schottky barrier concepts," *Materials Science and Engineering: R: Reports*, vol. 35, pp. 1–138, Nov. 2001.

[76] L. Kolaklieva and R. Kakanakov, "Ohmic Contacts for High Power and High Temperature Microelectronics," in *Micro Electronic and Mechanical Systems* (K. Takahata, ed.), InTech, Dec. 2009.

[77] A. Y. C. Yu, "Electron tunneling and contact resistance of metal-silicon contact barriers," *Solid-State Electronics*, vol. 13, no. 2, pp. 239–247, 1970.

[78] L. Kolaklieva and R. Kakanakov, *Ohmic Contacts for High Power and High Temperature Microelectronics*. INTECH Open Access Publisher, 2009.

[79] H. H. Berger, "Models for contacts to planar devices," *Solid-State Electronics*, vol. 15, no. 2, pp. 145–158, 1972.

[80] G. S. Marlow and M. B. Das, "The effects of contact size and non-zero metal resistance on the determination of specific contact resistance," *Solid-State Electronics*, vol. 25, pp. 91–94, Feb. 1982.

[81] Y. G. Chen, M. Ogura, S. Yamasaki, and H. Okushi, "Investigation of specific contact resistance of ohmic contacts to B-doped homoepitaxial diamond using transmission line model," *Diamond and Related Materials*, vol. 13, pp. 2121–2124, Nov. 2004.

[82] J. Barjon, E. Chikoidze, F. Jomard, Y. Dumont, M.-A. Pinault-Thaury, R. Issaoui, O. Brinza, J. Achard, and F. Silva, "Homoepitaxial boron-doped diamond with very low compensation," *physica status solidi (a)*, vol. 209, pp. 1750–1753, Sept. 2012.

[83] B. V. Paranjape and J. S. Levinger, "Theory of the Ettingshausen Effect in Semiconductors," *Physical Review*, vol. 120, pp. 437–441, Oct. 1960.

[84] G. Sonnino and P. Peeters, "Nonlinear Hall effect for materials with weak thermoelectric power coefficients: Preliminary comparisons between theoretical results of the thermodynamic field theory and experimental data," *Chaos: An Interdisciplinary Journal of Nonlinear Science*, vol. 14, pp. 910–923, Sept. 2004.

[85] C. M. Hurd, "The accurate determination of the Hall coefficient of a metal," *Journal of Scientific Instruments*, vol. 42, p. 465, July 1965.